



Universität Hamburg
DER FORSCHUNG | DER LEHRE | DER BILDUNG

Time-resolved Auger spectroscopy on thin films with excitation by short electron pulses

Dissertation
zur Erlangung des Doktorgrades

an der
Fakultät für Mathematik, Informatik und Naturwissenschaften
Fachbereich für Physik
der Universität Hamburg

vorgelegt von
Hannes Lasse Edvard Bein
geboren am 09.11.1989 in Henstedt-Ulzburg

Hamburg
2021

Gutachter: *Prof. Dr. Markus Drescher*
Prof. Dr. Henning Moritz

Zusammensetzung der Prüfungskommission: *Prof. Dr. Markus Drescher*
Prof. Dr. Henning Moritz
Prof. Dr. Daniela Pfannkuche
Prof. Dr. Tais Gorkhover
Prof. Dr. Ludwig Mathey

Vorsitzende der Prüfungskommission: *Prof. Dr. Daniela Pfannkuche*

Datum der Disputation: *21. September 2021*

Vorsitzender des Fach-Promotionsausschusses: *Prof. Dr. Wolfgang Hansen*

Leiter des Fachbereiches Physik: *Prof. Dr. Günter Hans Walter Sigl*

Dekan der Fakultät für Mathematik,
Informatik und Naturwissenschaften: *Prof. Dr. Heinrich Graener*

Abstract

In recent years, a broad spectrum of time-resolving techniques for surface analysis has emerged. Often utilising a combination of optical and electron pulses, methods like time-resolved electron energy-loss spectroscopy can investigate samples in a broad energy range, while providing temporal resolution in the femtosecond regime.

In this thesis, a new technique will be introduced, which will determine the Auger lifetime in solid samples on thin films via THz streaking. Previously, this technique was limited to gaseous samples. The experimental setup will utilise a photon-driven electron gun to generate 138_{-38}^{+12} fs electron pulses. The Auger electrons will be generated by the electron pulses on the backside of the anode, which serves as a sample holder. The energy modulation of the electron signal induced by the THz pulses, which are reflected at the sample surface, allows to determine a phase shift between primary and Auger electrons and thus the decay time of the Auger process.

With the newly developed methodology it was possible to determine the Auger lifetime of solid carbon to $\tau_{\text{Auger}} = 13_{-13}^{+100}$ fs.

Kurzfassung

In den letzten Jahren hat sich ein breites Spektrum an zeitauflösenden Techniken für die Oberflächenanalyse entwickelt. Oftmals durch die Kombination von optischen und Elektronenpulsen, können Methoden wie die zeitaufgelöste Elektronen-Energieverlust-Spektroskopie Proben in einem weiten Energiebereich untersuchen und gleichzeitig eine zeitliche Auflösung im fs-Bereich liefern.

In dieser Arbeit wird eine neue Technik vorgestellt, die es erlaubt, die Auger-Lebensdauer von festen Proben auf dünnen Schichten mittels THz-Streaking zu bestimmen. Bisher war diese Technik auf gasförmige Proben beschränkt. Der experimentelle Aufbau verwendet eine photonengetriebene Elektronenkanone zur Erzeugung von 138_{-38}^{+12} fs-Elektronenpulsen. Die Auger-Elektronen werden durch die Elektronen-Pulse auf der Rückseite der Anode erzeugt, die als Probenhalter fungiert. Die durch die an der Probenoberfläche reflektierten THz-Pulse induzierte Impulsmodulation des Elektronensignals, erlaubt es eine Phasenverschiebung zwischen Primär- und Auger-Elektronen und damit die Abklingzeit des Auger-Prozesses zu bestimmen.

Mit der neu entwickelten Technik war es möglich, die Auger-Lebensdauer von festem Kohlenstoff zu $\tau_{\text{Auger}} = 13_{-13}^{+100}$ fs zu bestimmen.

Contents

Introduction	17
1 The Interaction of Ultrashort Laser Pulses and Electron pulses with Matter	19
1.1 Ultrashort Light Pulses	20
1.2 Non-Linear Interaction of Light with Matter	22
1.2.1 Frequency Conversion in Non-Linear Crystals	23
1.2.2 Second and Third Harmonic Generation	25
1.3 Terahertz Radiation	27
1.3.1 Fundamental Principles of Photon-Driven THz Sources	27
1.3.2 Optical Rectification	28
1.3.3 Tilted-Pulse-Front Pumping	29
1.3.4 Material Selection	30
1.3.5 THz Generation in Lithium Niobate	31
1.3.6 Detection of Terahertz Radiation	33
1.4 Electron Interactions	35
1.4.1 Photoelectric Effect	35
1.4.2 Non-Linear Photoionisation	36
1.4.3 Bethe Formula	37
1.4.4 Berger-Seltzer Formula	38
1.5 Auger electrons	40
1.6 Light Field Driven Streaking	41
1.6.1 Classical Approach	41
1.6.2 Quantum Mechanical Approach	43
1.6.3 Reconstruction of Pulse Characteristics	44
2 Experimental Setup and its Characterisation	47
2.1 Femtosecond Laser System	47
2.2 Second and Third Harmonic Generation	49
2.3 THz Radiation Source	52

2.3.1	Electro-Optical Sampling	53
2.4	Experimental Chamber	55
2.4.1	Electron Gun	58
2.4.2	Time-Of-Flight Spectrometer	61
2.5	Multiple-Event Time Digitiser	65
2.5.1	Schematic Data Acquisition	65
2.5.2	MCS6A Time Digitiser	67
3	Streaking Carbon Auger Electrons	69
3.1	Auger Spectrum of Carbon	69
3.2	Streaking of Auger Electrons	72
3.2.1	Reconstructing the Electron Pulse	73
3.2.2	Reconstructing the THz pulse	75
3.2.3	Lifetime of the Auger Decay	76
4	Summary and Outlook	83
4.1	Summarised Results	83
4.2	Outlook	84
4.2.1	Optimising the Setup	84
4.2.2	Possible Targets	87
	Bibliography	91

List of Figures

1.1	Particle Interpretation of SHG, SFG and DFG	24
1.2	Index-Ellipsoid	26
1.3	Optical Rectification	29
1.4	Tilted-Pulse-Front Pumping	30
1.5	Phase Matching in the TFPF Configuration	31
1.6	EOS Methodology	34
1.7	Inelastic Mean Free Path	39
2.1	Laser-System	48
2.2	THG Setup	49
2.3	THG Spectra	51
2.4	THz Setup	52
2.5	Setup for EOS Sampling	54
2.6	EOS Sampling and THz Spectrum	55
2.7	Experimental Chamber	56
2.8	Interaction Zone	57
2.9	Auger process	58
2.10	TEM-window	58
2.11	Electron Gun Characteristic Function	59
2.12	Electron Gun Pulse Broadening	60
2.13	Pulse Broadening in the Anode	61
2.14	Time-Of-Flight Spectrometer	62
2.15	Spectrometer Calibration	63
2.16	Example Spectrum	64
2.17	Constant Fraction Discriminator	65
2.18	Schematic Data Acquisition	66
3.1	Auger Spectrum in TOF Frame	70
3.2	Auger Spectrum (Literature)	71
3.3	Pulse Reconstruction	72
3.4	Streaked Auger Electrons	73
3.5	Streaked and Unstreaked Spectra	74
3.6	Spectral Width VS Delay	75

3.7	Vector Potential and Electric Field of the THz pulses . .	76
3.8	Auger Lifetime VS Temporal Shift	77
3.9	Streaked Primary Electrons	78
3.10	Auger and Primary Phase Shift	79
3.11	Doppler Effect for Arbitrary Angles	79
3.12	Redshift of THz Spectra	80
3.13	redshift Corrected Streaking Traces	81
4.1	THz Wave-Guide and RFA	85
4.2	Electron Gun with THz Pulse Compression	86
4.3	Pierce-Type Gun	86
4.4	Auger Cross Section for Different Elements	87

List of Tables

1.1	Parameters of Materials for Optical Rectification	28
3.1	Auger Decays in Carbon	70

DECLARATION

I hereby do solemnly declare that this thesis is the product of my own independent work. All content and ideas drawn directly or indirectly from external sources are indicated as such. The thesis has not been submitted to any other examining body and has not been published.

A handwritten signature in blue ink, appearing to read "James B. ...". The signature is written in a cursive style with a long horizontal flourish extending to the right.

Introduction

To understand the nature of chemical, electronic or structural transitions in their intrinsic timescales, experiments have to be designed that can resolve those parameters on the natural scales of those processes. For this purpose a plethora of different techniques has been developed in the recent decades, synchronised to the aggregate state of the probe, the timescale of the investigated phenomenon or its energy scale. Common to almost all experimental approaches that strive to resolve the natural timescale of a process is the pump-probe methodology. Here an electron or optical pump pulse initiates a sample response, which is monitored by an electron or optical probe. By introducing a defined and variable delay between pump and probe, the response of the sample to the pump can be scanned. A common hurdle in a variety of approaches has been, and still is, to combine a high signal strength with a short pump or probe duration while maintaining a tabletop form factor. Optical tabletop sources can nowadays provide almost single-cycle pulses, where durations down to 43 as can be reached [1]. Regarding the photon energy, one of the most advanced techniques is the generation of high harmonics in aperiodic modulated fibres where energies in the 300 eV range are possible [2].

For some applications, a much higher energy and flux are needed than HHG sources could provide. Therefore, some experiments use electrons as pump or probe pulses. In modern setups the energy ranges of atomic or molecular phenomena are easily exceeded. Nevertheless, a trade-off between bunch charge and pulse duration has to be made if electron pulses are used.

To reach pulse durations below 1 ps is still challenging and can only be achieved as long as significant sacrifices are made in terms of bunch charge. In modern setups it is possible to reach pulse durations of electron beams down to 28 fs through the use of THz bunch compression [3].

Many experimental setups pursue the goal of investigating the chemical composition of a sample or even attempt to track the influences of a chemical reaction on its natural timescale.

For this endeavour it is necessary to find markers that stay unaltered during a chemical reaction and experience a low influence by the chosen experimental technique. A possible choice for a marker is the Auger process. In this process a core-shell electron is ejected by an X-ray photon or a highly energetic particle. If now a weakly bound outer-shell electron fills the newly formed hole, the energy released in this relaxation process can eject another electron, which is denoted as an Auger electron. As long as the threshold for an Auger decay is reached, the energy of the final Auger electron is independent of the exciting energy, making Auger spectroscopy a powerful tool to identify chemical constituents in a sample.

A common technique to investigate the timescales on which an Auger decay takes place is THz streaking. Here a gaseous sample is excited by an ultra-fast XUV pulse and the momentum of the generated photo- and Auger electrons is altered by a delayed THz pulse. If now the phase shift between the energy modulation of photoelectrons, which will be generated prior to the Auger electrons, and the modulation of the Auger electrons is measured, statements on the lifetime of the Auger decay can be made.

With the experimental setup introduced in this thesis, the range of possible samples will be expanded to solid-state matter and should in theory grant access to Auger decays with the highest energy thresholds.

The approach that will be presented in the following, will use short electron pulses to initiate the Auger decay and strong near single-cycle THz pulses to measure the phase shift between the energy modulation of the exciting electrons and the Auger electrons in order to explore its capability to determine the lifetime of the Auger decay in a carbon sample. To minimise the duration of the electron pulses while maximising the bunch charge, the setup will utilise a photon-driven electron gun with an integration of the sample holder as gun anode. To understand the principles that form the basis of the setup at hand, Chapter 1 will give a short introduction to the theoretical background of the interaction of ultra-short laser and electron pulses with matter as well as the generation and detection of the THz pulses needed for the energy modulation. In the subsequent Chapter 2, the experimental setup with the photon-driven electron gun and the source of the strong near single-cycle THz pulses will be described and characterised in detail. Chapter 3 will present the experimental results obtained with the showcased setup. Concluding with Chapter 4, this thesis will give a summary of the collected insights as well as an elaborated schedule for future optimisations of the setup.

Chapter 1

The Interaction of Ultrashort Laser Pulses and Electron pulses with Matter

To gain a general theoretical understanding of the physical mechanisms underlying this work, the following Chapter will give insights into the description of ultrashort laser pulses that will be used to operate a photon-driven electron gun, which again will be utilised to gain access to the KLL¹ Auger electrons of carbon. Here the knowledge of the interaction of electrons and matter comes into play, since the electron pulses generated by the electron gun will make these Auger electrons accessible. In addition, information is given on the generation of strong few-cycle THz pulses in electro-optic crystals. These THz pulses will be used to streak the Auger electrons to extract the underlying temporal dynamic of their decay process.

In general, ultrashort laser pulses with pulse durations of femto- or attoseconds are utilised to investigate molecular or atomic reaction dynamics in the time-domain. Wavelengths in the vacuum ultraviolet or soft X-ray regime are needed to access molecular or atomic transitions. Since no true gain medium for lasing in the ultraviolet regime exists, these wavelengths have to be obtained via SHG, THG or HHG² (see Section 1.2.2). For most elements even higher photon energies are needed, if Auger electrons are of interest. Here energies in the range of $\mathcal{O}(100)$ eV up to $\mathcal{O}(1000)$ eV are required. These realms can only be conquered with advanced HHG setups [2], FELs³ [4] or electron pulses.

In this work, ultrashort laser pulses in the ultraviolet spectral range will be used to generate electron pulses via the photoelectric effect in a thin silver layer. These electron pulses will create Auger electrons in carbon, which will be streaked with intense few-cycle THz pulses.

¹ **Auger notation:**

e^- creates core-hole in K-shell

e^- from L-shell fills hole

transition-energy ejects e^- in L-shell

² **SHG:**

Second Harmonic Generation **THG:**

Third Harmonic Generation **HHG:**

High Harmonic Generation

³ **FEL: Free Electron Laser**

Therefore, this Chapter will start with a compendious introduction on ultrashort light pulses, will then cover briefly the theory of second and third harmonic generation, followed by a short section on the generation and detection of strong few-cycle THz pulses and will end with the interaction of electrons and matter.

1.1 Ultrashort Light Pulses

⁴ For the sake of clarity, spatial components are omitted for the time being

⁵ $\mathcal{E}(t)$ is a real quantity, while $E(\omega)$ is complex

In theory, any form of light pulse is temporally characterised⁴ by its time-dependent electric field $\mathcal{E}(t)$.⁵ However, the temporal evolution of an ultrashort pulse in the time-domain is difficult to reconstruct with experimental techniques. Therefore, often the representation in the frequency-domain is preferred, which is the Fourier transform of the temporal representation given by

$$E(\omega) = E_0(\omega)e^{i\phi(\omega)}, \quad (1.1)$$

where $E_0(\omega)$ represents the real-valued amplitude, $\phi(\omega)$ the spectral phase and ω the angular frequency. With an inverse Fourier transform the complex time-dependent representation of the electric field can be obtained by

$$\begin{aligned} E(t) &= \frac{1}{2\pi} \int_{-\infty}^{\infty} E(\omega)e^{-i\omega t} dt \\ &= E_0(t)e^{i(\psi(t) - \omega_0(t))}. \end{aligned} \quad (1.2)$$

Here the real value $E_0(t)$ represents the amplitude, $\psi(t)$ the temporal phase and $\omega_0(t)$ the carrier frequency. If both the amplitude and the phase are known, the pulse is completely described. Through the Fourier transform, the pulse is automatically completely described in both representations.

It is common to use a Taylor expansion of the phase around the central angular frequency ω_0 or the reference time t_0 since it is often hard to find an analytical form for the pulse found in an experiment. In the frequency domain the Taylor expansion is given as the following

$$\begin{aligned} \phi(\omega) &= \sum_{n=0}^{\infty} \frac{1}{n!} \frac{\partial^n \phi(\omega_0)}{\partial \omega^n} (\omega - \omega_0)^n \\ &= \phi_0 + \phi_1(\omega - \omega_0) + \frac{1}{2}\phi_2(\omega - \omega_0)^2 \\ &\quad + \frac{1}{6}\phi_3(\omega - \omega_0)^3 + \dots + \frac{1}{n!}\phi_n(\omega - \omega_0)^n, \end{aligned} \quad (1.3)$$

with $\phi_n = \partial^n \phi(\omega_0) / \partial \omega^n$. In addition, ϕ_0 denotes the carrier envelope phase, which is the phase between the envelope of the electric field of the pulse and its carrier frequency. This quantity is of special interest when describing the interactions of ultrashort pulses, since the electric

field and the resulting intensity may be strongly dependent on the carrier envelope phase. The group delay is given by ϕ_1 , which describes the arrival time of the pulse relative to the reference time t_0 . The linear chirp ϕ_2 or GDD⁶ of the pulse describes the arrival time of each spectral component of the pulse. Depending on how the pulse is chirped, the arrival time of a given spectral component can either increase or decrease with the frequency. The last element of the Taylor expansion we work on is ϕ_3 and is called third-order dispersion and leads to the formation of a series of pre or postpulses in the time domain. The same representation can be done for the phase in the time-domain

$$\begin{aligned}\psi(t) &= \sum_{n=0}^{\infty} \frac{1}{n!} \frac{\partial^n \psi(t_0)}{\partial t^n} (t - t_0)^n \\ &= \psi_0 + \psi_1(t - t_0) + \frac{1}{2} \psi_2(t - t_0)^2 \\ &\quad + \frac{1}{6} \psi_3(t - t_0)^3 + \dots + \frac{1}{n!} \psi_n(t - t_0)^n\end{aligned}\tag{1.4}$$

In correspondence to the elements ϕ_n , the elements ψ_n reflect the same relation but only in the time-domain.

A special case occurs when all non-linear terms of the Taylor expansion in the frequency-domain of the phase vanish. In this case, the phase is considered flat and the pulse is Fourier-limited. Therefore, the pulse is as short as possible for a given amplitude $A(\omega)$. Linked through the Fourier transformation, one can obtain the following relationship between pulse duration and spectral bandwidth $\Delta\omega$

$$\frac{\Delta\omega}{2\pi} \tau = \Delta\nu\tau \geq TBP,\tag{1.5}$$

where TBP is the time-bandwidth product of the pulse and is dependent on the pulse shape. In most cases, it is sufficient to assume a Gaussian temporal pulse shape. Here the temporal amplitude can be written as

$$E(t) = E_0 \exp\left(-\frac{(t - t_0)^2}{2\sigma^2}\right),\tag{1.6}$$

where E_0 is denoting the maximal electric field amplitude, t_0 the reference time and σ the RMS⁷ pulse duration, which again is related to the FWHM⁸ pulse duration τ via

$$\tau = 2\sqrt{2 \ln 2} \sigma.\tag{1.7}$$

Therefore, the TBP of a pulse with Gaussian temporal profile is $TBP = \frac{2 \ln 2}{\pi}$. The TBP of other pulse shapes can be found for example in [5].

Leaving the temporal description of pulses, we will now focus on the spatial propagation of light. In many instances, a paraxial approximation⁹ is sufficient to characterise a beam [5].

⁶ **GDD: Group Delay Dispersion**

⁷ **RMS: Root Mean Square**

⁸ **FWHM: Full Width Half Maximum**

⁹ **Paraxial Approximation:** changes in the transverse beam dimension are small compared to the propagated distance.

Solving the paraxial Helmholtz equation and using polar coordinates, the intensity of a beam propagating in z -direction can be given by

$$I(r, z) = I_0 \left(\frac{w_0}{w(z)} \right)^2 \exp \left(-\frac{2r^2}{w(z)^2} \right), \quad (1.8)$$

where I_0 denotes the maximal intensity, w_0 the beam waist in the focal plane at which the intensity has dropped to I_0/e^2 and $w(z)$ the waist with respect to the propagation direction. It may be convenient to rewrite those parameters using the Rayleigh range z_R , the central wavelength of the pulse λ_0 and the peak power P_0 to

$$I_0 = \frac{2P_0}{\pi w_0^2}, \quad w(z) = \pi \frac{w_0^2}{\lambda_0} \quad \text{and} \quad z(r) = w_0 \sqrt{1 + \frac{z^2}{z_R^2}}. \quad (1.9)$$

The Rayleigh range defines the distance z at which the area of the beam waist w_0 has doubled, hence $w(\pm z_R) = \sqrt{2} w_0$. The confocal parameter is given by $2z_R$ and defines the depth of focus. The combination of Equations (1.6) and (1.8) leads to the temporal evolution of the intensity of a Gaussian pulse

$$I(r, z, t) = I_0 \left(\frac{w_0}{w(z)} \right)^2 \exp \left(-\frac{2r^2}{w(z)^2} \right) \exp \left(-\frac{(t - t_0)^2}{2\sigma^2} \right). \quad (1.10)$$

Further information can be found in the pertinent literature, for example [5, 6, 7, 8]

1.2 Non-Linear Interaction of Light with Matter

Generalising Equation (1.2) and taking spatial dependencies into account, one can describe the propagation of an electromagnetic pulse in a homogeneous, non-magnetic medium, without free charge carriers and currents as

$$\left(\nabla^2 - \frac{1}{c^2} \frac{\partial^2}{\partial t^2} \right) \vec{E}(\vec{r}, t) = \mu \frac{\partial^2}{\partial t^2} \vec{P}(\vec{r}, t), \quad (1.11)$$

with $c = 1/\sqrt{\epsilon\mu}$ as the speed of light, μ the permeability and ϵ the permittivity. The quantity \vec{P} is the induced macroscopic polarisation of the medium and describes the linear interaction of charge carriers in the medium with the electric field of the pulse

$$\vec{P}(\vec{r}, t) = \epsilon \int_{-\infty}^{\infty} \chi(t - t') \vec{E}(t') dt' \quad (1.12)$$

where χ gives the electronic susceptibility of the medium. It can be convenient to transform this equation to $\vec{P}(\omega) = \epsilon \chi(\omega) \vec{E}(\omega)$ and perform a Taylor expansion of χ around $\vec{E} = 0$ [9, 10]

$$\begin{aligned} \vec{P} &= \epsilon_0 \left(\chi^{(1)} + \chi^{(2)} \vec{E} + \chi^{(3)} \vec{E}^2 + \dots \right) \vec{E} \\ &= \vec{P}^{(1)} + \vec{P}^{(2)} + \vec{P}^{(3)} + \dots \end{aligned} \quad (1.13)$$

The susceptibilities $\chi^{(i)}$ represent tensors of the order $(i + 1)$ and link an i -fold product of vector components of \vec{E}_j to a given component of the i^{th} Polarisation $\vec{P}^{(i)}$. It is customary to describe the linear component of the polarisation separately

$$\vec{P} = \epsilon_0 \chi^{(1)} \vec{E}. \quad (1.14)$$

From this term refraction, diffraction, absorption and dispersion [5] can be derived. In addition, a linear response results in properties of the medium that are independent of the intensity of the incoming pulse. A direct result of this relationship is the linear index of refraction

$$n_0(\omega) = \sqrt{1 + \chi^{(1)}(\omega)}. \quad (1.15)$$

In general, interactions of light and matter are dominated by the linear term of the polarisation [6], since the susceptibilities $\chi^{(i>1)}$ are becoming increasingly smaller with higher orders of i . However, for many materials the polarisability starts to saturate for high values of the electric field. If the field strength is in the order of the inner-molecular or inner-atomic fields, higher orders in Equation (1.13) cannot be neglected. The consequence of the electron response is a change of material properties which results in an indirect self-interaction of the incident pulse. It is convenient to sum up the non-linear terms of \vec{P} to

$$\vec{P}_{\text{NL}} = \epsilon_0 \left(\chi^{(2)} \vec{E} + \chi^{(3)} \vec{E}^2 + \dots \right) \vec{E}, \quad (1.16)$$

which allows us to rewrite Equation (1.11) as

$$\left(\nabla^2 - \frac{n^2}{c_0^2} \frac{\partial^2}{\partial t^2} \right) \vec{E}(\vec{r}, t) = \mu_0 \frac{\partial^2}{\partial t^2} \vec{P}_{\text{NL}}(\vec{r}, t), \quad (1.17)$$

with $n = \sqrt{1 + \chi}$. This formula illustrates that new frequency-components can emerge from the non-linear polarisations.¹⁰ Materials with an inversion symmetry will not show a susceptibility of second order due to symmetry reasons. However, there is a number of crystals without inversion symmetry, allowing high values of $\chi^{(2)}$, which can be used for frequency conversion [11].

¹⁰ New frequency-components can emerge at all possible sums of the frequencies of the applied fields

1.2.1 Frequency Conversion in Non-Linear Crystals

The most commonly used non-linear effects in matter are the generation of second harmonics, the sum-frequency generation and the difference-frequency generation. All of those effects are second order effects, for which the polarisation can be given as

$$P^{(2)}(t) = \epsilon_0 \chi^{(2)} E^2(t). \quad (1.18)$$

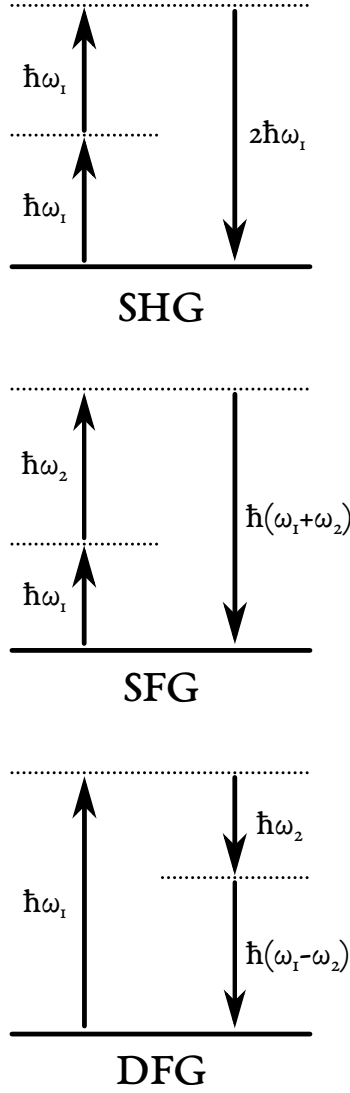


Figure 1.1: Particle interpretation of the SHG, SFG and DFG process, including virtual states.

If we consider an electric field with two frequency components ω_1 and ω_2

$$E(t) = E_1 e^{i\omega_1 t} + E_2 e^{i\omega_2 t} + c. c., \quad (1.19)$$

the resulting non-linear polarisation of second order will be

$$\begin{aligned} P^{(2)}(t) = \epsilon_0 & \left(2\chi^{(2)}(0, \omega_1, -\omega_1) |E_1|^2 + 2\chi^{(2)}(0, \omega_2, -\omega_2) |E_2|^2 \right. \\ & + \chi^{(2)}(2\omega_1, \omega_1, \omega_1) E_1^2 e^{i2\omega_1 t} + \chi^{(2)}(2\omega_2, \omega_2, \omega_2) E_2^2 e^{i2\omega_2 t} \\ & + 2\chi^{(2)}(\omega_1 + \omega_2, \omega_1, \omega_2) E_1 E_2 e^{i(\omega_1 + \omega_2)t} \\ & \left. + 2\chi^{(2)}(\omega_1 - \omega_2, \omega_1, -\omega_2) E_1 E_2^* e^{i(\omega_1 - \omega_2)t} + c. c. \right), \end{aligned} \quad (1.20)$$

where the arguments of $\chi^{(2)}(\omega_n, \omega_m, \omega_l)$ are defined as the following: ω_n will give the oscillation frequency of the polarisation while ω_m and ω_l will give the frequency components of the two incident beams. Taking a closer look, it becomes evident that light with different frequency components will be created:

1. Non-oscillating terms will create light with a DC-component. This effect is also known as optical rectification (for additional information see Section 1.3).
2. Terms proportional to $e^{i2\omega_i t}$ will create light with frequencies of $2\omega_i$. This effect is known as second harmonic generation (SHG) and is a special case of SFG with $\omega_1 = \omega_2$.
3. Terms proportional to $e^{i(\omega_1 + \omega_2)t}$ will create light with frequencies of $\omega_1 + \omega_2$. This effect is also called sum frequency generation (SFG).
4. Terms proportional to $e^{i(\omega_1 - \omega_2)t}$ will create light with frequencies of $\omega_1 - \omega_2$. This effect is also called difference frequency generation (DFG).

By moving to the particle interpretation of the photon, SHG, SFG and DFG can be viewed as the interaction of three photons, mediated by virtual states in the non-linear medium (see Figure 1.1).

An efficient generation of SHG, SFG or DFG can only be achieved, if the phase matching condition $\Delta\vec{k} = 0$ for the corresponding wave-vectors $\vec{k}_i = \frac{n}{c_0} \omega_i \hat{e}_i$ is satisfied. For SHG and SFG the phase matching condition is $\Delta\vec{k} = \vec{k}_1 + \vec{k}_2 - \vec{k}_3$. Using a collinear beam propagation, the formula simplifies to

$$\begin{aligned} \Delta k & = k_1 + k_2 - k_3 \\ & = \frac{1}{c_0} (n(\omega_1)\omega_1 + n(\omega_2)\omega_2 - n(\omega_3)\omega_3) = 0 \end{aligned} \quad (1.21)$$

If the phase matching is imperfect and $\Delta k \neq 0$, the intensity of the newly generated frequencies will drop. It can be shown, that the intensity is depending on Δk in the following manner [10]

$$I \sim \left(\frac{\sin(\Delta kz/2)}{(\Delta kz/2)} \right)^2, \quad (1.22)$$

where z is the propagated distance in the medium. The oscillating behaviour of the intensity is caused by an interference of the created wave and the fundamental. If two waves are created at the distance of $L_c = \pi/\Delta k$, destructive interference occurs and the intensity drops to zero. Therefore, L_c is also known as coherence length.

1.2.2 Second and Third Harmonic Generation

In the case of SHG, the phase matching condition can be simplified, since the frequencies can be expressed in terms of one single frequency $\omega_1 = \omega_2$ and $\omega_3 = 2\omega_1$. And so

$$n(\omega_1) - n(2\omega_1) = 0. \quad (1.23)$$

In this thesis, the third harmonic will be generated by a SFG of the fundamental and the second harmonic of a 800 nm Ti:Sapphire laser pulse. As well as in the case of the SHG, this specific case gives the opportunity to simplify the phase matching condition, since $\omega_2 = 2\omega_1$ and $\omega_3 = 3\omega_1$

$$n(\omega_1) + 2n(2\omega_1) - 3n(3\omega_1) = 0. \quad (1.24)$$

If we consider the normal dispersion regime of a medium ($\frac{d^2k}{d\omega^2} > 0$), the index of refraction increases monotonically with ω . Consequently, the phase matching conditions (1.23) and (1.24) cannot be fulfilled in such a medium. In case of the SHG phase matching, the matching condition would imply $n(\omega_1) = n(2\omega_1)$ but at the same time, the monotonically behaviour of $n(\omega)$ demands $n(\omega_1) < n(2\omega_1)$.

For the THG phase matching, the matching condition would imply $n_3 - n_2 = (n_1 - n_2) \frac{\omega_1}{\omega_3}$, but the behaviour of the index of refraction would demand $n_3 - n_2 > 0$ and $n_1 - n_2 < 0$.

For this reason, it is common to utilise the birefringence, which is the dependence of the index of refraction on the polarisation, in non-isotropic crystals. Predominantly, the non-inversion symmetric crystals that are commonly used for SHG, exhibit also birefringence.

To obtain phase matching in birefringent crystals, there are two possibilities. In both cases the polarisation of the highest frequency is chosen to experience the smallest of the two indices of refraction.

If the polarisation of signal and idler wave are the same, we define this as type-I phase matching. If their polarisations are perpendicular, it is defined as type-II phase matching [12].

In this thesis, negative uniaxial crystals will be used with a type-I phase matching for both SHG and THG. In uniaxial crystals it is possible to define a distinguished direction, which is the so called optical axis. Light that is polarised perpendicular to the plane which is stretched by the optical axis and the wave-vector \vec{k} will be refracted by the ordinary index of refraction n_o . In other words, a wave that passes the crystal along the optical axis suffers no birefringence. Light that is polarised within this plane will be refracted by the extraordinary index of refraction n_e , which is dependent on the angle between the optical axis and \vec{k} (see Figure 1.2)

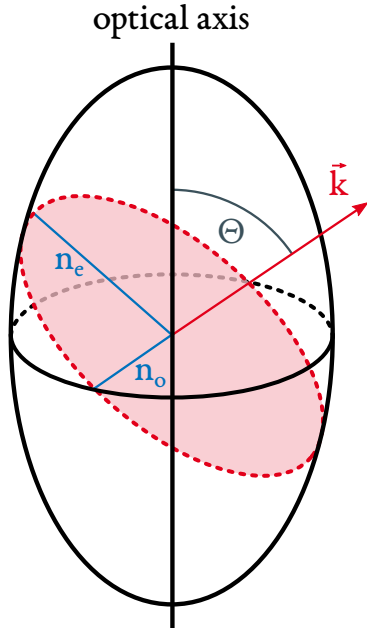


Figure 1.2: Visual representation of birefringence.

$$\frac{1}{n_e(\Theta)^2} = \frac{\sin^2(\Theta)}{n_e^2} + \frac{\cos^2(\Theta)}{n_o^2}. \quad (1.25)$$

Now it is possible to obtain phase matching with $\Delta k = 0$ for $n_e(\Theta)$ by adjusting the angle Θ . The result for SHG is

$$n_e(2\omega_1, \Theta) = n_o(2\omega_1). \quad (1.26)$$

The phase matching for THG results in

$$n_e(3\omega_1, \Theta) = n_o(\omega_1) + 2n_o(\omega_1). \quad (1.27)$$

For an efficient generation of THG it is necessary to take the possible difference of the group velocity of the two generating light pulses into account. If two pulses with group velocities $v_{G,1}$ and $v_{G,2}$ with $v_{G,1} > v_{G,2}$ travel a given distance z , the difference in arrival time is

$$\Delta t = \left(\frac{1}{v_{G,1}} - \frac{1}{v_{G,2}} \right) \times z. \quad (1.28)$$

We choose $v_{G,1}$ to be the group velocity of the generating pulse in the SHG. The fundamental pulse generates a pulse with ω_2 on the whole length of the crystal, which leads to a temporal broadening of the SHG pulse if the length of the crystal is not small compared to the pulse duration τ_1 of the generating pulse.

Therefore, it is easy to estimate the length L of a crystal for which a significant broadening would occur via [5]

$$L \ll \frac{\tau_1}{1/v_{G,2} - 1/v_{G,1}}. \quad (1.29)$$

To provide an estimate of upper bounds of crystal thicknesses, we take the group velocity difference of 400 nm and 800 nm pulses in β -barium borate, which gives $1/v_{G,400nm} - 1/v_{G,800nm} = 187 \text{ fs/mm}$ [5]. The FWHM pulse duration of the 800 nm pulses was measured to be $\sim 70 \text{ fs}$ in a previous work [13]. With this, we can estimate that the crystal thickness should be below 0.37 mm to avoid pulse broadening.

In the case of THG, it is not possible to give an easy approximation for the crystal thickness, since here the conversion efficiency is dependent of three group velocities. But as a rule of thumb, the crystal in the THG process should be $1/5$ up to $1/2$ of the thickness of that in the SHG process [14].

Having described the theoretical framework underlying the interaction of ultrashort laser pulses with matter and non-linear effects arising from those interactions, we will now focus on the description of THz radiation.

1.3 Terahertz Radiation

Most commonly, THz radiation is defined as the electromagnetic spectrum in the range of 0.1 to 10 THz.¹¹ Nowadays, there are multiple techniques to generate THz radiation with reasonable conversion-efficiencies. One of the most technical mature methods is the generation through optical rectification in organic or inorganic crystals [15, 16, 17, 18, 19, 20, 21], whereby the later will be used in this thesis. But there are also other far-developed techniques as the generation through wave mixing in plasma, photo-conductive antenna and undulators.

¹¹ Also other definitions exists, for example 10 to 30 THz

Optical rectification is a non-linear optical effect as described in Section 1.2. But it might be beneficial to treat this effect separately, since it will play a major role in the theoretical and experimental setup of this thesis. The following passages are adapted from [22], where additional information can be found.

1.3.1 Fundamental Principles of Photon-Driven THz Sources

To generate THz pulses with a carrier frequency of $\Omega/2\pi$, an electromagnetic current-density \vec{j}_{THz} with the same frequency is needed.¹² This polarisation-current can be expressed as $\vec{j}_{\text{THz}} = \partial\vec{P}_{\text{THz}}/\partial t$.

¹² As a simple example, a Hertzian dipole in a subwavelength volume can be used.

As mentioned in Section 1.2, the interaction of an electromagnetic field with high electric field strength causes the response of the medium not be proportional to the electric field. In this case, the polarisation of the medium can be described as

$$\vec{P} = \epsilon_0 \left(\chi^{(1)} + \chi^{(2)}\vec{E} + \chi^{(3)}\vec{E}^2 + \dots \right) \vec{E}. \quad (1.30)$$

In the linear response regime the frequencies of the induced dipole moments are in the order of $\mathcal{O}(100)$ THz [10]. Consequentially, THz radiation with lower or higher frequencies can only be generated in the non-linear regime.

In materials with reduced inversion symmetry, the induced polarisation scales quadratically with the field strength of the driving optical pulse.

For an optimal output of THz radiation in a beam-like shape, the spherical waves emitted from all locations inside the used material need to superimpose constructively in the desired direction. The needed phase matching conditions can be difficult to fulfil, due to different propagation velocities of THz and optical pulse.

Therefore, it is crucial for an efficient THz output to use media with a high non-linear optical response and the potential to achieve phase matching over large optical and THz bandwidths. Properties of the most commonly used materials for THz generation based on optical rectification can be found in Table 1.1, where d_{eff} gives the effective non-linear coefficient, n_{IR} and n_{THz} the refractive index at 800 nm and 1 THz respectively, α_{THz} the absorption coefficient again at 1 THz and the figure of merit is defined as $\text{FOM} = \frac{d_{\text{eff}}^2}{n_{\text{IR}}n_{\text{THz}}}$.

Table 1.1: Parameters of commonly used materials for THz generation based on optical rectification

Material	d_{eff} [$\frac{\text{pm}}{\text{V}}$]	n_{IR}	n_{THz}	α_{THz} [$\frac{1}{\text{cm}}$]	FOM [$\frac{\text{pm}^2}{\text{V}^2}$]
GaAs	65.6	4.18	3.61	0.5	87.9
GaP	24.6	3.57	3.34	1.9	18.2
ZnTe	68.5	3.31	3.17	1.3	180
LiTaO ₃	161	2.22	6.42	46	882
LiNbO ₃	168	2.23	5.16	16	1170

1.3.2 Optical Rectification as Source for THz Radiation

As mentioned in Section 1.3.1, optical rectification is a second order non-linear effect and can be seen as a special case of DFG, where spectral components ω and $\omega + \Omega$ from one broadband pulse are mixed by DFG. Employing a different reference frame, OR¹³ can be seen as an intrapulse DFG, as in contrast to the classical interpulse DFG, where two separate pulses with different carrier frequencies are needed (see Figure 1.3).

¹³ OR: Optical Rectification

If $\chi^{(2)}$ is flat in ω , the newly generated spectral components Ω result in a single-cycle pulse with a temporal shape that is proportional to the time derivative of the intensity envelope of the pump pulse, featuring a fixed carrier envelope phase. There are multiple equivalent representations for the non-linear THz polarisation, generated by the driving field

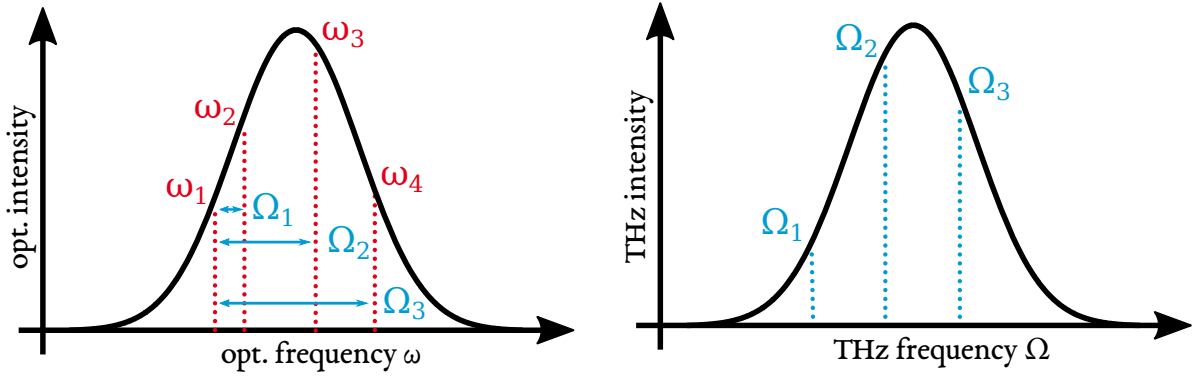
$$\begin{aligned}
 P_{\text{THz}}(\Omega) &= 2\epsilon \int_0^\infty d_{\text{eff}} E(\omega + \Omega)_{\text{Opt.}} \bar{E}(\omega)_{\text{Opt.}} d\omega \\
 &\sim \epsilon_0 \Omega d_{\text{eff}} E(\omega + \Omega)_{\text{Opt.}} E(\omega)_{\text{Opt.}},
 \end{aligned} \tag{1.31}$$

where ϵ_0 denotes the vacuum permittivity and $\bar{E}(\omega)$ the complex conjugate of the pump pulse $E(\omega)$ in frequency-space.

An optimal THz generation can only be obtained when the phase matching condition $\Delta k = 0$ between driving and THz field is fulfilled

$$\begin{aligned}\Delta k &= k(\Omega) + k(\omega) - k(\omega + \Omega) \\ &\approx k(\Omega) - \Omega \left. \frac{\partial k}{\partial \omega} \right|_{\omega_0},\end{aligned}\quad (1.32)$$

where ω_0 denotes the central frequency of the pump pulse. The second equation only holds true if $\Omega \ll \omega$ is assumed. But if we consider a pump pulse in the optical spectrum, this is naturally satisfied.



If we rewrite Equation (1.32) for collinear phase matching, we obtain the following relation

$$\Delta k = |\Delta k| = \frac{\Omega}{c_0} [n(\Omega) - n_g(\omega_0)], \quad (1.33)$$

where c_0 denotes the vacuum speed of light, n the refractive and n_g the group index. The phase matching condition is equivalent to a velocity matching condition, that can be expressed as

$$v(\Omega) = v_g(\omega_0), \quad (1.34)$$

where $v = \frac{c}{n}$ is the phase velocity and $v_g = \frac{c}{n_g}$ is the group velocity.

1.3.3 Tilted-Pulse-Front Pumping

In most cases, it is not possible to achieve collinear phase matching in materials that are commonly used for THz generation, as most of these materials are optical isotropic¹⁴ and thus missing birefringence.

Therefore, it is only possible to achieve phase matching for specific pump wavelengths and THz frequencies.¹⁵

To fulfil the phase matching conditions for other wavelengths and in different materials, a non-collinear approach can be taken.

Figure 1.3: Schematic illustration of THz generation through intrapulse DFG

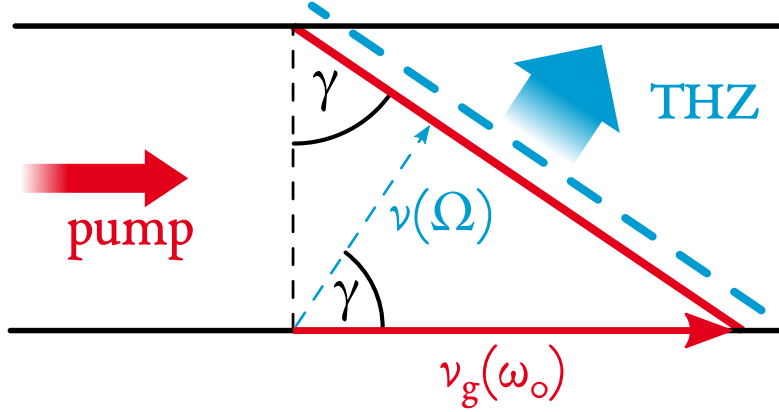
¹⁴ A prominent counterexample is the THz generation in GaSe, which exhibits a natural birefringence.

¹⁵ ZnTe can be pumped with 800 nm pulses to generate radiation with a frequency of 1 THz.

¹⁶ **TPFP: Tilted-Pulse-Front Pumping**

In the TFP, the pump pulse propagates with a tilted intensity front inside the non-linear medium [23], where the angle between phase-front and pulse-front is γ . The THz field is generated by the induced polarisation alongside the pulse-front of the driving field. Due to the Huygens principle, the partial waves of the THz radiation interfere constructively and a strong THz field can form parallel to the tilted pulse-front of the driving field. A schematic illustration of this process can be found in Figure 1.4.

Figure 1.4: Schematic representation of tilted-pulse-front pumping, where the tilted pulse front (solid red line) of the driving field creates a non-tilted pulse-front (dashed blue line) in the THz pulse.



This configuration has the great practical advantage to enable an achromatic phase matching, while being scalable to high THz pulse energies by illuminating a larger pumped area.

In the TFP configuration, a slightly different phase matching condition has to be fulfilled compared to the colinear case

$$\nu(\Omega) = v_g(\omega_0) \cos(\gamma). \quad (1.35)$$

Here the projected group velocity of the driving field has to match the THz phase velocity, which can only be fulfilled, if the THz phase velocity is smaller or equal to the pump pulse group velocity.

Another description of this condition can be formulated as

$$\tan(\gamma) = -\frac{n}{n_g} \lambda \frac{\partial \epsilon}{\partial \lambda'}, \quad (1.36)$$

where $\epsilon(\omega)$ describes the propagation angle with respect to the beam propagation direction z (see Figure 1.5).

1.3.4 Material Selection

To select the right material for THz generation through optical rectification, different criteria have to be taken into account, for example the

central wavelength of the pump pulse or its intensity. Therefore, it can be informative to calculate the efficiency of the THz generation during phase matching [24]

$$\eta(\Omega) = \frac{2\Omega^2 d_{\text{eff}}^2 L^2 I}{\epsilon_0 c^3 n^2(\omega_0) n(\Omega)} \frac{\sinh^2 [\alpha(\Omega)L/4]}{[\alpha(\Omega)L/4]^2} \exp[-\alpha(\Omega)L/2]. \quad (1.37)$$

In this case, L is the material length, I the pump pulse intensity and $\alpha(\Omega)$ the THz absorption coefficient. It is evident, that for a high THz generation efficiency, a large non-linear coefficient d_{eff} , a high pumping intensity and a small absorption coefficient are favourable. The quadratic response of η to the THz frequency implies considerable higher efficiencies for higher THz frequencies, which makes it challenging to generate high THz outputs near the microwave regime.

Another desirable characteristic of a potential pumping material is

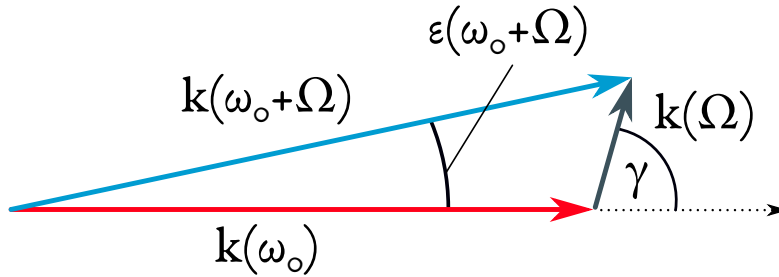


Figure 1.5: Phase matching in the non-collinear TFP configuration.

a high damage threshold, which allows the use of high intensities in the driving field. It might also be advantageous to use materials with a similar refractive index in the THz regime as well as in the regime of the pumping wavelength, to be able to either utilise a collinear pumping or to use only slightly tilted pulses in the TFP configuration.

Even though not all mentioned criteria are fulfilled, one of the most commonly used materials for THz generation is LiNbO_3 , which will be discussed in the next section for it will be used in this thesis to generate near single-cycle THz pulses.

1.3.5 THz Generation in Lithium Niobate

The optical rectification in LiNbO_3 is dominated by cascaded parametric generation [25], where simultaneous quasi-phase-matching of optical parametric generation and sum-frequency generation leads to the generation of THz radiation. This section will be orientated on [26], where also additional information can be found.

In LiNbO_3 the non-linear coefficient is dominated by the largest element of the non-linear susceptibility tensor χ_{333} . Both are connected by the following relationship: $d_{33} = 1/2 \chi_{333}^{(2)}(\Omega)$.

As depicted in Table 1.1, LiNbO₃ exhibits a relatively high non-linear coefficient. This is favoured by a resonance in the THz range. The frequency dependence of this resonance is given by

$$\chi_i(\Omega) = \chi_{i0} \left[1 - \frac{\Omega^2}{\omega_i^2} + \frac{i\gamma\Omega}{\omega_i^2} \right]^{-1}, \quad (1.38)$$

where $\chi_{i0} = 23.36$, $\gamma = 0.34$ THz and $\omega_i/2\pi = 7.6$ THz. With this, the non-linear coefficient can be given by

$$\begin{aligned} d_{33}(\Omega) &= \frac{1}{2} \left[\delta_{eee}(\Omega)\chi_e^2(\Omega)\tilde{\chi}_e(\Omega) + \delta_{iee}(\Omega)\chi_i(\Omega)\chi_e\tilde{\chi}_e(\Omega) \right] \\ &= 168 \frac{\text{pm}}{\text{V}}, \end{aligned} \quad (1.39)$$

with $\delta_{eee} = 0.761$ pm/V and $\delta_{iee} = 0.421$ pm/V are the electronic and mixed ionic terms and $\chi_e = 3.674$ (if $\Omega \sim \mathcal{O}(\text{THz})$). The value of $d_{\text{eff}} = d_{33} = 168$ pm/V is higher than for most semiconductors, which range from $d_{\text{eff}} = 25 - 80$ pm/V but smaller than that of organic crystals like DAST or BAN [20]. But in most cases, the damage threshold for those materials is below that of LiNbO₃, which is in the order of 100 GW/cm^2 . To further increase the damage threshold, it is common to dope the LiNbO₃-crystal with MgO, which significantly reduces photo-refractive damage. The optimal doping concentration varies for the two different lithium niobate forms and was determined to be 0.7% for stoichiometric (sLN) and 6.0% for congruent lithium niobate (cLN) [27].

¹⁷ MPA: Multi Photon Absorption

Despite being able to be pumped with high field strength, MPA effects¹⁷ are negligible in LiNbO₃, as it is an insulator with a relatively large band gap of 3.8 eV. Contrariwise, THz absorption is a dominant effect, since lithium niobate features a relatively high absorption coefficient of 17 cm^{-1} at 1 THz at 300 K. The absorption coefficient can be reduced to below 5 cm^{-1} by reducing the crystal temperature to cryogenic temperatures [28].

Another dominant absorption process during THz generation is the absorption of phonons, which limits the output frequency below 4.5 THz [29].

The strong contribution of lattice vibrations to the dielectric function is also responsible for the fact that phase matching by angle tuning, utilising the birefringence of lithium niobate, is not possible below the transverse-optical phonon frequency. The dielectric function can be estimated by [30]¹⁸

¹⁸ ϵ_s , A_j , ω_j and γ_j are properties of the crystal and depend on the chosen oscillator model

$$\epsilon(\Omega) = \epsilon_s + \sum_j A_j \frac{\omega_j^2}{\omega_j^2 - \Omega^2 - 2i\gamma_j\Omega}. \quad (1.40)$$

With this it is also possible to write the absorption coefficient as $\alpha(\Omega) = 2\pi\Omega \text{Im} \sqrt{\epsilon}$ and the refractive index as $n(\Omega) = \text{Re} \sqrt{\epsilon}$.

The lattice vibrations are also responsible for the large difference between optical group velocity and THz phase velocity, which leads to the necessity of large tilted pulse-front angles of $\gamma = 63^\circ$.

1.3.6 Detection of Terahertz Radiation

Since THz waves occupy frequencies in between the microwave range (where waves can be detected by charge acceleration) and the NIR¹⁹ (where waves can be detected by the band gap of materials), it is meticulously hard to detect and characterise THz waves with the techniques available at the moment.

One of the most commonly used techniques to characterise THz pulses is the EOS,²⁰ which exploits the Pockels effect.

For weak electric fields, the relationship between induced polarisation and electric field for an anisotropic material is given by the tensor equation

$$P = \epsilon_0 \chi_{ij} E_j. \quad (1.41)$$

For an easier interpretation, the general χ_{ij} can be diagonalised to match the principal axes of the material, which will result in the following form

$$\chi_{ij} = \begin{pmatrix} \chi_{11} & 0 & 0 \\ 0 & \chi_{22} & 0 \\ 0 & 0 & \chi_{33} \end{pmatrix}. \quad (1.42)$$

If at least one of the tensor entries varies from the other entries, the material is birefringent.

It might be of interest to rewrite Equation (1.41) as the electric displacement field D_{ij}

$$D_{ij} = \sum_j \epsilon_{ij} E_j, \quad (1.43)$$

where the permittivity ϵ_{ij} is defined by

$$\epsilon_{ij} = 1 + \chi_{ij}. \quad (1.44)$$

If now an electromagnetic wave with a given polarisation travels through such an anisotropic medium, the polarisation of the transmitted wave changes, if its original polarisation is not parallel to one of the optical axis of the medium.

Otherwise, the wave exhibits extraordinary and ordinary components, which propagate with different velocities through the material, which eventually lead to phase shifts between the components and finally a change in polarisation after the transmission.

¹⁹ **NIR: Near Infra Red**
usually defined as the spectral region of
780 nm to 1450 nm

²⁰ **EOS: Electro Optical Sampling**

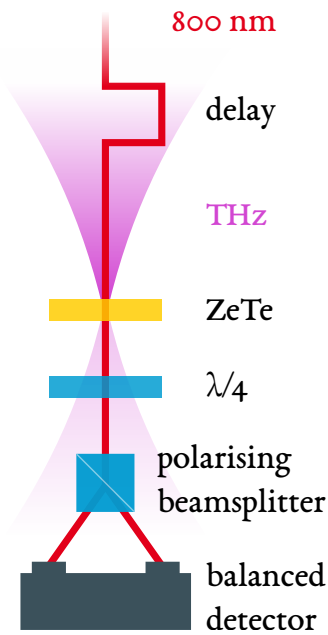


Figure 1.6: Schematic illustration of the EOS methodology.

$${}^{21}\eta_{ij} = \eta_{ji}$$

If we now turn the attention to strong electric fields, we can recall from Equation (1.13) that it might be favourable to express the polarisation P as a Taylor expansion. Since we stated that the EOS uses the Pockels effect, which is a second order effect, we can truncate the Taylor expansion after the second term. With relation (1.15) and (1.44), we can now quantitate the change of the refractive index, induced by the Pockels effect

$$\begin{aligned} n^2 &= \epsilon = 1 + \chi \\ &= 1 + \chi^{(1)} + \chi^{(2)}E + \dots \\ &= n_0 + \chi^{(2)}E \\ &= (n_0 + \Delta n)^2 \\ &\approx n_0^2 + 2n_0\Delta n \end{aligned} \quad (1.45)$$

and the second order polarisation [10]

$$\begin{aligned} P_i^{(2)}(\omega) &= 2 \sum_{j,k} \epsilon_0 \chi_{ijk}^{(2)}(\omega, \omega, 0) E_j(\omega) E_k(0) \\ &= \sum_j \chi_{ij}^{(2)}(\omega) E_j(\omega), \end{aligned} \quad (1.46)$$

whereby $\chi_{ij}^{(2)}(\omega) = 2 \sum_k \chi_{ijk}^{(2)}(\omega, \omega, 0) E_k(0)$ denotes the susceptibility-tensor induced by the field [31] and $E_k(0)$ the electric field of the THz beam.

In the majority of cases, a pump beam in the NIR range is used, resulting in a difference in pump and probe frequencies of three orders of magnitude. Hence, the assumption $E_k(\omega) = E_k(0)$ can be made. From Equation (1.46) it follows, that a static field induces birefringence in an anisotropic medium, that is proportional to the field strength. Vice versa it is possible to determine the field strength by measuring the induced birefringence in a medium. By rearranging Equation (1.43), we can express the field components of the probing beam as

$$E_i = \sum_j \eta_{ij} D_j, \quad (1.47)$$

where $\eta_{ij} = 1/\epsilon_{ij}$ denotes the real and symmetric²¹ impermeability tensor, which is related to the electric field via the electro-optical tensor r_{ijk}

$$\eta_{ij} = \sum_k r_{ijk} E_k. \quad (1.48)$$

It is possible to contract the tensor to $\eta_l = \sum_k r_{lk} E_k$, where the index l runs over its six independent entries.

It is now possible to quantitate the change of the refractive index, generated by the nearly constant THz field

$$\Delta n_l = \sqrt{\frac{1}{\sum_{k=1}^3 r_{lk} E_k}}. \quad (1.49)$$

The standard setup to detect such a change would consist of an electro-optical crystal, followed by a $\lambda/4$ -plate for the probe beam, a polarising beam splitter and two photo detectors. If now the THz pulses and the probe beam are spatio-temporal overlapped inside the crystal, the THz field leads to a change in the refractive index, which changes the polarisation of the probe pulse from linear to elliptical. After passing through the $\lambda/4$ -plate, the probe pulse is no longer circular polarised and thus induces different intensities in the photo detectors (see Figure 1.6).

By varying the arrival time of THz and probe beam, it is possible to raster the amplitude and phase of the THz pulse. Due to its optical properties, ZnTe (see Table 1.1) is the most commonly used material for EOS setups. The electro-optical tensor of ZnTe consists of only one distinct entry

$$r_{lk} = r_{41} \begin{pmatrix} \mathbf{0}_{3 \times 3} \\ \mathbf{1}_{3 \times 3} \end{pmatrix}. \quad (1.50)$$

As given in [26], the intensity difference for each polarisation component is given by²²

$$\Delta I(\alpha, \phi) = I_p \frac{\omega n^3 E_{\text{THz}} r_{41} L}{2c} (\cos(\alpha) \sin(\phi) + 2 \sin(\alpha) \cos(2\phi)), \quad (1.51)$$

if $n^2 E_{\text{THz}} r_{41} \ll 1$ holds true. If the trigonometric functions are maximised and parameters²³ for an EOS setup with a ZnTe crystal and a 800 nm probe beam are inserted into formula (1.51), the THz field strength can be calculated by

$$E_{\text{THz}} [\text{MV/m}] = \frac{1.36}{L [\text{mm}]} \frac{\Delta I_{\text{max}}}{I_p}. \quad (1.52)$$

It is worth noting, that the given formula is only valid for small changes in intensity ($I_{\text{max}} \ll I_p$).

After discussing the interaction of electromagnetic waves with matter, we will now focus on the interactions of electrons with matter.

1.4 Electron Interactions

Before describing the interaction of electrons with matter, we will shortly describe the photoelectric effect that will be used in this thesis to generate the electron pulses of the electron gun.

1.4.1 Photoelectric Effect

The photoelectric effect can be viewed as a special form of ionisation in which the energy needed to generate a free electron is reduced due to the confinement of the atoms in a solid.

22

I_p = probe beam intensity
 ω = probe beam frequency
 L = crystal thickness
 α = angle between THz pol.
 and [110]-axis of crystal
 ϕ = angle between probe pol.
 and [110]-axis of crystal

23

$\alpha = 0^\circ$
 $\phi = 0^\circ$ or 90°
 $\omega = 2.36 \times 10^3$ THz
 $r_{41} = 4.04$ pm/V
 $n = 2.854$

For a single atom ionisation, energies in the range of 4.07 eV – 24.58 eV are needed, while free electrons generated by the photoelectric effect on material surfaces only require 1.95 eV – 5.93 eV [32].

The photoelectric effect was first described by H. Hertz in 1887 [33]. He investigated the release of electrons from a metal surface via UV radiation. His results can be summarised in four major statements:

- The photoelectric effect is only present above a distinct threshold frequency ν_g of the light. This threshold is specific for different metals.
- The kinetic energy of the electrons is set by the frequency of the beam.
- For $\nu \geq \nu_g$ the number of emitted electrons is proportional to the intensity of the beam.
- The photoelectric effect takes place on timescales below 1 ns.

These findings were later summarised by A. Einstein in his *Lichtquantenhypothese* in 1905 [34] which was based on the work of M. Planck. If light with the frequency ν interacts with matter, only energy quanta of

$$E = h\nu \quad (1.53)$$

can be transferred. The maximum kinetic energy K_{\max} of an ejected electron is given by

$$K_{\max} = h\nu - \phi, \quad (1.54)$$

where h is the Planck constant and ν is the frequency of the incident photon. The term ϕ is the work function, which gives the minimum energy required to remove an electron from the surface of the metal. The work function satisfies

$$\phi = h\nu_g. \quad (1.55)$$

Therefore, only photons with a frequencies higher than ν_g can trigger the photoelectric effect. It is however possible to achieve photoionisation with photons below the critical energy. If the photon density is high enough, non-linear effects can trigger the photoelectric effect as well.

1.4.2 Non-Linear Photoionisation

There are two possible scenarios in which it is possible to ionise matter with photon energies below the work function. The first one is MPI²⁴ while the other is TI.²⁵ In the first case, an outer-shell electron is

²⁴ **MPI:** Multi-Photon Ionisation

²⁵ **TI:** Tunnel Ionisation

absorbing multiple photons at the same time to accumulate enough energy to leave the atom. It is evident, that this effect can only occur, if the photon density is high enough. In the second case, the high field strength of the driving electromagnetic field is able to deform the potential of the atom in such a way, that electrons are able to tunnel through the remaining potential barrier. To estimate, which effect will be more likely, we can use the Keldysh parameter [35], which is given by

$$\gamma^2 = \frac{E_b}{2U_p}, \text{ with } U_p = \left\langle \frac{1}{2} m_e v^2(t) \right\rangle = \frac{e^2 I}{2c_0 \epsilon_0 m_e \omega^2}. \quad (1.56)$$

The Keldysh parameter is depending on the binding energy E_b of the electron and the ponderomotive potential U_p , which is a measure for the mean potential energy that the electron is accumulating in the field of the driving electromagnetic wave. If $\gamma^2 \gg 1$ multi-photon ionisation dominates, while tunnel ionisation dominates for $\gamma^2 \ll 1$.

Having established the generation of free electrons through the photoelectric effect, we will now turn to the interaction of free electrons with matter.

1.4.3 Bethe Formula

If Auger electrons are generated in solids, they can only be detected if the origin of their generation is near the surface ($\mathcal{O}(\text{nm})$) of the material. To understand this fact, we will first address the energy loss of fast charged particles in matter.

The first attempts to describe this phenomenon was made by N. Bohr in 1913 [36, 37], in which relativistic or quantum mechanic effects were not taken into account. Both were later implemented by H. Bethe [38, 39].

In the more general case of heavy charged particles like protons, α -particles or atomic nuclei, we can describe their mean energy loss by the Bethe formula, which is given by²⁶

$$-\left\langle \frac{dE}{dx} \right\rangle = \frac{4\pi}{m_e c^2} \frac{nZ^2}{\beta^2} \left(\frac{q_e^2}{4\pi\epsilon_0} \right)^2 \left[\ln \left(\frac{2m_e c^2 \beta^2}{I(1-\beta^2)} \right) - \beta^2 \right]. \quad (1.57)$$

In the Bethe-Bloch approximation, fast charged particles interact with the electrons of the matter they pass through. By elevating the energy state, or ionising the atoms, the incoming particles transfer energy to the material and thus experience an energy loss.

For particles with $\beta \ll 1$, Equation (1.57) simplifies to

$$-\frac{dE}{dx} = \frac{4\pi n Z^2}{m_e v^2} \left(\frac{e^2}{4\pi\epsilon_0} \right)^2 \left[\ln \left(\frac{2m_e v^2}{I} \right) \right]. \quad (1.58)$$

²⁶

v = speed of particle
 q_e = charge
 E = energy
 I = mean excitation potential
 x = traveling distance
 $n = \frac{N_A Z \rho}{A M_u}$
 = electron number density
 ρ = material density
 Z = atomic number
 A = atomic mass
 N_A = Avogadro number
 M_u = Molar mass constant
 $\beta = \frac{v}{c}$

²⁷ Z^3 : Barkas-Andersen correction
 Z^4 : Bloch correction

Being derived by quantum mechanical perturbation theory, the expression is proportional to the square of Z . Taking higher orders into account²⁷ the description can be further improved.

Nonetheless, Equation (1.57) is only valid for the interaction of heavy charged hadrons with matter and not for those of electrons and matter. This is due to the fact that the scattered electrons are indistinguishable from the electrons of the material. Furthermore, they are significantly lighter than for example protons, and therefore need corrections for Bremsstrahlung and relativistic effects.

1.4.4 Berger-Seltzer Formula

To address the energy loss of electrons in matter we have to employ the Berger-Seltzer formula. For every energy loss process there are two regimes that have to be taken into account. Being continuous below a given threshold, the energy loss is discrete above aforementioned threshold, due to the production of secondary particles. Since the regime of discrete loss is by far above any energy level of atomic shells, we are only interested in the continuous case. Considering the differential cross section per atom with atomic number Z for the ejection of a secondary particle with kinetic energy K by an incident particle of total energy E moving in a material of density ρ , we obtain

$$\frac{d\sigma(Z, E, K)}{dK}. \quad (1.59)$$

In the case of an incoming particle with kinetic energy below the threshold K_{cut} , we observe the creation of low energetic secondary particles and a continuous energy loss that can be described by

$$\frac{dE_{\text{low}}(E, K_{\text{cut}})}{dx} = n_{\text{at}} \int_0^{K_{\text{cut}}} \frac{d\sigma(Z, E, K)}{dK} K dK, \quad (1.60)$$

where n_{at} is the number of atoms per volume in the material.

The maximal transferable energy of a free electron or positron is given by

$$K_{\text{max}} = \begin{cases} E - m_e c^2, & \text{for } e^+ \\ (E - m_e c^2)/2, & \text{for } e^- \end{cases} \quad (1.61)$$

where m_e is the electron resting mass. By integrating Equation (1.60), we arrive at the Berger-Seltzer formula [40], which gives us the mean energy loss per unit length in a given material²⁸

$$\left. \frac{dE}{dx} \right|_{K < K_{\text{cut}}} = 2\pi r_e^2 m_e c^2 n_{\text{el}} \frac{1}{\beta^2} \left[\ln \frac{2(\gamma + 1)}{(I/mc^2)^2} + F^\pm(\tau, \tau_{\text{up}}) - \delta \right]. \quad (1.62)$$

$r_e = e^2 / (4\pi\epsilon_0 m_e c^2)$
 = classical electron radius
 $n_{\text{el}} = Z n_{\text{at}} = Z \frac{N_A \rho}{A}$
 = electron density in the material
 $I =$ mean excitation energy
 $\gamma = E / (m_e c^2)$
 $\beta^2 = 1 - (1/\gamma^2)$
 $\tau = \gamma - 1$
 $K_{\text{cut}} =$ minimum energy cut
 $\tau_c = K_{\text{cut}} / (m_e c^2)$
 $\tau_{\text{max}} =$ maximum energy transfer
 $\tau_{\text{up}} = \min(\tau_c, \tau_{\text{max}})$
 $\delta =$ density effect function

28

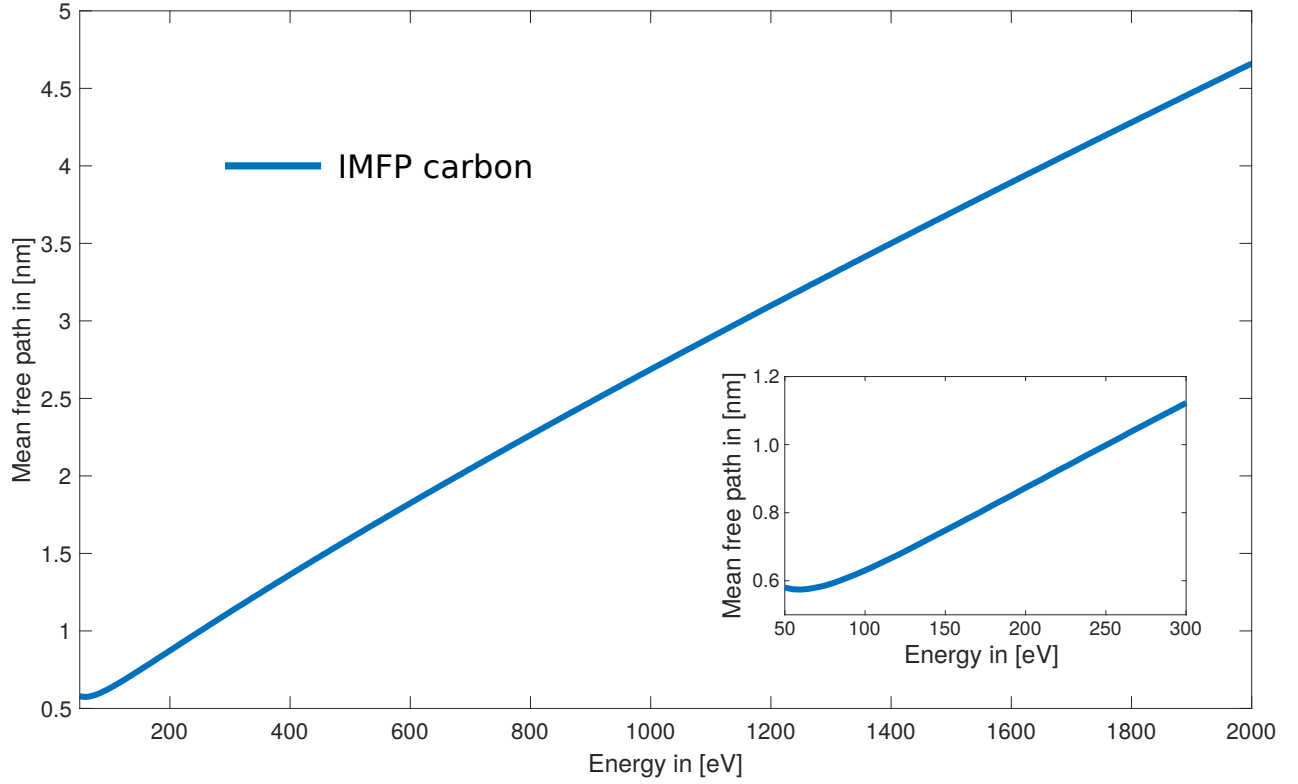


Figure 1.7: Monte Carlo simulation of the inelastic mean free path of electrons in carbon. Data taken from [41].

The functions F^\pm are given by

$$\begin{aligned}
 F^+(\tau, \tau_{\text{up}}) &= \ln(\tau \tau_{\text{up}}) - \frac{\tau_{\text{up}}^2}{\tau} \left[\tau + 2\tau_{\text{up}} - \frac{3\tau_{\text{up}}^2 y}{2} - \left(\tau - \frac{\tau_{\text{up}}^3}{3} \right) y^2 \right. \\
 &\quad \left. - \left(\frac{\tau_{\text{up}}^2}{2} - \tau \frac{\tau_{\text{up}}^3}{3} + \frac{\tau_{\text{up}}^4}{4} \right) y^3 \right] \\
 F^-(\tau, \tau_{\text{up}}) &= -1 - \beta^2 + \ln[(\tau - \tau_{\text{up}})\tau_{\text{up}}] + \frac{\tau}{\tau - \tau_{\text{up}}} \\
 &\quad + \frac{1}{\gamma^2} \left[\frac{\tau_{\text{up}}^2}{2} + (2\tau + 1) \ln \left(1 - \frac{\tau_{\text{up}}}{\tau} \right) \right].
 \end{aligned} \tag{1.63}$$

With this tool, we are now able to determine the inelastic mean free path of electrons in matter. Showing an exemplary dataset for the inelastic mean free path of electrons in carbon, Figure 1.7 illustrates, that even for electrons with kinetic energies around 2 keV, the mean free path is only in the order of a few nm.

With this insight, we can understand why Auger electrons originating from solids can only be obtained from the surface layer of the material.

On the one hand, this relation hampers us from gaining access to Auger electrons from deep inside of solids, but on the other hand, it gives us access to an extremely surface-sensitive spectroscopy method, which will be discussed in the next section.

1.5 Auger electrons

In the Auger process is a special case of a radiation-free double ionisation and was first discovered by L. Meitner [42] and later independently by P. V. Auger [43].

The Auger effect can be described in a two step model. In the first step, the atom undergoes a single ionisation, which can be caused by a high energy photon or the collision with electrons or other particles. In the second step, the vacancy is filled by an electron from a higher shell. The excess energy can either be radiated by a photon or by a second electron, which is the Auger electron. The kinetic energy of the Auger electron is defined by the energy difference of the single and the double ionised state and is thereby independent of the energy of the triggering photon or the kinetic energy of the electron that is initiating the Auger process. The probability of such a radiation-free transition for binding energies below 1 keV²⁹ of the primary ionisation is significantly higher than for transitions that feature a photon [44]. The spectral distribution of Auger electrons is described by a Lorentz profile with the spectral width Γ , which is related to the lifetime τ_A of the vacant state by the time-energy uncertainty by

$$\tau_A = \frac{\hbar}{\Gamma}, \quad (1.64)$$

where \hbar is defined as $\hbar = h/2\pi = 6.58 \times 10^{-16}$ eVs. Typical lifetimes are in the order of attoseconds to a few femtoseconds, while the spectral widths are in the order of a few millielectronvolt up to several electronvolt.

There are several effects that can influence the spectral appearance of an Auger spectrum. A possible scenario is the so-called shake-up transition. Here the almost instantaneous distortion of the Coulomb potential due to the emission of the core-electron can cause the transition of a valance electron to an unoccupied higher shell. This process happens at the same time as the emission of the photoelectron [45]. By the shake-up, the kinetic energy of the core-electron is reduced by the excitation energy of the valance electron, which results in additional peaks in the overall spectrum. Another effect that can change the appearance of an Auger spectrum is the so called PCI.³⁰ A PCI can occur, when the kinetic energy of the Auger electron is higher than the energy of the primary ejected photoelectron. In this case, the Auger electron

²⁹ For atoms with $Z < 70$ the Auger process dominates, while for $Z > 70$ fluorescence is the dominant effect.

³⁰ PCI: Post-Collision-Interaction

overtakes the photoelectron, which results in a change of the potential that the Auger electron is exposed to. It changes from a double ionised potential to a single ionised potential. By this, an energy transfer from the photoelectron to the Auger electron takes place, with a higher transfer, the closer the interaction takes place to the ion [46]. The PCI-effect is especially pronounced when the energy of the photon energy approaches the binding energy of the initial photonelectron, which results in shifts and deformations in the Auger peaks in measured spectra.

1.6 Light Field Driven Streaking

To gain access to the temporal scales on which an Auger decay takes place, this thesis will rely on the technique of a light field driven streaking camera. Here, the temporal profile of the Auger decay is mapped to the energy change of the Auger electrons which is dependent on the phase of the THz pulse during the decay.

A classical streaking camera is used to map the temporal profile of an electromagnetic pulse to a spatial distribution. The technical approach in this case is, that a light pulse generates a direct replica of itself, by producing photoelectrons in a cathode. Those electrons are then deflected by a variable electric field onto an electron-sensitive screen. In case of a conventional light field driven streaking camera, the varying electric field is replaced by another electromagnetic pulse,³¹ which is copropagating with the primal pulse. If both pulses are spatio-temporally overlapped in a gas target, the temporal profile of the shorter pulse can be mapped to an energy shift of the photoelectrons created in the target.

Since the oscillation period of the streaking field should exceed the duration of the investigated pulse or the exploited electron dynamic (photoionisation, Auger decay etc.) by at least a factor of four, it is common practice to use NIR or THz pulses to drive the streaking process.

In the following, a classical description of the streaking process is given to introduce the matter, followed by a quantum-mechanical delineation to gain a more detailed understanding.³²

1.6.1 Classical Approach

In the classical approach, the ionisation through the XUV pulse is considered independent from the following acceleration in the streaking field. In this case neither the THz field influences the ionisation by the XUV pulse, nor does the XUV pulse influence the free electron [47].

³¹ The oscillation period of the added pulse has to be longer than the temporal profile of the first pulse

³² In a conventional streaking-setup XUV pulses are used to initialise photoionisation or additional Auger-decay. Those pulses are then streaked by THz pulses. In this thesis electron pulses will be used to trigger the Auger decay, but the underlying principle is equivalent.

If an electron is ionised at t_i in the presence of linear polarised electric field $E(t)$, the momentum change due to that field is given by

$$\Delta p(t_i) = q_e \int_{t_i}^{\infty} E(t) dt = q_e A(t_i), \quad (1.65)$$

$$p = p_0 + \Delta p(t_i). \quad (1.66)$$

where $A(t)$ denotes the vector potential of the streaking field, p the final momentum and p_0 the initial momentum. The total change of momentum depends on the angle between the initial momentum and the streaking field. By this, the final kinetic energy of a streaked electron is given by

$$\begin{aligned} W_{\text{kin}} &= \frac{|\vec{p}|^2}{2m_e} \\ &= W_0 + 2U_p \cos(2\Theta) \sin^2(\phi_i) \\ &\quad \pm \sqrt{1 - \frac{2U_p}{W_0} \sin^2(\Theta) \sin^2(\phi_i)} \sqrt{8W_0 U_p \cos(\Theta) \sin^2(\phi_i)}, \end{aligned} \quad (1.67)$$

where W_0 describes the initial kinetic energy, U_p the ponderomotive potential, Θ the angle between the initial momentum and the streaking field and ϕ_i the phase of the streaking field at the moment of ionisation. Considering the two extreme cases in which the initial momentum is either perpendicular or parallel to the polarisation of the streaking field, Equation (1.67) simplifies to

$$\begin{aligned} W_{\text{kin}}^{\parallel} &= W_0 + 2U_p \sin^2(\phi_i) \pm \sqrt{8W_0 U_p} \sin(\phi_i) \\ W_{\text{kin}}^{\perp} &= W_0 - 2U_p \sin^2(\phi_i). \end{aligned} \quad (1.68)$$

Since predominantly, the kinetic energy of the electrons is much greater than the ponderomotive potential the term $2U_p \sin^2(\phi_i)$ can be neglected. Only electrons with initial momentum parallel to the field polarisation experience an energy shift of

$$\begin{aligned} \Delta W_{\text{kin}} &= W_{\text{kin}} - W_0 \\ &\approx \sqrt{8W_0 U_p} \sin(\phi_i) \\ &= e \sqrt{\frac{2W_0}{m_e}} A(t_i). \end{aligned} \quad (1.69)$$

With this, we illustrated that in the small-angle approximation the ionisation time is mapped onto the kinetic energy of the electrons.

However, this holds only true if the initial momentum of the electrons is delta-distributed. In the case of streaked photoelectrons this condition is not fulfilled, since their energy is determined by the spectral

distribution of the ionising XUV pulse. Therefore, only a convolution of the spectral width and the duration of the XUV pulse can be determined. As the energy of Auger electrons is only determined by the natural linewidth of the corresponding decay, Equation (1.69) is a sufficient approximation. In the quantum mechanical description, the exponential decay characteristic of an electron hole transfers to the wave packet of an Auger electron. Considering that the generating pulse exhibits a temporal width, the streaked Auger spectrum is a convolution of the temporal profile of the exciting pulse and the exponential decay of the Auger electrons. Since in most cases the duration of the generating pulses is longer than the decay time of the Auger process, the mathematical description for photoelectrons and Auger electrons is identical.

To gain a more complete understanding of the streaking process, we now switch to a quantum mechanical description. Here we are able to reconstruct the XUV or electron pulses by analysing spectra in the presence and absence of a streaking field.

1.6.2 Quantum Mechanical Approach

In the quantum mechanical approach the electrons created during ionisation are not described as particles, but as wave packets $|\Psi(t)\rangle$, for which the time-dependent Schrödinger equation is defined as

$$i \frac{d}{dt} |\Psi(t)\rangle = \hat{H}(t) |\Psi(t)\rangle. \quad (1.70)$$

The Hamiltonian of the streaking process can be written as

$$\hat{H}(t) = 1/2 (\hat{p} + A(t)_{\text{STR}})^2 + E(t)_{\text{XUV}} \hat{r} + V(r)_{\text{EFF}}. \quad (1.71)$$

Here we denote the vector potential of the streaking field as $A(t)_{\text{STR}}$.³³ The effective potential $V(r)_{\text{EFF}}$ describes the influence of the ion and the remaining electrons bound in the atom. If we replace the XUV pulses by electron pulses, the Hamiltonian has to be adapted since we have to consider the Coulomb attraction between electrons and nuclei, the repulsion between the electrons, their kinetic energies as well as the repulsion of the nuclei

$$\hat{H}(t) = \sum_i \left(\left(\frac{\hat{p}_i}{2} + A(t)_{\text{STR}} \right)^2 - \sum_n \frac{Z_n}{|\hat{q}_i - R_n|} \right) + \frac{1}{2} \sum_{\substack{i,j \\ i \neq j}} \frac{1}{\hat{q}_i - \hat{q}_j}. \quad (1.72)$$

Here Z_n gives the nuclear charge of the n^{th} nuclei, R_n the position of the n^{th} nuclei and \hat{q}_i the position of the \hat{q}_i electron. In both cases, it can be favourable to consider some simplifications to attempt to (numerically) solve the Schrödinger equations.

³³ In the Coulomb gauge: $E(t)_{\text{STR}} = -\partial_t A(t)_{\text{STR}}$

Further information can be found for example in [48]. We now only consider the case of an ionising XUV pulse and use the single active electron approximation. We additionally consider the following:

- **Field Free Ionisation:** Without the streaking field, the temporal profile of the photoelectrons is a replica of the XUV pulse. If the transition dipole matrix element d_p is known, the transition amplitude a_p to the continuum state $|p\rangle$ can be calculated and thus the XUV pulse be reconstructed [49]

$$a_p = \langle p | \Psi(t) \rangle = -i \int_{-\infty}^{\infty} d_p E_{\text{XUV}} \exp\left(i \left(\frac{p^2}{2} + I_p\right) t\right) dt. \quad (1.73)$$

Here the electric field of the XUV pulse is E_{XUV} , and I_p is the ionising potential of the nucleus.

- **Ionisation in Strong Fields:** If the ionisation now occurs with a temporal delay of τ with respect to the streaking field, the transition amplitude is given by

$$a_p = -i \int_{-\infty}^{\infty} d_{p(t)} E_{\text{XUV}}(t - \tau) \exp\left(i \left(I_p t - \int_t^{\infty} \frac{p(t')^2}{2} dt'\right)\right) dt. \quad (1.74)$$

The momentum of the free electron in the presence of the streaking field is given by $p = (p_0 + A(t_i)) - A(t)$. We assume that the influence of the nuclei after the ionisation can be neglected.

The square of the transition amplitudes yields the photoelectron spectrum depending on the temporal delay between XUV pulse and the streaking field

$$I(p, \tau) = |a_p(\tau)|^2. \quad (1.75)$$

This dependency enables us to investigate the temporal dynamics of photoexcitations or Auger decays by comparing the temporal shift of photoelectrons from different energy levels or between photoelectrons and Auger electrons.

1.6.3 Reconstruction of Pulse Characteristics

Reconstruction of pulse characteristics can be challenging, if no simplifying assumptions on the pulse envelope can be made. If we rearrange Equation (1.74), the following form can be achieved

$$a_p = -i \int_{-\infty}^{\infty} \exp(i\phi(t)_V) d_{p(t)} E_{\text{XUV}} \exp\left(i \left(\frac{p^2}{2} + I_p\right) t\right) dt, \quad (1.76)$$

with the Wolkow phase [50]

$$\phi(t)_V = - \int_{-t}^{\infty} pA(t') + \frac{A(t')^2}{2} dt. \quad (1.77)$$

By assuming a Gaussian envelope of the XUV pulse, a linear chirp, $U_p \ll W_{\text{kin}}$ as well as a linear polarisation of the streaking field we can simplify the Wolkow phase as the sum of three different constituents

$$\phi(t)_V = \frac{\sqrt{8WU_p(t)}}{\omega} \cos(\Theta) \cos(\omega t) - \frac{U_p(t)}{2\omega} \sin(2\omega t) - \int_t^{\infty} U_p(t) dt. \quad (1.78)$$

Here ω denotes the frequency of the streaking field and Θ the angle between the initial electron momentum and the polarisation of the streaking field. Only the first summand will contribute to the phase, if only electrons with an initial momentum parallel to the polarisation of the streaking field are taken into account and the assumption $U_p \ll W_{\text{kin}}$ is made. If we now insert this phase into Equation (1.76), we obtain the following representation of the streaked spectrum [47]

$$I(p, t) \sim \exp\left(-\frac{a(\omega - \omega_0)^2}{2(a^2 + (c \pm \frac{s}{2})^2)}\right), \quad (1.79)$$

with $a = \frac{1}{\sqrt{2}\tau_{\text{XUV}}}$. The linear chirp is given by c and the streaking speed is given as

$$s = \partial_t \Delta W = \pm \sqrt{8U_p(0)\omega_0\omega}. \quad (1.80)$$

These equations allow us to determine the width of the streaked spectrum to

$$\sigma_s = \sqrt{\sigma_{\text{XUV}} + \tau_{\text{XUV}}(s^2 \pm 4cs)} \quad (1.81)$$

Here σ_{XUV} indicates the spectral width in the field free case.

Through this relation, we established that the streaked spectrum is therefore a convolution of the XUV spectrum and the projection of the temporal structure of the pulse onto an energy modulation.

If the pulse is not chirped ($c = 0$), its duration can directly be given as

$$\tau_{\text{XUV}}^2 = \frac{\sigma_s^2 - \sigma_{\text{XUV}}}{s^2}. \quad (1.82)$$

To determine the pulse duration of a chirped pulse, it is necessary to measure the spectral width for two different delays between XUV and streaking pulse (σ_1 and σ_2). It is favourable to choose a delay where the streaking speed has the same amplitude but the opposing sign. By this, the chirp cancels from the equation and we arrive at

$$\tau_{\text{XUV}}^2 = \frac{\sigma_1^2 + \sigma_2^2 - 2\sigma_{\text{XUV}}}{2s^2}. \quad (1.83)$$

Another common practice is to use two detectors to determine the spectral width at the same time. By orientating the detectors at opposing positions in the interaction zone, the measured streaking speed is intrinsically of the same amplitude and of opposing sign.

Having provided the theoretical background of this thesis, we will now describe the experimental setup that is necessary for streaking Auger electrons of solid materials.

Chapter 2

Experimental Setup and its Characterisation

To streak Auger electrons generated by electron impact, several technical hurdles have to be overcome. The first is the operation of a photon-driven electron gun with electron pulses short enough to fulfil the streaking conditions for the Auger electrons (see Section 1.6). The second hurdle is the generation of strong near single-cycle THz pulses to streak the Auger electrons. Instead of generating those two different pulses from two different sources, it is common practice to start with one pulse and split it into two branches from which the UV and the THz pulses are then generated. Intrinsic to this approach, is also the feature of a minimal temporal jitter between both branches of the experiment.

To illustrate this approach, this Chapter firstly focuses on the generation of ultrashort NIR pulses in the main branch from which the two subsequent branches detour (see Section 2.1). In the following, we describe the setup for the UV branch in Section 2.2 and the THz branch in Section 2.3. Going more into detail, the photon-driven electron gun is discussed in Section 2.4.1. Afterwards the TOF spectrometer¹ is described in Section 2.4.2, which is responsible for the energy analysis. Finally the multiple-event time digitiser is discussed in Section 2.5, which is responsible for the data acquisition.

¹ **TOF:** Time-Of-Flight

2.1 Femtosecond Laser System

Base of the experimental setup of this thesis is a laser system², that consists of commercially available components (see Figure 2.1). It is used to generate ultrashort NIR pulses via a CPA setup³ with a Ti:Sapphire gain medium. Starting with < 10 fs broadband pulses originating from a passive mode-locked Ti:Sapphire oscillator, the pulses are temporally stretched by a factor of 1 000 – 10 000 to be amplifiable in a regenerative and multi-pass amplifier, before being recompressed to < 40 fs.

² Amplitude Technologies Pulsar

³ **CPA:** Chirped Pulse Amplification

To implement this concept, a Femtolasers Synergy Pro modelocked laser oscillator with a pulse duration < 10 fs, an output energy of 4.1 nJ, a central wavelength of 772 nm and a bandwidth of 90 nm at a repetition-rate of 75 MHz [51] is used. The pulses from the oscillator are then stretched within an aberration-free Öffner-triplet single-grating stretcher [52] to pulse durations of 10 ps – 100 ps.

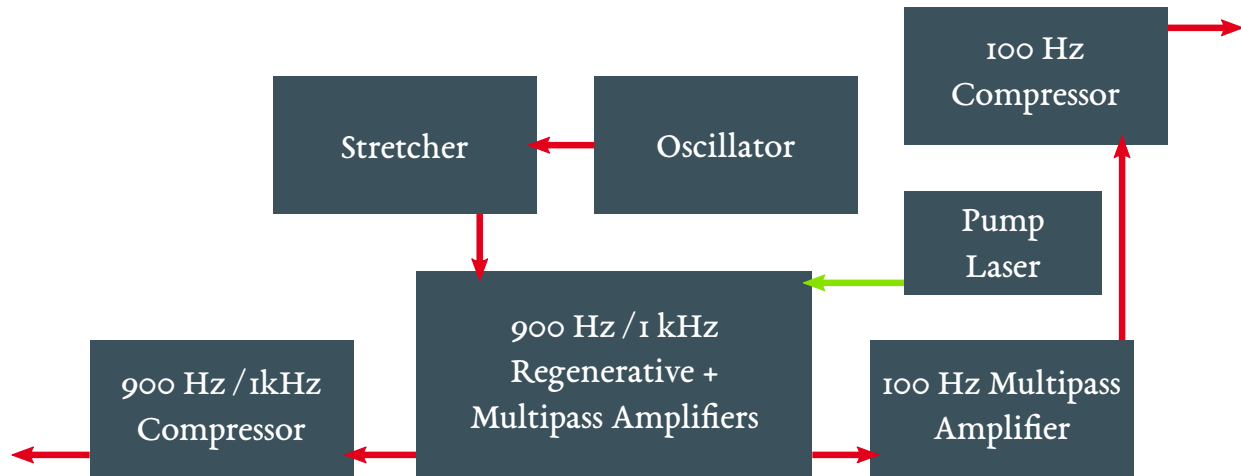


Figure 2.1: Schematic illustration of the used laser system. Positions and dimensions resemble the setup on site.

⁴ Photonics Industries DM30-527

⁵ Fastlite Mazzler

Since lower repetition-rates can deliver higher pulse energies, the repetition rate is reduced to 1 kHz by employing a combination of Pockels cells and polarisers, acting as a pulse picker.

In the first amplification stage, the pulse passes multiple times through a Ti:Sapphire crystal gain medium, which is pumped by a diode-pumped Nd:YLF-laser⁴ with a central wavelength of 527 nm. In this regenerative amplification process, the pulse energy is elevated to 0.8 mJ, while keeping a high quality beam profile. To suppress gain-narrowing and increase the possible amplification bandwidth, the cavity of the regenerative amplifier is equipped with an acousto-optic programmable gain control filter.⁵ By this measure, a bandwidth of 90 nm can be achieved.

Subsequent to the regenerative amplifier cavity, every tenth pulse of the kHz pulse train is picked by using a Pockels cell and is redirected, which results in two individual pulse trains with a repetition rate of 900 Hz and 100 Hz, respectively. The 100 Hz-branch is used for different experimental setups and will not be discussed further on.

In a second amplification stage, the 900 Hz pulses are amplified in a multi-pass amplification stage. In this stage, the pulses complete five cycles in a Ti:Sapphire crystal, which is pumped by the same laser as in the regenerative amplifier, but having undergone a frequency doubling.

In a final step, the linear chirp that was introduced in the beginning of the CPA setup, is removed by a grating compressor. The now compressed pulses feature a pulse energy of 3 mJ, a central wavelength of 800 nm with a spectral width of 30 nm and a pulse duration of 35 fs to 40 fs, while being p-polarised with respect to the horizontal plane. The beam size was determined to $w_x = (5.9 \pm 0.1)$ mm and $w_y = (7.1 \pm 0.1)$ mm with a divergence of $\Theta_x = 0.54$ mrad and $\Theta_y = 0.72$ mrad in previous works [13, 53]. After leaving the compressor, the beam travels 5 m in air while passing one periscope, four 45° dielectric mirrors, a second periscope and two additional 45°-mirrors until it reaches a beam splitter. Here the beam is divided in a ratio of 70/30, where 70% of the beam is reflected to the branch that is dedicated to the THz generation and the remaining 30% are transmitted to the branch responsible for the photon-driven gun.

Due to possible saturation effects in the readout electronics, the pulse energy of the branch dedicated to the photon-driven gun is of secondary interest. Therefore, the Mazzler is detuned to optimise the output of the THz branch. With a fully optimised THz fieldstrength (see Section 2.3), the overall pulse energy drops to 2.4 mJ, which results in pulse energies of the UV branch of 0.57 mJ and a pulse energy of the THz branch of 1.5 mJ.

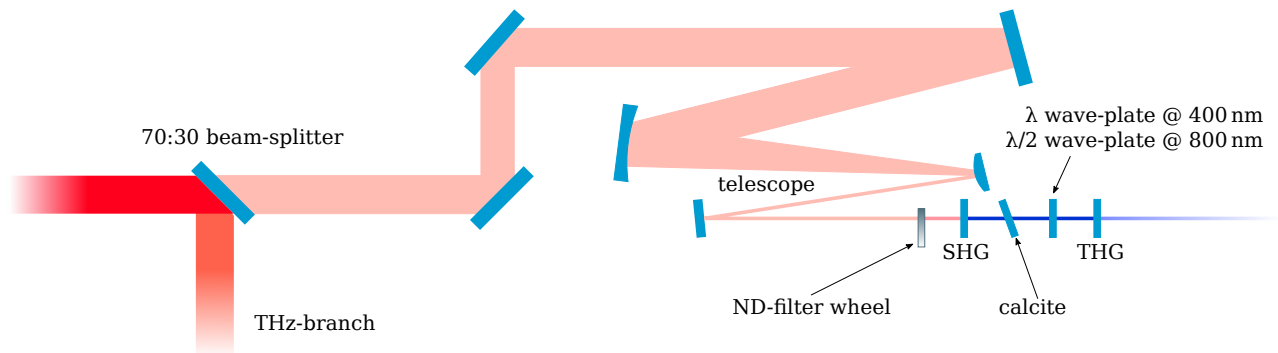


Figure 2.2: Simplified illustration of the THG source.

2.2 Second and Third Harmonic Generation

The design of the electron gun used in this thesis requires the back-illumination of a silver coated sapphire cathode. This imposes two conditions on the used radiation. The first being, that the wavelength has to be short enough to trigger the photoelectric effect. The second is a long enough wavelength, such that the radiation is still able to penetrate the silver layer of the cathode.⁶ Therefore, the choice was made towards a wavelength of 266 nm, which is the third harmonic of the 800 nm beam.

⁶ The photoelectric effect in silver is triggered by wavelengths shorter than 291 nm [54], while a transmission greater than 80% requires wavelengths in the range of 232 nm to 4435 nm [55].

There are several established procedures to generate the third harmonic of a given wavelength. A compact and highly efficient method is the generation via non-linear processes in crystals (see Section 1.2.1).

The used setup utilises a SHG with a subsequent SFG in two type-I BBO-crystals in a collinear configuration to generate 266 nm pulses. A simplified schematic of the setup can be seen in Figure 2.2.

After the beam splitter, the UV branch passes two 45°-mirrors and a periscope (not included in Figure 2.2) until it is back-reflected by a 0°-mirror onto a reflective telescope that reduces the beam diameter by a factor of 1:5. The telescope consists of a spherical-concave mirror⁷ with a radius of curvature of 1250 mm and a spherical-convex mirror⁸ with a radius of curvature of 250 mm. The telescope is followed by another 0°-mirror that reflects the beam through a 2 mm thick neutral-density filter wheel. The filter wheel is made of 2 mm thick UV fused silica coated with Inconel,⁹ allowing a continuously variable attenuation of the beam with an optical density between 0.04 and 4.0.

Since the attenuation is purely induced by reflection and thereby the optical density only depends negligibly on the degree of attenuation, no major changes in the pulse duration are to be expected. The pulse intensity of the UV branch after the telescope is high enough to drive the non-linear processes inside the crystals. Therefore no further focusing has to take place.

The now following setup for the actual third harmonic generation is build up by four components. In the first step, the second harmonic of the fundamental pulse is generated in a 0.2 mm thick type-I BBO-crystal¹⁰ with a cutting-angle of 29.2°. The mount of the crystal allows a rotation in the plane perpendicular to the beam propagation to align the polarisation of the fundamental beam and the optical axis of the crystal. In addition, the crystal can be tilted such that the incoming beam impinges exactly perpendicularly on the surface of the crystal. The newly generated SHG beam is s-polarised, while the copropagating fundamental beam is still p-polarised. Since the crystal for SFG is a type-I BBO as well, the polarisation of the beams has to be matched.

For this purpose a $\lambda/2$ -plate¹¹ for the 800 nm beam is introduced, which tilts the polarisation of the fundamental beam by 90° but leaves the polarisation of the 400 nm beam unaltered, as it acts as a λ -plate for it.

Since the group velocity of the 400 nm and 800 nm differ in BBO as well as in quartz, the pulses experience a temporal separation, while passing through both elements. To compensate for this effect and to guaranty an efficient third harmonic generation, a birefringent calcite plate¹² with a thickness of 1.7 mm is introduced as a third element. The plate is placed between the first BBO and the wave-plate, since here both beams still exhibit a different polarisation.

⁷ Laser Components, reflectivity at 800 nm > 99.8 %, AOI: 0°

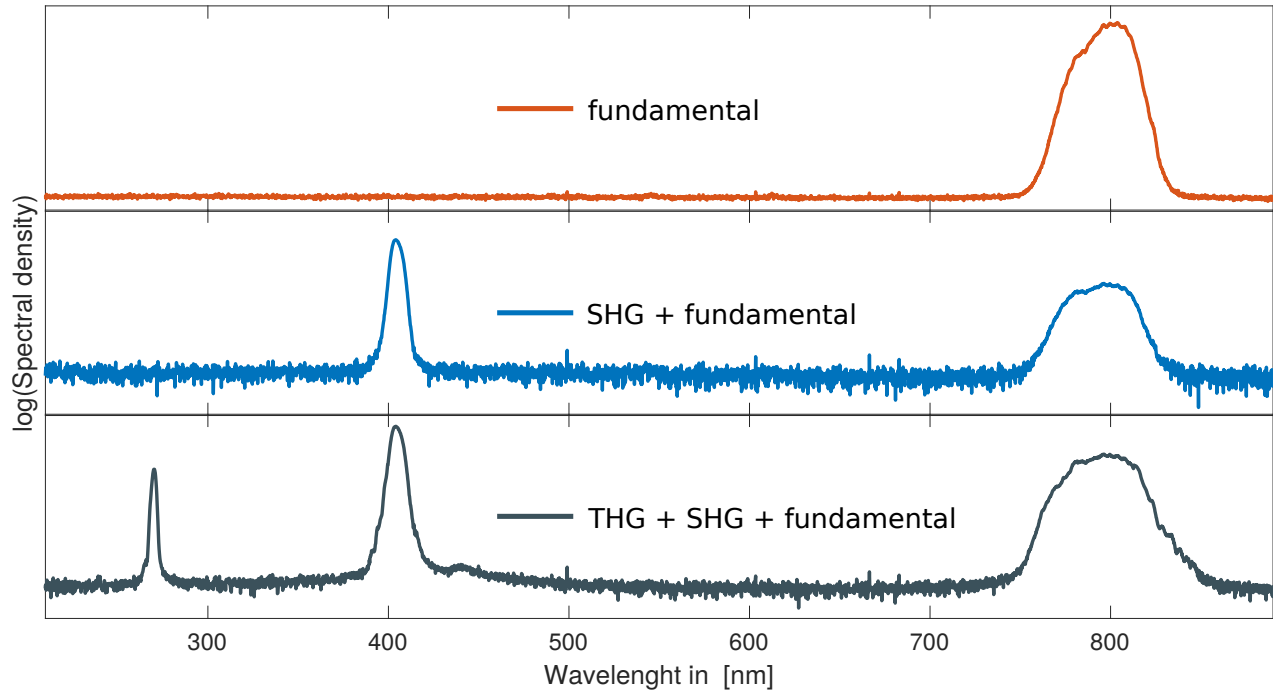
⁸ Layertec, reflectivity at 750-850 nm > 99.9 %, AOI: 0°

⁹ Thorlabs, NDC-100C-4M
Inconel: alloy from nickel, chrome and iron

¹⁰ EK SMA Optics, BBO-1002H

¹¹ EK SMA Optics, 465-4211
1.8 mm fused quartz

¹² EK SMA Optics, 225-2113



Inside the plate the refractive index of the extraordinary beam is lower than that of the ordinary beam. Therefore, the plate is orientated in such a way that the 400 nm beam is influenced by the extraordinary index of refraction and experiences a higher group velocity. The plate is mounted in a rotatable holder in such a way, that the tilt can be adjusted to compensate for the time difference between the two pulses.

As final element for the THG a second type-I BBO¹³ with a cutting-angle of 44.3° and a thickness of 0.1 mm is placed after the wave-plate.

Here the third harmonic of the 800 nm fundamental beam is generated via sum frequency generation of the 800 nm and 400 nm beam.

The efficiency of the SHG and the THG process were determined in [56] to be $\eta_{SHG} = (29 \pm 4) \%$ and $\eta_{THG} = (7 \pm 1) \%$, respectively.

In Figure 2.3, we can find the spectra generated in each step of the THG process. In the top part the fundamental spectrum with a central wavelength of $\lambda_0 = (798.5 \pm 0.15) \text{ nm}$ and a FWHM of $(35.4 \pm 0.4) \text{ nm}$ is shown. The middle sections illustrates the spectrum after the first BBO, where the fundamental beam copropagates with the newly generated second harmonic beam with a central wavelength of $\lambda_0 = (404.5 \pm 0.1) \text{ nm}$ and a FWHM of $(6.76 \pm 0.04) \text{ nm}$. The bottom part depicts the final output of the THG setup, where the third harmonic is produced in the second BBO with a central wavelength of $\lambda_0 = (270.1 \pm 0.1) \text{ nm}$ and a FWHM of $(2.55 \pm 0.02) \text{ nm}$.¹⁴

Figure 2.3: The spectra of each step of the THG process. The top graphic shows the spectrum of the **fundamental beam**, while the middle section depicts the stage after the first BBO, where the **second harmonic copropagates with the fundamental beam**. In the bottom frame the final output is shown.

¹³ EKSMA Optics, BBO-1009H

¹⁴ A Fourier-limited pulse with $\lambda = 270.1 \text{ nm}$ and $\Delta\lambda = 2.55 \text{ nm}$ would exhibit a FWHM pulse duration of $\tau = 42.1 \text{ fs}$.

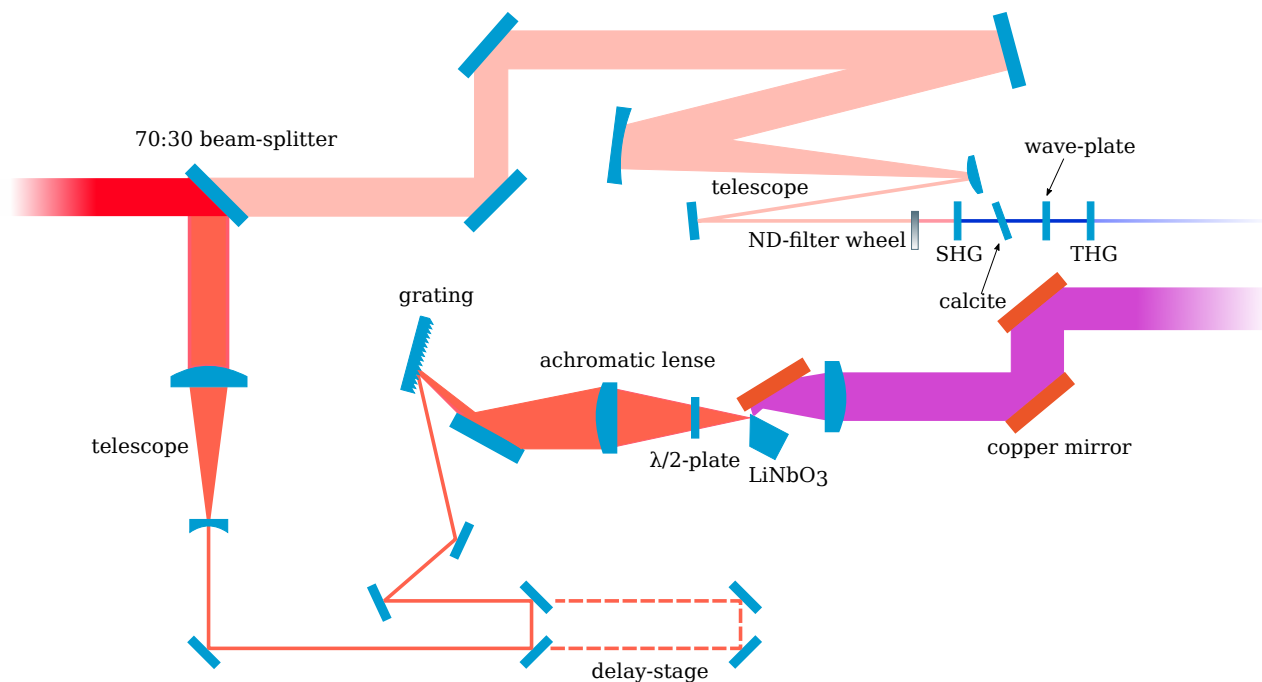


Figure 2.4: Simplified illustration of the THz and UV source. The **NIR pulses** are split in a 70:30 ratio at the beam splitter. The majority of the pulse energy is used to generate **THz pulses**, while the remaining energy is used to generate **UV pulses**.

The reason why the central wavelength of the second and third harmonic differ from the expected values of 399.25 nm and 266.17 nm are due to the fact, that the BBO-crystals were detuned to reduce the excess energy of the photoelectrons, which results in faster electron pulses inside the gun (see Section 2.4.1).

2.3 THz Radiation Source

The second hurdle on the way to streak Auger electrons produced by electron impact is the generation of strong near single-cycle THz pulses.

As a first step in the THz generation, the 800 nm beam passes through a transmissive telescope consisting of a plano-convex lens with a focal length of $f = 250$ mm and a plano-concave lens with a focal length of $f = -100$ mm to reduce the beam diameter from ~ 10.5 mm by a factor of 2.5 to a diameter of ~ 4.2 mm (see Figure 2.4). After passing a 45° -mirror and a periscope, the beam passes through a delay-stage. Here a defined delay between THz and UV branch can be introduced, which is necessary for conducting the streaking experiment. The unit is built up by two 45° -mirrors that are orientated perpendicular to each other and are mounted on a linear stage that is equipped with a stepper motor, capable of providing optical delays of (33.3 ± 4.5) fs/step. After passing two additional mirrors, the beam is reflected by a blazed grating with 2000 lines/mm, which is diverging by 9.5° from the Littrow configuration to provide the optimal pulse front tilt for an effective phase matching inside the LiNbO₃-crystal (see Section 1.3.5).

For a parasitic monitoring of the beam alignment, the 0th order of

refraction of the grating is reflected onto a screen via a mirror, while parts that are transmitted by the mirror are monitored by a CCD-camera to check the angular alignment (both not shown in Figure 2.4). While the 0th order is used for monitoring, the 1st order is used for the THz generation. The 1st order is reflected into an achromatic lens with a focal length of 75 mm to image the grating onto the crystal. In between lens and crystal, a $\lambda/2$ -plate is mounted to change the polarisation of the beam from p-polarisation to s-polarisation. The beam diameter is demagnified by the lens by a factor of two to ~ 2 mm. For an optimal in-coupling of the beam, the crystal is equipped with an anti-reflex coating for 800 nm. The THz output can also be increased by applying few layers of polyimide tape to optimise phase matching conditions on the backside of the crystal.

The angle between entrance- and exit-face of the crystal is cut with an 63° angle to enable a perpendicular exit of the THz pulses. Since the THz beam exhibits a large divergence after exiting the LiNbO₃-crystal, a copper mirror is placed directly after the crystal to reflect the beam into a plano-convex Zeonex-lens with a focal length of 100 mm.

Instead of realising a collimated beam, the setup uses an intermediate focus halfway to the interaction point in the experimental chamber to reduce clipping of the beam during transport. To gain full control of the THz output, the crystal is mounted to a holder that is capable of tilting, rotating and shifting the crystal. To monitor the generated output, a copper parabola can be placed after the Zeonex-lens to focus the THz beam onto a pyroelectric detector to measure the pulse energy. The detector was calibrated in an earlier work [57], has a size of $2 \text{ mm} \times 2 \text{ mm}$ and indicates pulse energies of up to $1.4 \mu\text{J}$ per pulse. The pyroelectric detector can be removed and the THz Beam can be coupled into an electro-optical sampling setup to make statements on the temporal profile of the THz pulses.

If the copper parabola is not placed into the beam path to monitor the THz pulses, the beam is reflected by two copper mirrors at an angle of 45° (see Figure 2.4) and then enters the experimental chamber through a polymer window.

2.3.1 Electro-Optical Sampling

If the pyro-electric detector is replaced by a ZnTe-crystal, the THz beam can be characterised via an electro-optical sampling setup (for a theoretical background, see Section 1.3.6, a schematic illustration of the setup can be found in Figure 2.5). It is common practice to perform the EOS inside the experimental chamber at the interaction point to establish the temporal overlap of THz pulse and whichever type of pulses used in a given experiment.

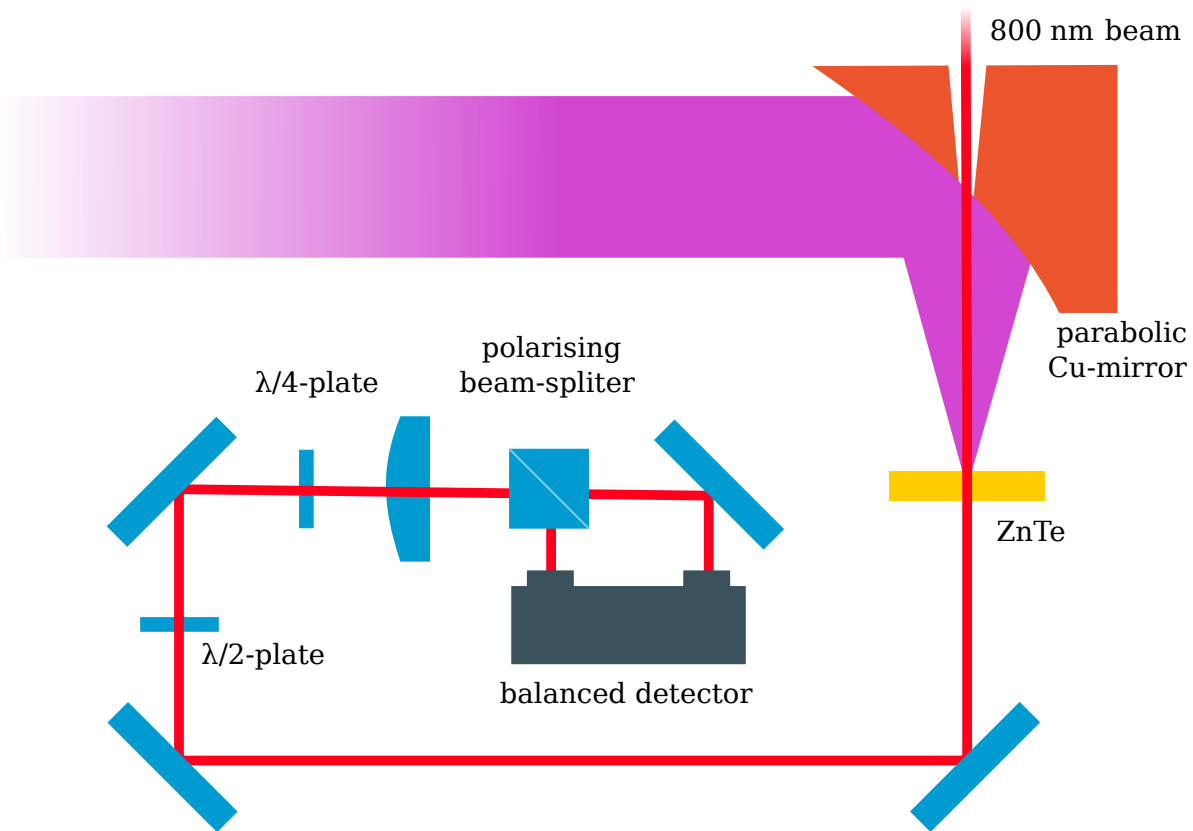
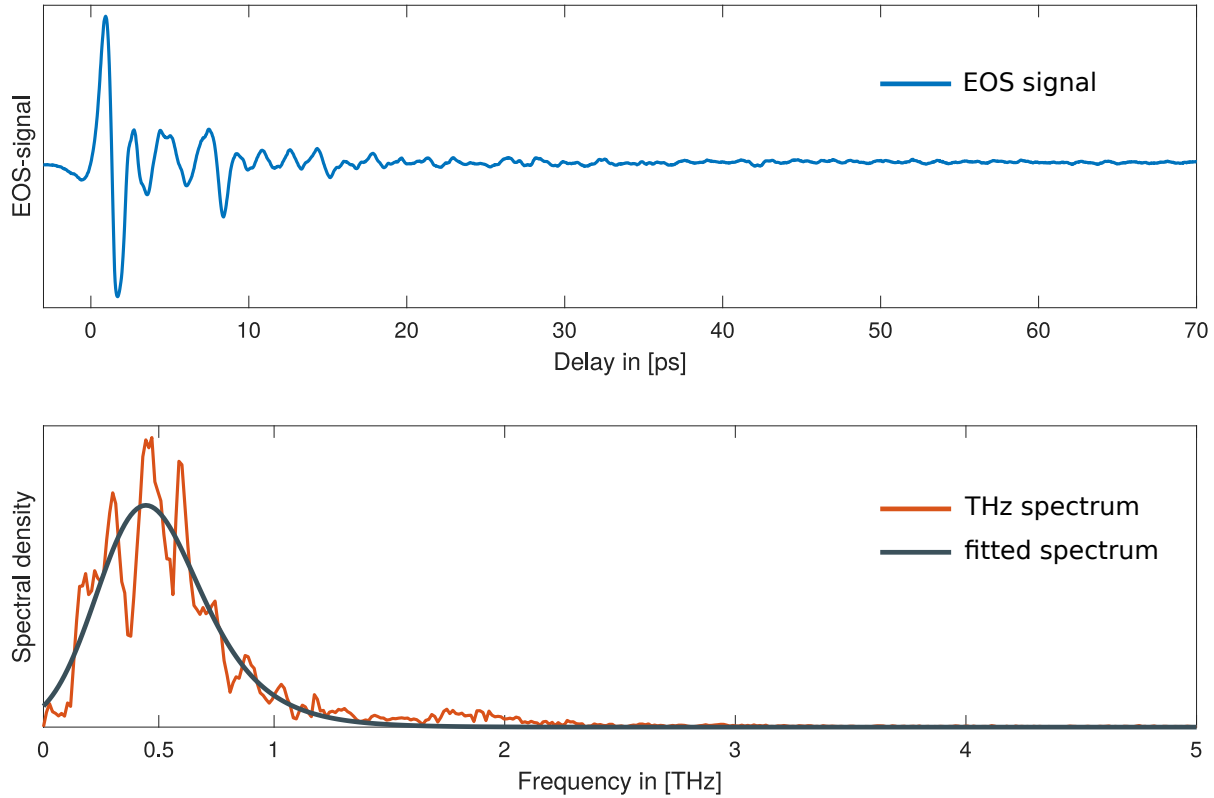


Figure 2.5: Simplified illustration of the used EOS setup. Here the **NIR pulses** are spatio-temporally overlapped inside the **ZnTe-crystal** with the **THz pulses**.

However, the geometry of the setup used in this thesis does not allow such an arrangement, thus the EOS is solely used to characterise the temporal profile of the THz pulses.

In the used setup, the 800 nm beam is utilised to probe the electro-optical effect induced by the THz pulses in the ZnTe-crystal. After being focused into the crystal, the THz beam diverges and can be neglected in the following. The 800 nm beam passes several 45° -mirrors before it is transmitted through a $\lambda/2$ -plate and a $\lambda/4$ -plate (see Figure 2.5). Those wave-plates are responsible for generating two equal contributions to a s-polarisation and p-polarisation component of the beam, which is then separated by a polarising beam splitter that passes the two partial beams to the two photodiodes of a balanced detector.

To guarantee a complete illumination of both photodiodes, the 800 nm beam is focused before the beam splitter. The results of a representative EOS measurement can be found in Figure 2.6. The measurement samples a temporal delay of 75 ps and reveals an almost single-cycle THz pulse with a center of mass of the frequency of $\nu_{\text{exp.}} = (0.56 \pm 0.3) \text{ THz}$ for the raw data and a center of mass of the frequency of $\nu_{\text{fit}} = (0.502 \pm 0.02) \text{ THz}$ for the fitted data.



If a Gaussian envelope is fitted to the EOS signal, we obtain a duration of $\tau = (2.8 \pm 0.1)$ ps. Those results are in good agreement with the frequencies¹⁵ found in [57], where the same setup with a lower pulse energy for the THz pulses was used.

So far all the components of the described laser system were operated at atmospheric pressure. We will now shift the focus towards the experimental chamber, capable of providing pressures of down to $\sim 7 \times 10^{-7}$ mBar. Here the photon-driven electron gun is operated, providing the high energetic electron pulses for the experiment. These pulses are then used to generate Auger electrons that are streaked with the strong near single-cycle THz pulses.

2.4 Experimental Chamber

As depicted in Figure 2.7, the THz beam enters the chamber through a 3 mm polymer-window with an aperture of 40 mm and 90 % transmission [57].

Inside the chamber, the THz beam is reflected by two copper mirrors in a periscope arrangement, which lifts the beam to the level of the electron gun and TOF spectrometer. The periscope reflects the beam by 90° with respect to the preceding beam trajectory and changes the polarisation from s-polarised to p-polarised.

Figure 2.6: The **electro-optical sampling** of the generated THz pulses reveals near single-cycle THz pulses. A **spectral analysis** of the EOS signal highlights prominent absorption dips due to atmospheric water.

¹⁵ $\nu = 0.66$ THz

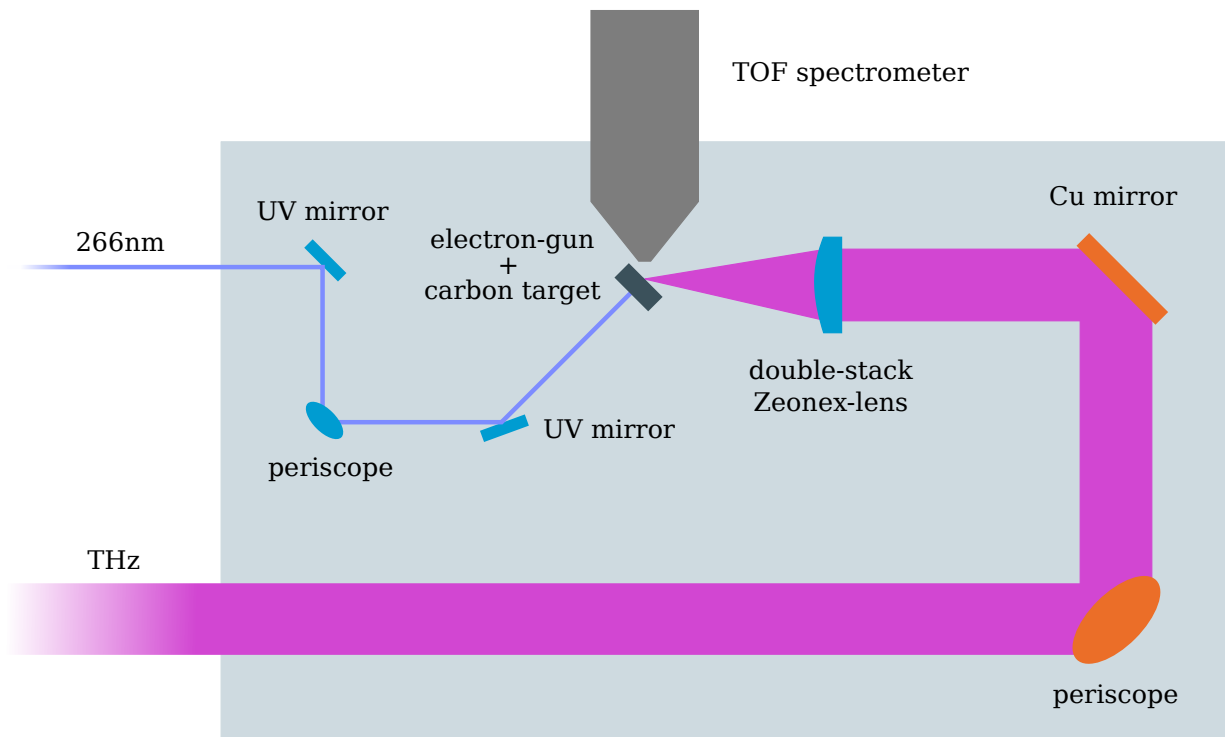


Figure 2.7: Schematic illustration of the experimental chamber.

After the periscope, the beam is again reflected by a copper mirror by 90° , whereafter it will be focused by a double Zeonex-lens array with an effective focal length of ~ 35 mm onto the carbon target. Said target can be replaced by a pyroelectric detector to monitor the THz output and the spatial overlap in the interaction zone.

To couple the 266 nm beam into the chamber, a 1 mm thick anti-reflex coated sapphire window with an aperture of 40 mm is used. Inside the chamber, the beam is reflected by a dielectric mirror¹⁶ by 90° . Thereafter, the beam enters two dielectric mirrors in a periscope arrangement, where the beam is lifted to the level of the electron gun and the TOF spectrometer.

By this, the polarisation changes from p-polarised to s-polarised, but since the polarisation is lost during the electron generation, no countermeasures were taken. After the periscope, the beam passes a last dielectric mirror that reflects the beam by a 135° -angle into the electron gun. Between the periscope and the last 135° -mirror, a movable fluorescent screen can be inserted to monitor the UV beam alignment. Precise alignment is performed by maximising the TOF signal.

¹⁶ Laser Components, reflectivity at 266 nm $> 99.3\%$ and $< 10\%$ for 400 nm and 800 nm

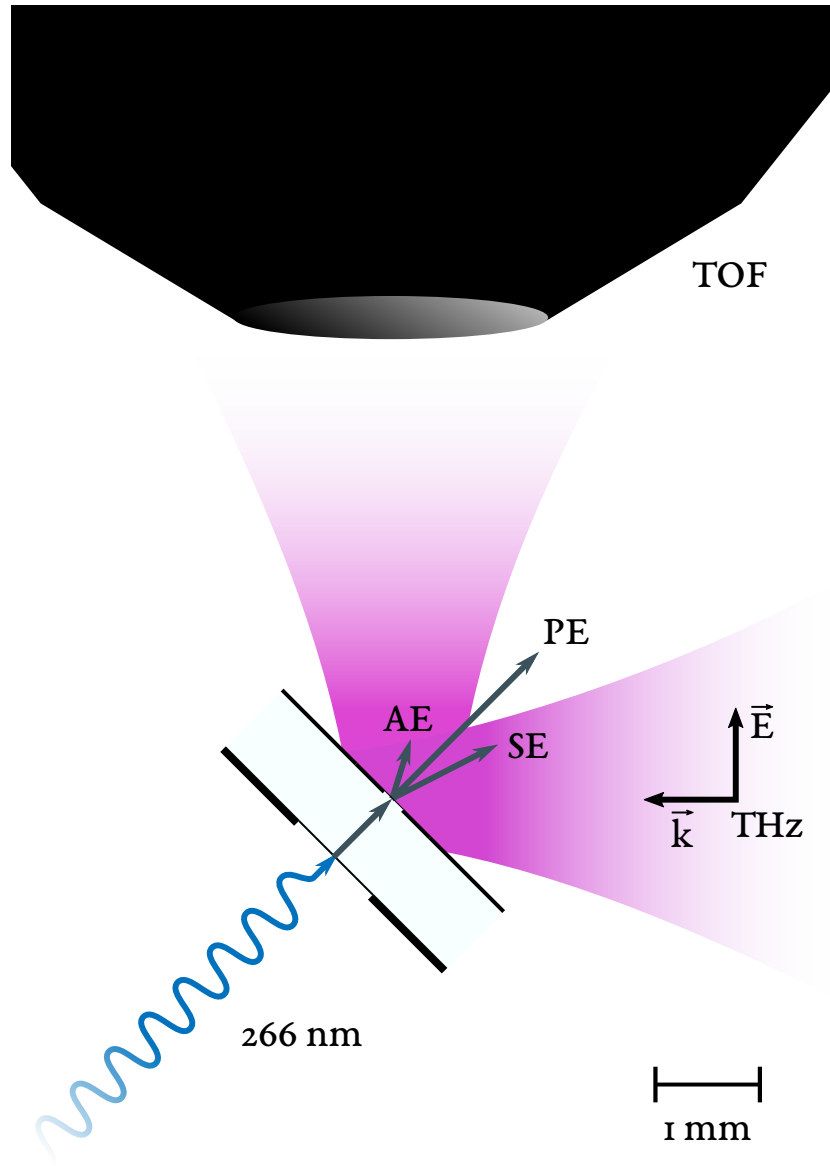


Figure 2.8: In this detailed schematic of the interaction zone, we can see that the majority of the primary electrons (PE) will miss the TOF due to the tilted orientation of the gun ($\angle \vec{k}_{UV} \vec{k}_{THz} = 40^\circ$). By this, the signal inside the TOF can be reduced to avoid saturation in the readout-electronics. Furthermore the ratio of the isotropic scattered secondary electrons (SE) and Auger electrons (AE) to the anisotropic scattered primary electrons will increase. Only the cathode and anode of the gun are shown. Dimensions (except thicknesses) to scale.

With the setup described so far, we are now able to shift the focus to the interaction zone, where the 266 nm pulses generate high energy electron pulses¹⁷ with a temporal profile in the fs regime, which again produces Auger electrons that can be streaked with the strong near single-cycle THz pulses. As shown in Figure 2.8, the electron beam and the flight axis of the TOF includes an angle of 40° . The same applies for the angle between THz and electron beam. This arrangement serves two purposes, the first being the suppression of the primary electrons inside the TOF.

¹⁷ The setup is able to produce bunch energies of up to 5 keV, but theoretical energies of up to 7.5 keV would be possible before the vacuum breakdown is reached.

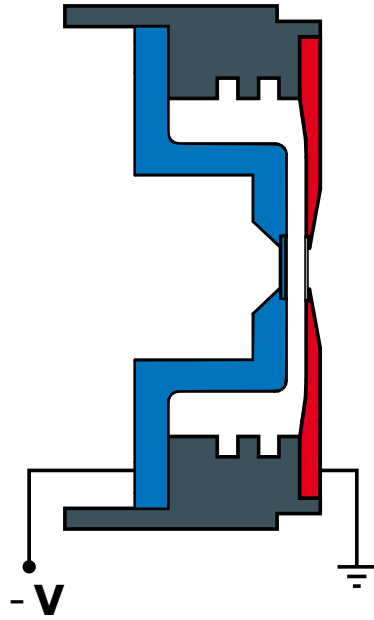


Figure 2.9: Simplified diagram of the utilised electron gun. The **cathode** is separated from the **anode** by a PEEK insulator, forming a gap of 0.75 mm between the cathode and the anode. The grooves in the insulator were implemented to reduce surface currents. The outer diameter of the gun is 25.4 mm and therefore allows mounting in standard optical mounts.

¹⁸ **TEM:** Transmission Electron Microscopy

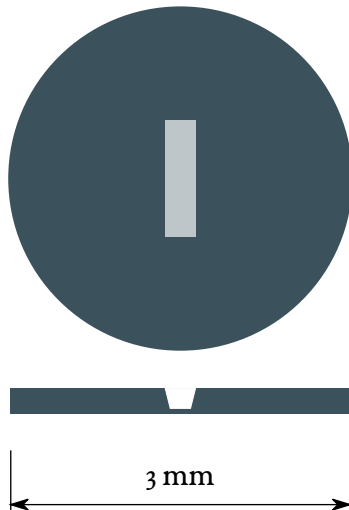


Figure 2.10: Illustration of the TEM window. The frame (dark gray) has a diameter of 3 mm and a thickness of 0.2 mm. The pane (light gray) has a height of 1 mm, a width of 0.25 mm and a thickness of 40 nm.

Too many electrons would lead to saturation effects in the readout electronics or other undesired effects inside the flight-tube itself. Since the primary electrons only experience minimal scattering, the majority miss the TOF with the chosen geometry of the experiment. The second reason is the streaking process. In common setups, the THz beam is copropagation with the pump beam into the interaction zone. Here the THz field is polarised in such a way that it accelerates or decelerates the photo- or Auger electrons towards the detector. In this setup, the target is a conducting solid. Therefore, the surface of the sample has to be tilted by a given angle Θ to assure the streaking of the Auger electrons. If the sample surface would be orientated perpendicular to the symmetry axis of the spectrometer, only a grazing THz field on the sample would be possible. By tilting the sample, the THz field is reduced by a factor of $\sin(\Theta)$ but the full focus can illuminate the surface.

2.4.1 Electron Gun

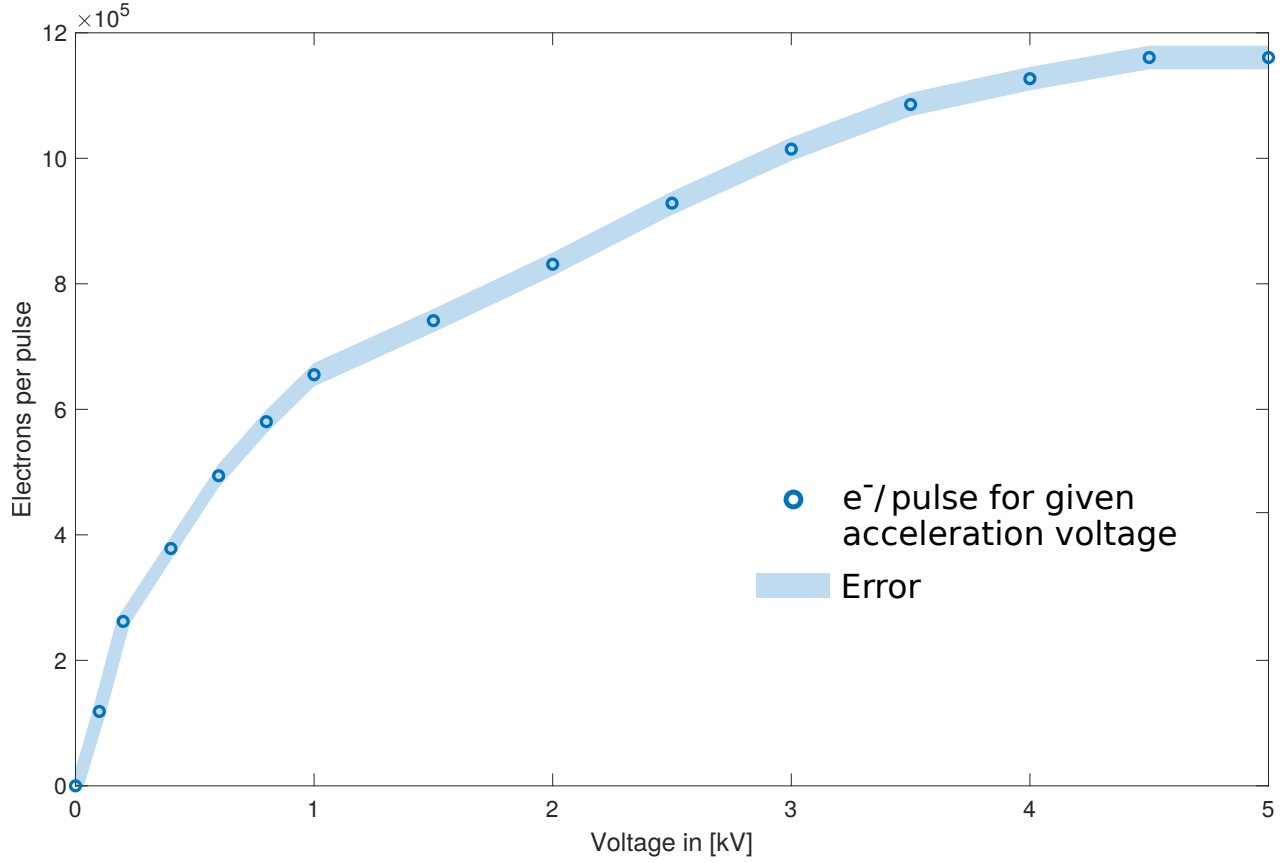
To generate electron pulses with a temporal profile in the femtosecond regime and negligible jitter with respect to the THz pulses, a photon-driven gun is utilised (see Figure 2.9). The electron pulses are generated by illuminating the backside of a 200 μm thick sapphire cathode, which is coated with a 40 nm silver layer, with UV pulses. With a photon energy of $4.59 \pm 0.03\text{eV}$, the UV pulses will generate electrons with a kinetic energy of $0\text{ eV} - 0.33\text{ eV}$, if a work function of silver of $\phi_{\text{Ag}} = 4.26\text{ eV} - 4.74\text{ eV}$ [54] is assumed.

It may be advantageous to reduce the difference between photon energy and work function to optimise the pulse duration inside the electron gun (see Equation (2.3) and [58]). The electron pulses generated in this fashion are then accelerated over a distance of 0.75 mm by a negative voltage applied to the cathode towards the grounded anode. Said anode consists of a 1 mm thick aluminium plate with an insert for a 200 μm thick Si_3N_4 TEM window frame.¹⁸ The pane size is $1\text{ mm} \times 0.25\text{ mm}$ with a thickness of 20 nm (see Figure 2.10). The short edge of the window is orientated parallel to the polarisation of the THz field to minimise temporal broadening of the signal (see Section 3.2.1).

The side of the TEM window which is facing the TOF is sputter coated with a 40 nm thick layer of carbon and serves as target in which the Auger electrons are generated (see Figure 2.8).

The UV pulses generated in the THG setup (see Section 2.2) exhibit an estimated pulse duration of $(55 \pm 6)\text{ fs}$ [13]. Due to multiple effects during the acceleration process, the final pulse duration of the electron pulses is longer. The final pulse duration is given by

$$\tau_e = \sqrt{\tau_{\text{Laser}}^2 + \tau_{\text{Acc}}^2 + \tau_{\text{SpChrg}}^2} \quad (2.1)$$



where τ_{Laser} denotes the pulse duration of the UV pulses, τ_{Acc} the temporal broadening due to the acceleration process and τ_{SpChrg} the broadening due to space charge effects.

Assuming a Fourier-limited pulse with an energy bandwidth of ΔE , τ_{Laser} is given by

$$\tau_{\text{Laser}} \approx 0.44 \frac{2\pi\hbar}{\Delta E}, \quad (2.2)$$

assuming a Gaussian profile. The temporal broadening induced by accelerating the electron pulses inside the gun is given by [58]

$$\tau_{\text{Acc}} \approx \frac{\sqrt{\sqrt{2}m_e\Delta E}}{eV_{\text{Acc}}}, \quad (2.3)$$

where V_{Acc} denotes the accelerating voltage.

So far, the temporal broadening only takes single electron pulses into account. But if a pulse consists of multiple electrons, space charge effects can play a role in the broadening process.

Figure 2.11: Characteristic function of the used electron gun, measured at an approximated UV flux of $2.71/\text{cm}^2$. The generated electrons were measured directly after the anode with a Faraday cup to maximise the electron yield.

For an electron pulse composed of N electrons, which is accelerated over a length L with an initial beam-radius r_B , the temporal broadening is given by [59]

$$\tau_{\text{SpChrg}} = \sqrt{\frac{q_e m_e}{2V_{\text{Acc}}^3} \frac{L^2 N}{\epsilon_0 4\pi r_B^2}}. \quad (2.4)$$

To estimate, if the temporal broadening generated by space-charge has to be taken into account, the number of electrons per pulse were measured with a Faraday cup (see Figure 2.11). For this purpose, the current between the gun and the cup is measured for different acceleration voltages.

The final streaking experiment is performed at an acceleration voltage of 3 kV, which yields approximately 10^6 electrons per pulse, if the output is maximised. Since the flux is reduced during the final experiment, this can be considered as an upper limit.

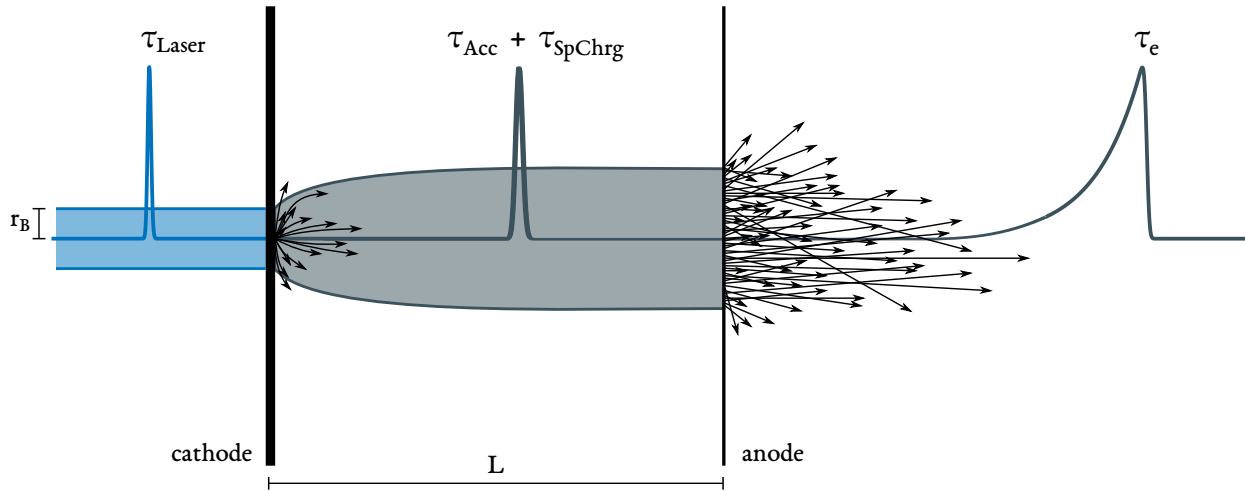


Figure 2.12: Schematic of the broadening of electron pulses inside the electron gun. The UV pulse generates an electron pulse inside the gun (black arrows) which will be broadened due to the acceleration and space charge effects.

With a drift distance of $L = 0.75$ mm and an initial beam radius of $r_B = 0.5$ mm, the temporal broadening due to space charge effects is estimated to be $\tau_{\text{SpChrg}} = (8.3 \pm 0.3)$ fs. Combined with a temporal broadening due to the acceleration of approximately $\tau_{\text{Acc}} = (99.8 \pm 0.7)$ fs and $\tau_{\text{Laser}} = (55 \pm 6)$ fs, the electron beam will exhibit an estimated temporal profile of $\tau_e = (114.3 \pm 6.1)$ fs when it enters the anode (see Figure 2.12).

As a final factor, the temporal broadening inside the anode material has to be taken into account. As depicted in Section 1.4.4, this is no trivial task since electron-electron collisions have to be taken into account, which are interactions of quantum-mechanically indistinguishable particles. A rough estimate can be given by starting from the

energy spread of the primary electrons measured by the TOF spectrometer, if they pass through the anode material.

For this, spectra were measured with a copper mesh as anode and compared to spectra measured with the Si_3N_4 anode. For a 3 keV beam, the energy of the inelastically scattered primary electrons is broadened by approximately 13% during the transition through the anode material. The energy spread can be translated to a velocity spread, which again can be translated to temporal spread of roughly 0.25 fs inside the anode material (see Figure 2.13). Compared to the contributions of other effects, this temporal broadening inside the anode material is negligible.

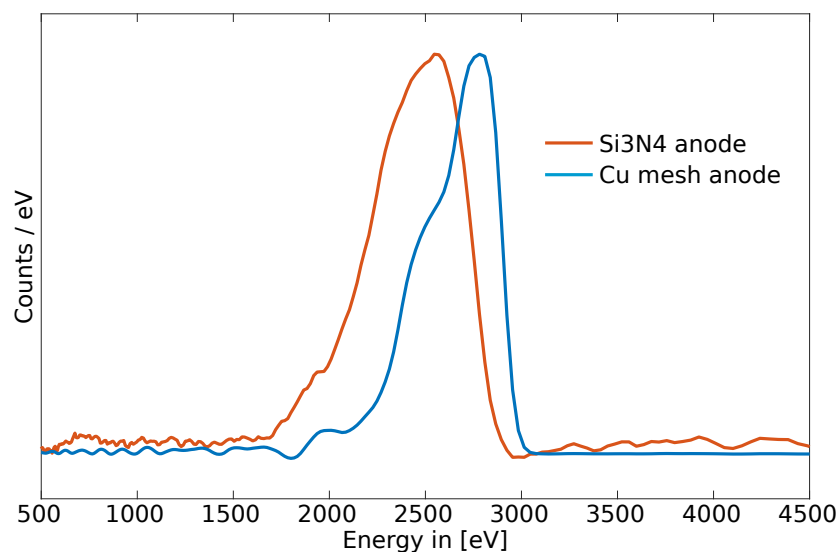


Figure 2.13: Spectra measured with a Si_3N_4 and a copper mesh anode to estimate the temporal broadening inside the anode material.

The electron pulses that now pass the anode material and the carbon target consist of elastically scattered primary electrons, inelastically scattered electrons, secondary electrons and Auger electrons [60]. Those electrons will be detected by the time-of-flight spectrometer, which is orientated at a 40° -angle towards the Si_3N_4 -window (see Figure 2.8).

2.4.2 Time-Of-Flight Spectrometer

To detect the broad energy spectrum of the electron pulses leaving the gun, a time-of-flight spectrometer is used. It maps the time an electron needs to pass a given distance to a kinetic energy.

The TOF detector used in this setup consists of six electrostatic lenses to collect the electrons, a flight tube with a length of 445 mm, which can also be used to retard the flight time of the electrons and a copper mesh that will accelerate the electrons to a double-stack MCP¹⁹ (see Figure 2.14).

¹⁹ MCP: Multi Channel Plate

The signal of the MCP will be amplified and processed by a multiple-event time digitiser²⁰ (see Section 2.5). The transmission of the spectrometer depends on the kinetic energy and angle of incidence at which the electrons enter the spectrometer. Since this thesis investigates carbon Auger electrons, the energy range of ~ 270 eV is of particular interest. For an angle of incidence smaller than $\pm 5^\circ$ with respect to the central axis of the flight tube the transmission is greater than 50 %.

²⁰ MCS6A, FAST ComTec

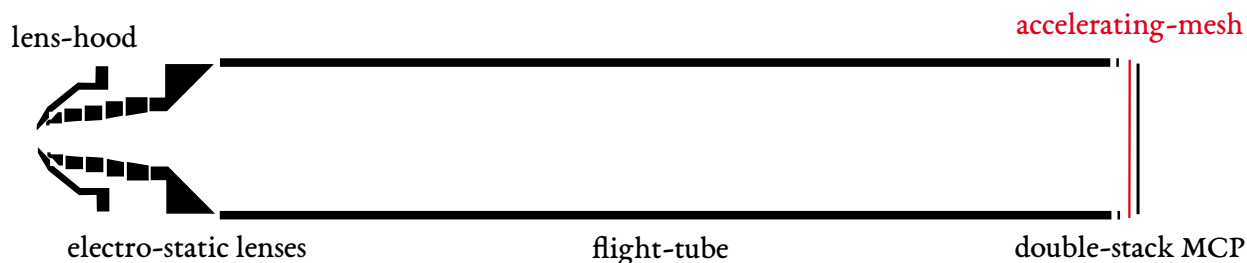


Figure 2.14: Schematic of the used 445 mm time-of-flight spectrometer with six electrostatic lenses and a double-stack MCP.

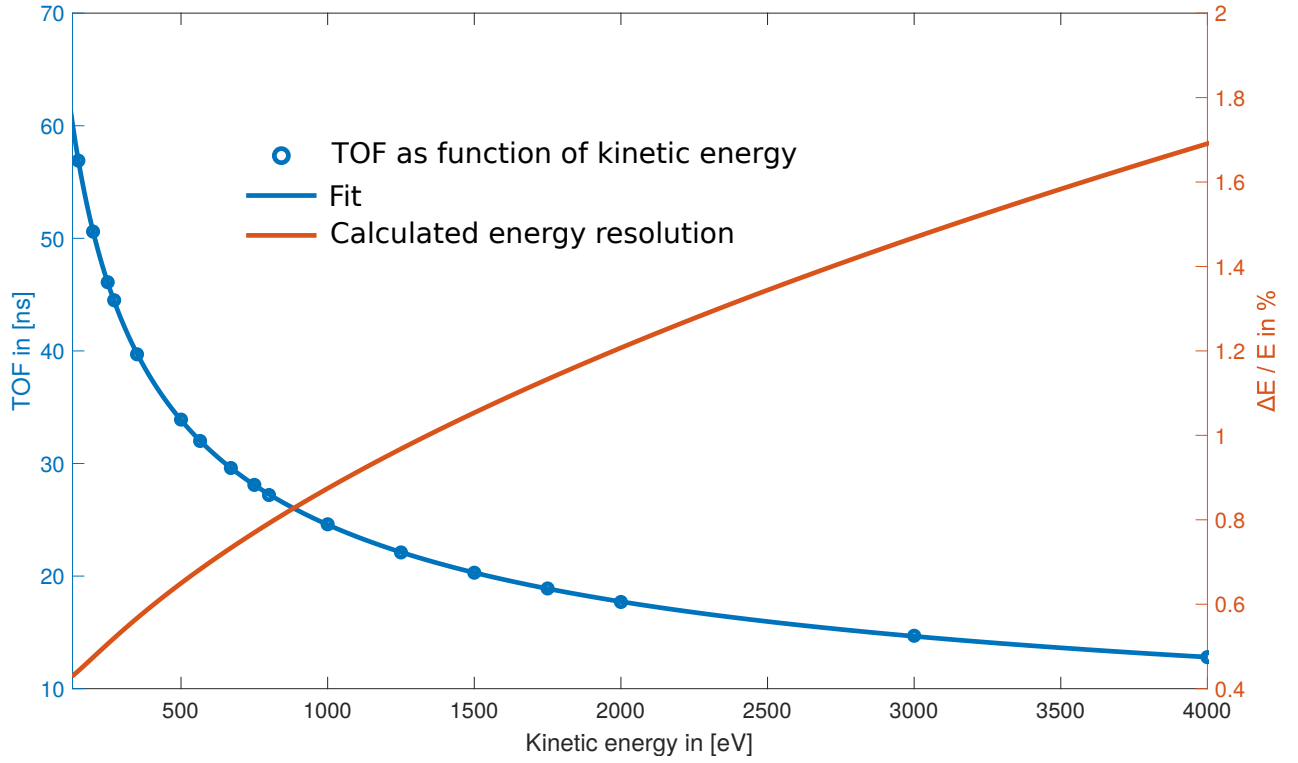
Due to the isotropic distribution of the Auger electrons, the aperture size and its distance to the sample, electrons within an opening-angle of $\pm 11^\circ$ are registered, which reduces the transmission to 3 %.

The TOF was drafted in a previous work [61] and was designed to reach the best resolution for electrons with a kinetic energy in the region of 10 – 30 eV. By applying a retardation voltage, it is possible to shift this region towards higher energies. For the Auger electrons of carbon with an energy of 272 eV, this would imply a retardation of ~ 240 V. In practice, it was only possible to apply voltages of up to ~ 120 V before additional electrons were generated inside the TOF spectrometer and the signal was corrupted. Therefore, the decision was made to work with a set of minimal lens voltages, that were established in [62], to guarantee a low but broad and flat transmission curve.

To map the flight time to a kinetic energy, it is common practice to match the flight time to known spectral lines of different elements (e. g. Xenon or Krypton) to calibrate the spectrometer. Due to the design of the setup, this approach is not possible.²¹ Instead, the Si_3N_4 -window was replaced with a copper mesh and the acceleration voltage of the gun was varied in the range of 150 V to 4000 V to map a wide range of kinetic energies to a given time-of-flight. The replacement of the Si_3N_4 -window was made to allow for a higher transmission in the low-energy regime.

In this calibration the time-of-flight is defined in such a way, that the arrival time corresponds to the maximum derivative of the leading edge of the signal. The resulting calibration curve can be found in Figure 2.15.

²¹ A calibration via a gas target would require a focussed UV or XUV beam and a gas inlet in the interaction zone, which is not possible due to space limitations inside the chamber.



The correlation between kinetic energy and the time-of-flight can be parametrised by

$$W = \frac{m_e L^2}{2(t - t_0)^2} - eU. \quad (2.5)$$

Here L is the effective distance the electrons travel inside the tube, t_0 the point in time where the electrons left the interaction zone with respect to a chosen time-zero and U gives an effective retardation voltage. Since the correlation is non-linear, the conservation of the number of electrons has to be considered.

By demanding

$$N dt = N' dW = N' \frac{\partial W}{\partial t} dt, \quad (2.6)$$

we obtain the adjusted counts N' of electrons per energy interval dE through the relation

$$N' = \frac{1}{2} \frac{m_e L}{(E + eU)^{3/2}} N. \quad (2.7)$$

To optimise the TOF signal, the flight tube is mounted to the chamber via four threaded bars. By turning the mounting-screws, the TOF nozzle can be moved towards or away from the interaction zone. In addition, the flight tube can also be tilted vertically, horizontally, or in a combination of both.

Figure 2.15: The calibration of the TOF spectrometer results in an effective voltage of $U = (80 \pm 10)$ V and an effective length of $L = (483 \pm 3)$ mm. The errors of the measured data is in the range of $\mathcal{O}(100)$ ps and are omitted in the Figure to increase visibility. The calculated energy resolution of the spectrometer shows the typical decrease in energy resolution for higher kinetic energies of TOF spectrometers.

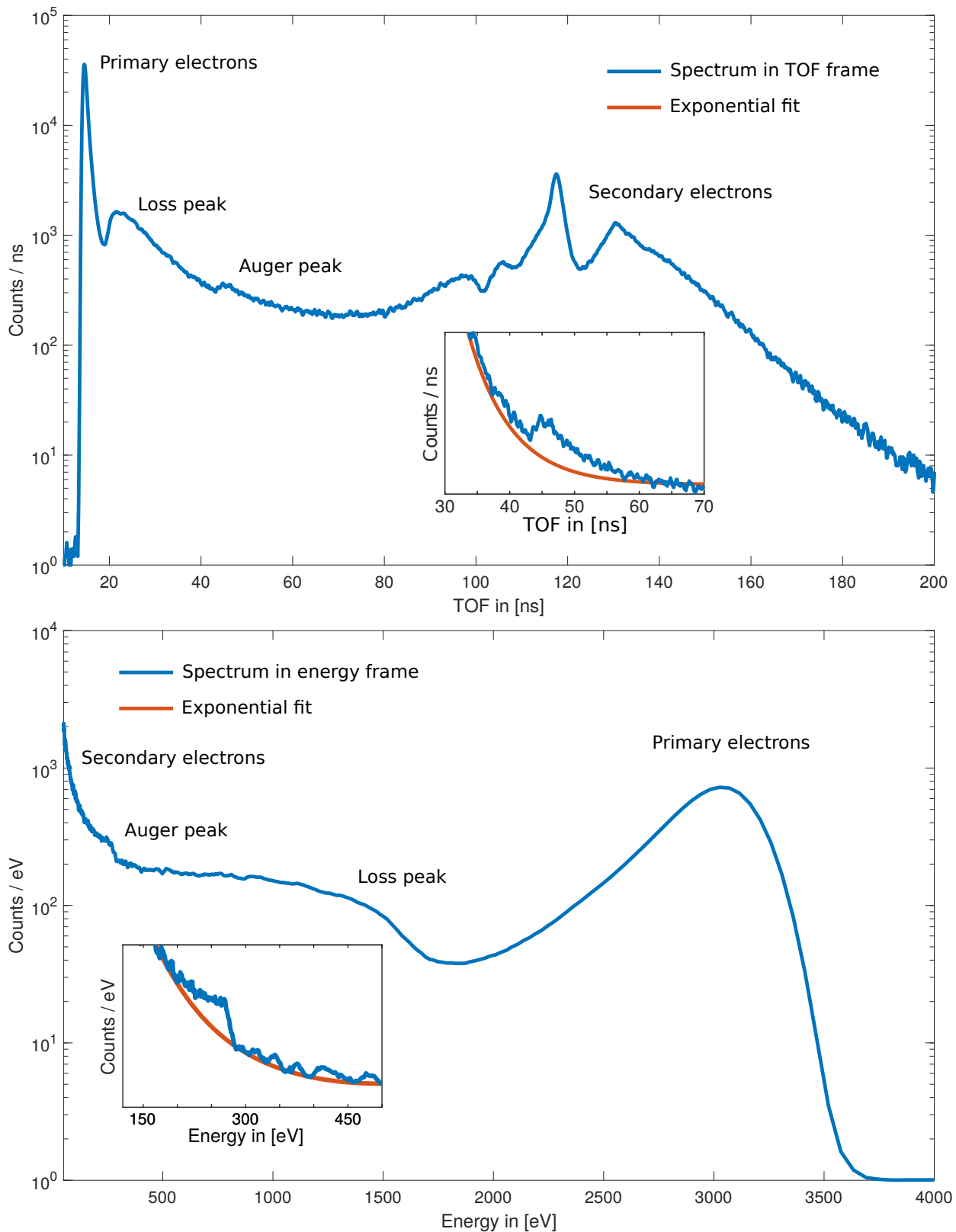


Figure 2.16: Complete spectrum of carbon, generated by 3 keV electron impact. Spectra shown in the TOF- (top) and energy-frame (bottom). The insets show the assumed **exponential background** of the Auger electrons. The visible substructure of the spectrum shown in the inset for the energy frame is most likely caused by the readout electronic.

To allow the movement of the spectrometer while simultaneously guaranteeing vacuum-tightness, the flight tube is connected to the chamber with a metal bellow. An example for a spectrum in the time-of-flight frame as well as a converted spectrum can be found in Figure 2.16.

2.5 Multiple-Event Time Digitiser

After being detected in the MCPs of the TOF, the electron signal has to be processed to generate time-of-flight spectra. With high cross sections and flight times in the range of $\mathcal{O}(100 \text{ ns} - 500 \text{ ns})$, this task can be performed by conventional oscilloscopes.

In the experiment at hand, neither the cross section nor the time-of-flight would allow for an efficient data acquisition by conventional oscilloscopes. As shown in Figure 2.16, all relevant electrons exhibit a time-of-flight below $\sim 100 \text{ ns}$. In combination with a low detection rate of $\sim 9 \text{ electrons/s}$ for the Auger electrons (see Section 3.1), the choice was made towards a multiple-event time digitiser for data acquisition.

The advantage of METDs²² is their capability of recording multiple electron events of a periodic signal with temporal resolutions in the range of $\mathcal{O}(10 - 100 \text{ ps})$, which is far below that of simple frequency counters ($\mathcal{O}(1 \text{ ns})$).

²² METD: Multiple-Event Time Digitiser

2.5.1 Schematic Data Acquisition

In the following we will illustrate the operation mode of a METD with a simplified scheme. Since a broad variety of time digitisers exists, the given description will be closely orientated on the METD used in the presented setup.

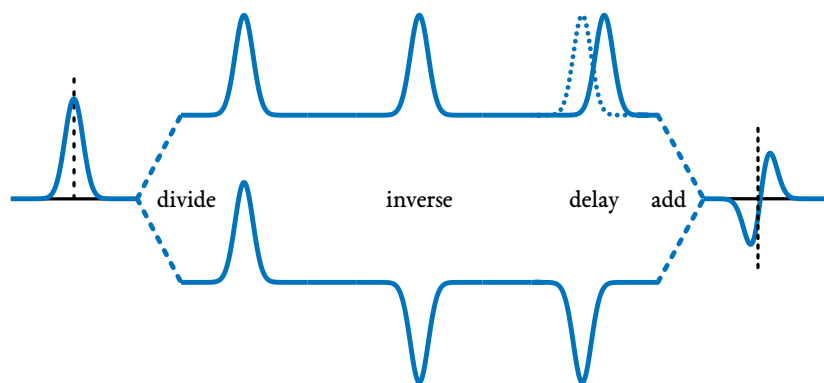


Figure 2.17: Schematic illustration of the arrival time determination by means of a constant fraction discriminator. The vertical dotted line represents the arrival time.

To record the temporal profile of a given recurring signal, a trigger signal is required to start the data acquisition process. Usually, the rising slope of a fast photodiode-signal is used for this purpose.

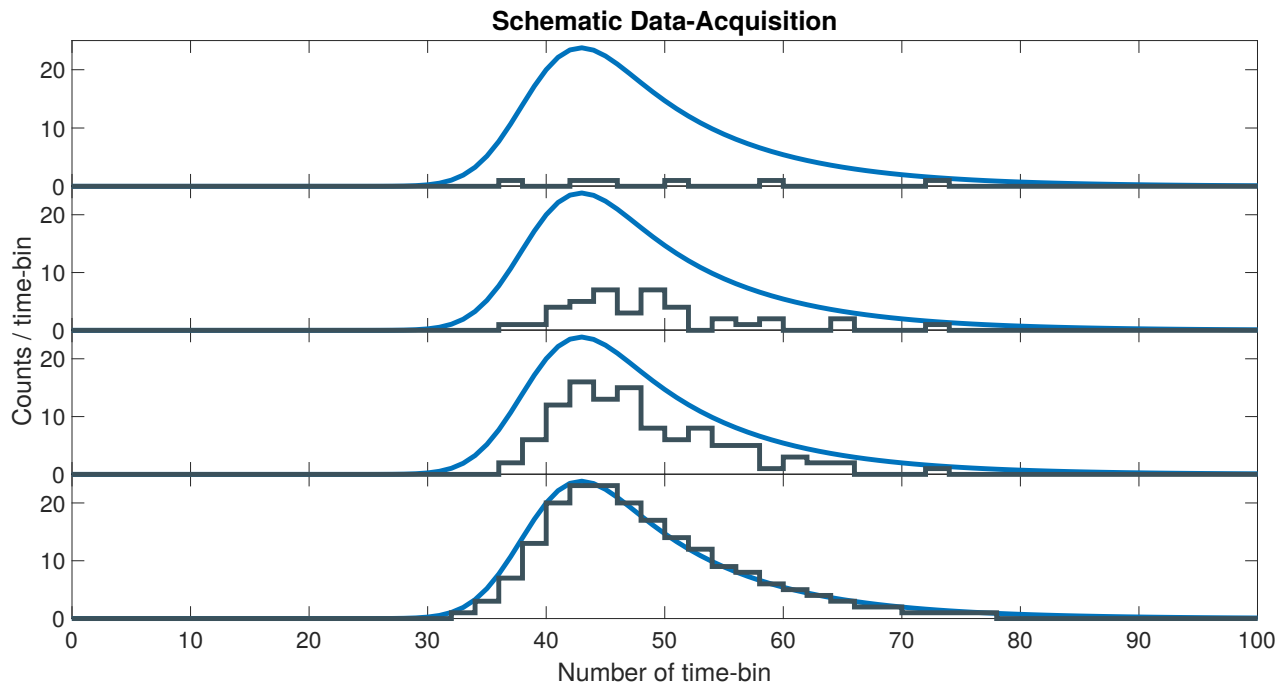


Figure 2.18: Schematic illustration of the data acquisition via a METD. Through multiple counting iterations, the **measured signal** converges to the **true signal** (from top to bottom).

After the trigger is set, the arrival time of each subsequent electron signal is determined in relation to the trigger signal by processing the individual signals in a constant fraction discriminator. This component imitates the mathematical operation of a derivative to determine the zero-crossing of a slope. This is especially useful, if pulses with no sharp maximum, but short rise times are processed. For this purpose, the electron signal is divided equally. After inverting one and delaying the other signal-branch, both subsignals are added (see Figure 2.17). The zero-crossing of the newly formed sum defines the arrival time of the electron signal. The great advantage of this discriminator architecture is its independence of the signal amplitude. If a simple threshold trigger would be used, the determined arrival time would be dependent on the signal height.

To avoid non-linear effects, the count rate has to be kept low enough to prevent the simultaneous arrival of two or more electrons at on time-bin.

By repeating this process whenever the trigger criteria is met, the TOF spectrum can be build by counting every registered event in every corresponding time bin (see Figure 2.18).

Other possible approaches for time digitiser include the interpolation of the signal to determine the arrival time. Here resolutions down to 10 ps can be reached [63], but only in exchange for a lower repetition rate.

2.5.2 MCS6A Time Digitiser

The multiple-event time digitiser used in this thesis is a MCS6A multiple-event time digitiser by FAST ComTec.

It is designed with fully digital circuitry, capable of accepting at least 65 000 events at peak input rates of up to 10^{Gbit/s} for each of the six channels with a temporal resolution of each individual event of 100 ps. Each event has to be limited to an amplitude below 400 mV to prevent non-linear effects [64].

After describing the experimental setup that is used to streak the Auger electrons of carbon, we will now shift the focus towards the experimental results.

Chapter 3

Streaking Carbon Auger Electrons

In classical AES,¹ the most common practice is to trigger the Auger decay through an energy transfer of a continuous electron beam. The Auger electrons are collected with electromagnetic lenses and detected with retarding field analysers. With this approach a huge variety of materials can be studied. It is possible to investigate the surface constituents of materials in the spatial Å regime. Nevertheless, no statements can be made on a temporal scale of those Auger processes.

¹ **AES: Auger Electron Spectroscopy**

For measurements in the temporal domain, it is possible to use table top pump-probe experiments that nowadays can reach temporal resolutions in the attosecond regime. But in most cases, those experiments lack the energy needed to gain access to all inner-shell excitations of interest.

Facilities like FELs or synchrotron sources provide an opportunity to gain access to the photon energies needed for stimulating the Auger decay, but advanced analysis methods like the self-referenced streaking spectroscopy [4] are necessary to overcome their inherent timing-jitter.

With the presented setup it is possible to reach pulse durations in the 100 fs regime with pulse energies of up to 5 keV while reaching pulse charges of up to ~ 180 fC. Setups with an increased complexity can nowadays deliver pulse durations in the 10 fs regime, but in exchange for bunch charges reaching only up to ~ 0.5 aC [3].

This Chapter will compare literature and experimental results of the carbon Auger spectrum, further characterise the experimental setup and finally estimate the lifetime of the Auger decay in carbon.

3.1 Auger Spectrum of Carbon

The electronic shell of a neutral C₁₂ carbon atom consists of two electrons in the K-shell and four electrons in the L-shell.

Thereby, six distinct Auger decays are possible that are listed in Table 3.1. Due to their great similarity in decay energy, it is experimentally difficult to resolve the K-L₁-L₂ and K-L₁-L₃ channel, as well as the K-L₂-L₂, K-L₂-L₃ and K-L₃-L₃ channel. The three energies that can be resolved are experimentally determined to 252 eV, 260 eV and 272 eV [65].

Table 3.1: Cross sections and energies of the possible Auger decays in carbon induced by electron impact [66]. The values are calculated from a combination of the relativistic distorted wave and the plane-wave Born approximations [67].

Decay channel	Energy in [eV]	Cross section in [\AA^2] at 3 keV impact energy
K-L1-L1	255.89	1.1×10^{-3}
K-L1-L2	264.46	3.6×10^{-4}
K-L1-L3	264.47	7.2×10^{-4}
Σ		1.08×10^{-3}
K-L2-L2	273.03	1.1×10^{-5}
K-L2-L3	273.04	2.9×10^{-4}
K-L3-L3	273.05	1.7×10^{-4}
Σ		0.47×10^{-3}

To estimate how many Auger electrons are generated in the experimental setup by an electron beam inside the target, the following formula will be used

$$N_A = \sigma \frac{N_T N}{A}. \quad (3.1)$$

Here N_A is the number of generated Auger electrons, σ the cross-section for an Auger decay induced by electron impact, N_T the number of target particles, N the number of electrons in the beam and A the area illuminated by the electron beam.

The total cross-section for all decay channels for an electron impact with a kinetic energy of 3 keV is $2.6 \times 10^{-3} \text{\AA}^2$. By assuming an average density of amorphous carbon of 1.95 g/cm^3 [32] and a layer thickness of 1 nm, from which Auger electrons can escape (see Figure 1.7), the amount of accessible carbon atoms in the target is projected to be $N_T = 2.93 \times 10^{13}$. The number of 3 keV electrons per pulse are estimated to be $N = 9.36 \times 10^5$ (see Figure 2.11). The resulting passel of Auger electrons per pulse of $N_A = 2800$ has to be adjusted to accommodate for multiple factors that decrease the number of detected Auger electrons per pulse

$$\begin{aligned} N_A^{\text{est.}} &= \phi_{AP} \phi_{ABS} \phi_{ATT} \phi_{SA} \phi_{TR} N_A \\ &= \frac{1}{3} \times 0.04 \times 0.22 \times 0.04 \times 0.03 \times N_A. \end{aligned} \quad (3.2)$$

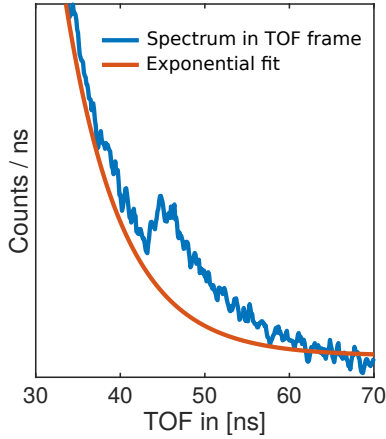
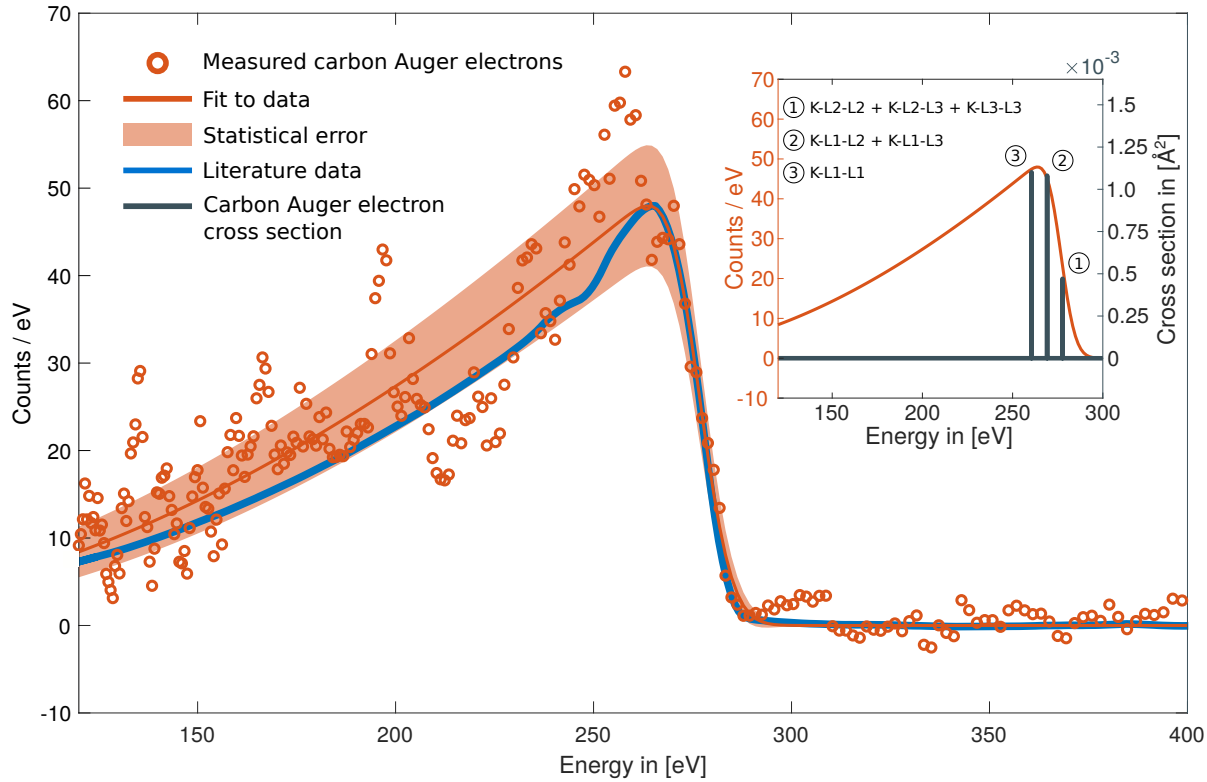


Figure 3.1: The measured Auger spectrum in the TOF frame.



Here ϕ_{AP} gives the reduction by the aperture of the TEM window, ϕ_{ABS} the absorption of electrons inside the TEM window, ϕ_{ATT} the attenuation of the UV beam to avoid saturation in the readout electronics, ϕ_{SA} describes the reduction of the signal through the solid angle capable of reaching the TOF and ϕ_{TR} accounts for the transmission of the TOF. Taking the above factors into account, we conclude with $N_A^{\text{est.}} = 9.4 \times 10^{-3}$ Auger electrons per pulse.

To verify the estimation above, we take the spectrum shown in Figure 3.1 and remove the background in the TOF frame, assuming an exponential background.

The converted spectrum can be found in Figure 3.2. Fitting an exponentially modified Gaussian² to the data, we obtain a **FWHM** of (89 ± 1) eV, with the maximum of the derivative of the spectrum at $E_0 = (272.5 \pm 1.4)$ eV.³ The thus obtained values are in good agreement with the literature values of **FWHM**= 73.18 eV and $E_0 = 272$ eV taken from [65].

Integrating over all electrons collected in the complete Auger peak interval during the 500 000 shots that build the peak in Figure 3.2, we retrieve ~ 4600 electrons.

Figure 3.2: Comparison of experimental Auger spectrum (○) and literature measurements [65] of solid carbon. In addition, the cross section for the K-L1-L1, the sum of the K-L1-L2 and K-L1-L3 and the sum of the K-L2-L2, K-L2-L3 and the K-L3-L3 decay-channel are given. The substructures visible in the experimental data are detector or readout artefacts. To determine the FWHM, an exponentially modified Gaussian was fitted to the measured data (solid line). In addition the statistical error of the fitted counts is given as well.

$$^2 f(x) \sim \exp(-x) (1 - \text{erf}(x))$$

³ It is common practice in AES spectroscopy to define the Auger energy by the maximum of the derivative of a spectrum.

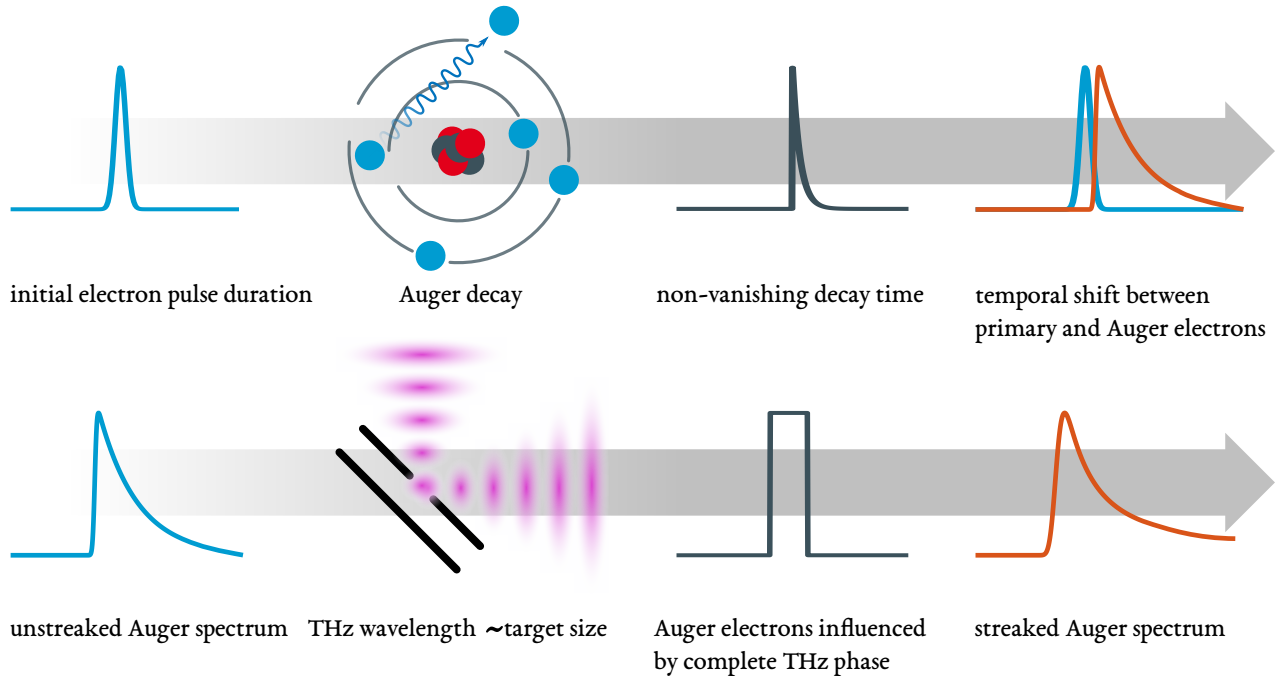


Figure 3.3: Schematic of the convolutions involved in forming the Auger spectrum. In the first step, the electron pulse inside the gun hits the target material and stimulates the Auger decay. The resulting spectrum is a convolution of the temporal profile of the exciting electron pulse and the Auger decay. In the presence of the THz field, the generated Auger spectrum is broadened (top). In the situation at hand, the Auger spectrum experiences a considerable fraction of the THz phase, since THz wavelength and target size are nearly identical (bottom). The broadening shown in this graphic is exaggerated for visual assistance.

Assuming a Poissonian distribution of the counts, we obtain a number of $N_A^{exp.} = (9.2 \pm 2) \times 10^{-3}$ Auger electrons per pulse, which is in good agreement with the estimated $N_A^{est.} = 9.4 \times 10^{-3}$ Auger electrons per pulse.

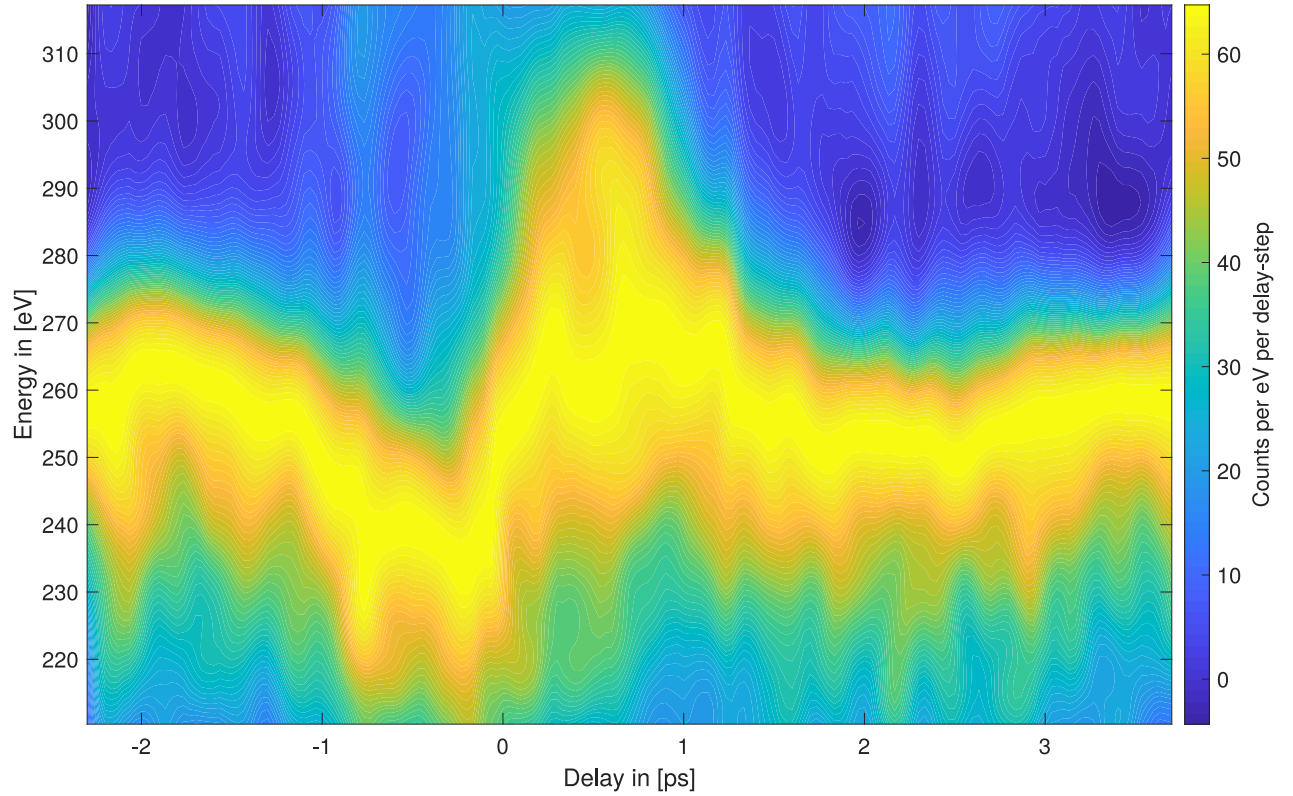
To investigate the temporal dynamics which are underlying this spectrum, we will now let the Auger electrons interact with the THz pulses.

3.2 Streaking of Auger Electrons

The great advantage of the streaking methodology is its capability to characterise the exciting pulse and explore the temporal dynamics of a given decay from the same set of streaking traces. To extract the temporal structure of the exciting pulse, the spectral broadening of the Auger electrons has to be investigated. From the temporal shift between the streaking traces of the primary and Auger electrons, the lifetime of the Auger decay can be determined. For this, the delay between electron impact and the arrival time of the streaking field has to be varied.

The necessary delay between the electron and THz pulses is introduced by the delay-line, described in Section 2.3. The stage is capable of introducing delays with a step-width of (33.3 ± 4.5) fs. For the measurement a total delay of 6 ps^4 was covered to investigate the influence of the complete THz pulse.

⁴ $6 \text{ ps} \hat{=} 180 \text{ steps}$



As stated in Section 1.6, we need to assume that the temporal profile of the exciting pulse is Gaussian to calculate the pulse duration via

$$\tau^2 = \frac{\sigma_s^2 - \sigma_{XUV}^2}{s^2 \pm 4cs}. \quad (3.3)$$

Due to the geometry of this setup, this assumption can no longer be made. Since the THz pulse illuminates the full width of the tilted Si_3N_4 -window no coherent phase relation between electron pulse and streaking field can be established. For any given delay step during the temporal overlap of both pulses, a large variety in combinations of the electron arrival time and THz phase are possible.

Therefore, the streaked Auger spectrum is measured as a convolution of the unstreaked spectrum and the temporal profile of the electron pulse, which again is a convolution of the actual temporal profile of the electron pulse inside the gun and the window width (see Figure 3.3).

3.2.1 Reconstructing the Electron Pulse

In Figure 3.4 the streaked Auger spectrogram is shown. Here we can observe a prominent spectral broadening in the first pico-second after the arrival of the THz pulse.

Figure 3.4: Spectrogram of the energy shift of the Auger electrons generated by the THz pulse. High electron counts are depicted in yellow, while low counts are coloured blue.

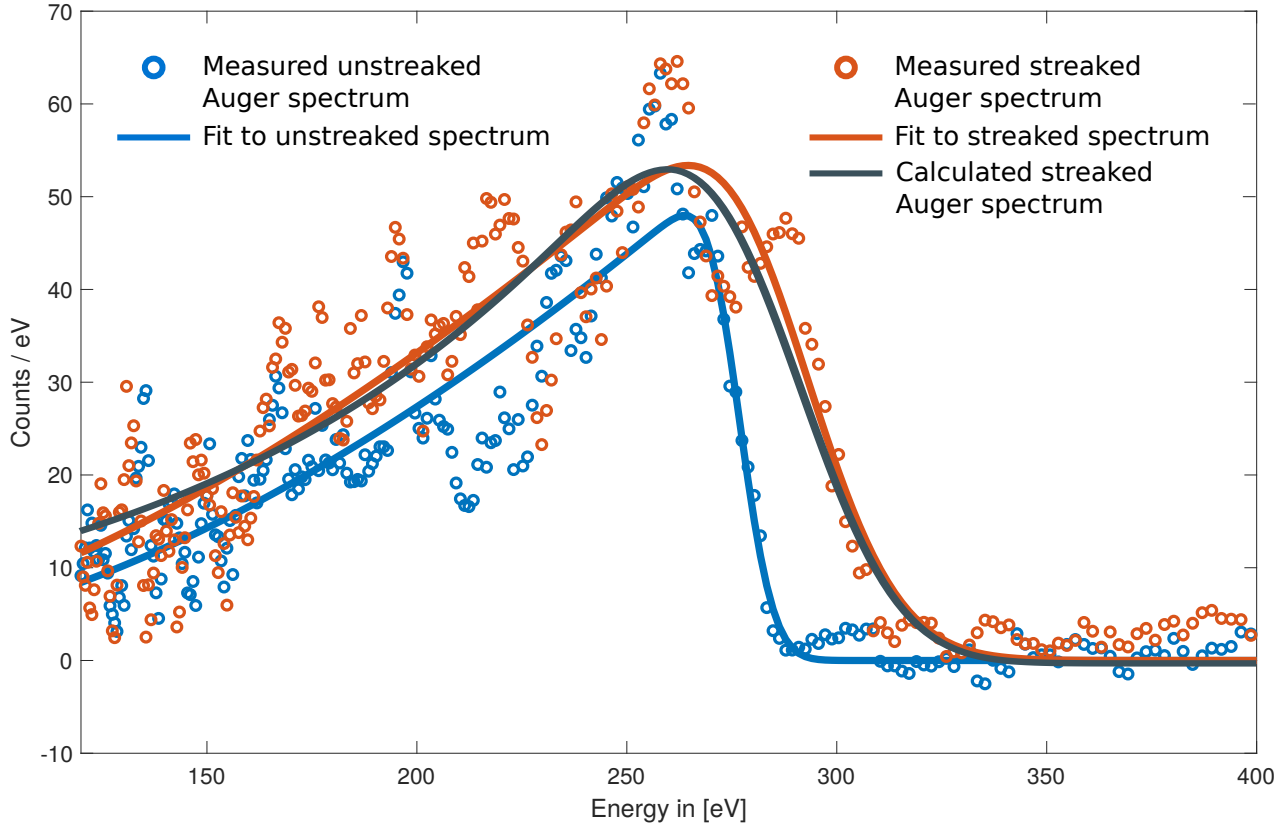


Figure 3.5: Measured **streaked** and **field free** Auger spectra of carbon together with the calculated streaked spectrum that best matches the FWHM of the measurement.

⁵ **Temporal Overlap:** The temporal overlap is defined as the instant where the energy of the streaked primary beam is equivalent to the energy in the field free configuration

The FWHM of around (89 ± 1) eV in the absence of the THz field is broadened up to a FWHM of (116.6 ± 5) eV during the temporal overlap⁵ of electron and THz pulse (see Figure 3.5). The strong broadening of around $\sim 130\%$ indicates a long pulse duration (see Equation 1.81). The maximal broadening is reached at a delay of (275 ± 15) fs, while the FWHM of the complete broadening spans a period of approximately (664 ± 15) fs, which is equivalent to a quarter cycle of the THz pulse (see Figure 3.6).

To estimate the duration of the electron pulses based on the broadening of the Auger spectrum, an array of Gaussian pulses with durations from 10 fs to 200 fs is convoluted with the equivalent width of the Si_3N_4 -window of $0.25 \text{ mm} \times \sin(40^\circ) \times c_0 = 536$ fs. The unstreaked Auger spectrum is then convoluted with this array of possible pulse durations. The duration which results in the same FWHM as the measured streaked spectrum is assumed to be the most likely pulse duration (see Figure 3.5). The pulse duration determined in this manner, is given by $\tau_{exp.} = 138^{+12}_{-38}$ fs, which is in good agreement with the predicted pulse duration of $\tau_e = (114.3 \pm 6.1)$ fs. The maximal streaking speed $s = \partial_t \Delta W$ of the THz field is determined to $s = (108.3 \pm 0.9)$ meV/fs.

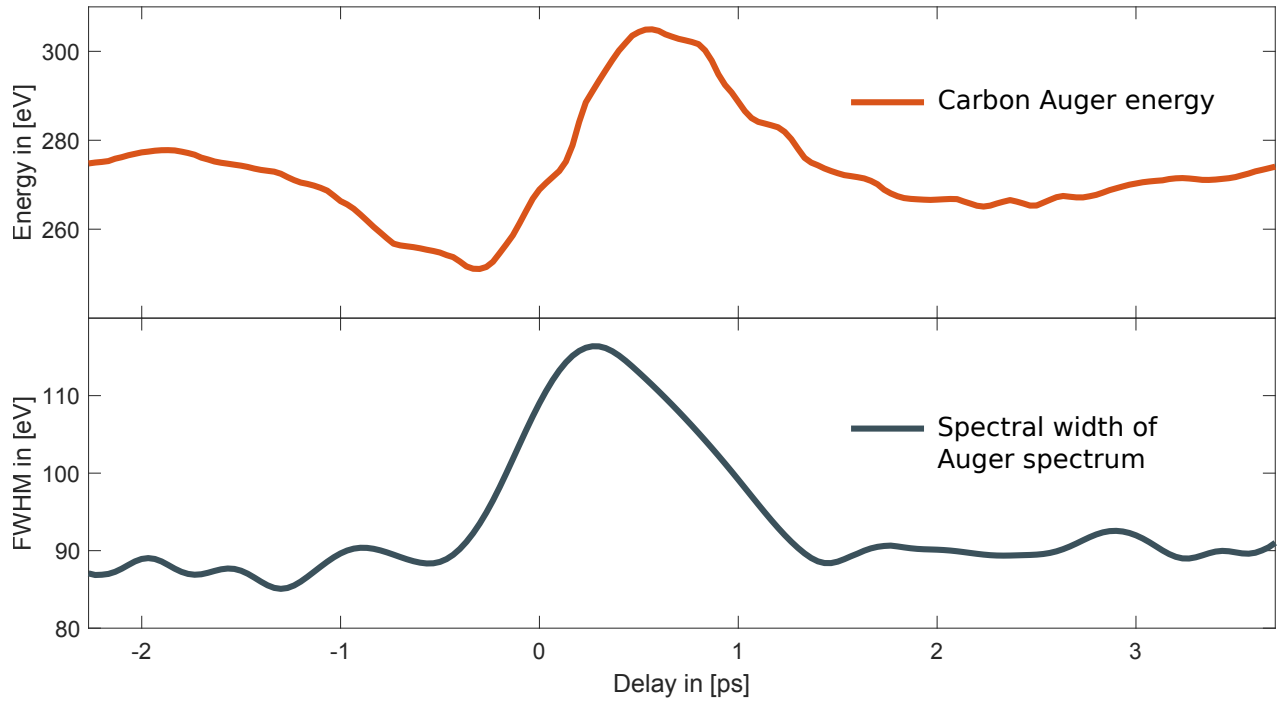


Figure 3.6: **Spectral width** of the **streaked Auger electrons** as a function of delay. The upper curve was determined by finding the maximum of the derivative with respect to the energy for the spectrum of each delay step. The lower curve is the fitted spectral width for every delay step.

3.2.2 Reconstructing the THz pulse

In addition to the reconstruction of the electron pulse duration, it is also possible to extract information about the THz pulse from the streaked spectrum. Two quantities of the THz pulse can be determined from the energy modulation of the Auger spectrum. On the one hand, the time-dependent vector potential and, on the other hand, the electric field strength. To determine the vector potential of the THz field, we compare the time-dependent shift in kinetic energy ΔW to the kinetic energy W_0 in the field free scenario

$$\Delta W = Ae\sqrt{\frac{2W_0}{m_e}}. \quad (3.4)$$

By rearranging the previous equation, we arrive at the vector potential $A(t)$

$$A(t) = \frac{\Delta W(t)}{qe} \sqrt{\frac{m_e}{2W_0}}. \quad (3.5)$$

If the vector potential is differentiated with respect to the temporal delay between electron pulses and the THz pulses, we can obtain the electric field of the THz pulses

$$E = \partial_t A(t). \quad (3.6)$$

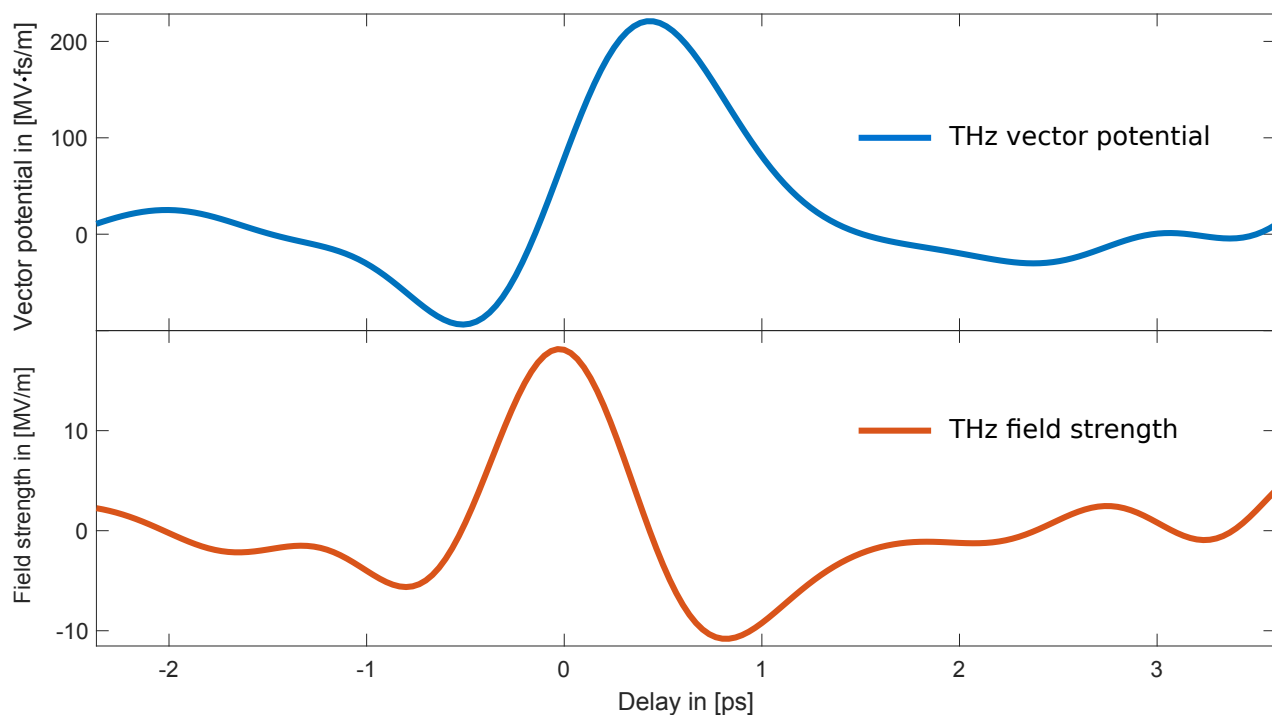


Figure 3.7: **Vector potential** and **electric field** of the THz pulses, reconstructed from the streaking trace of the Auger electrons (see Figure 3.6).

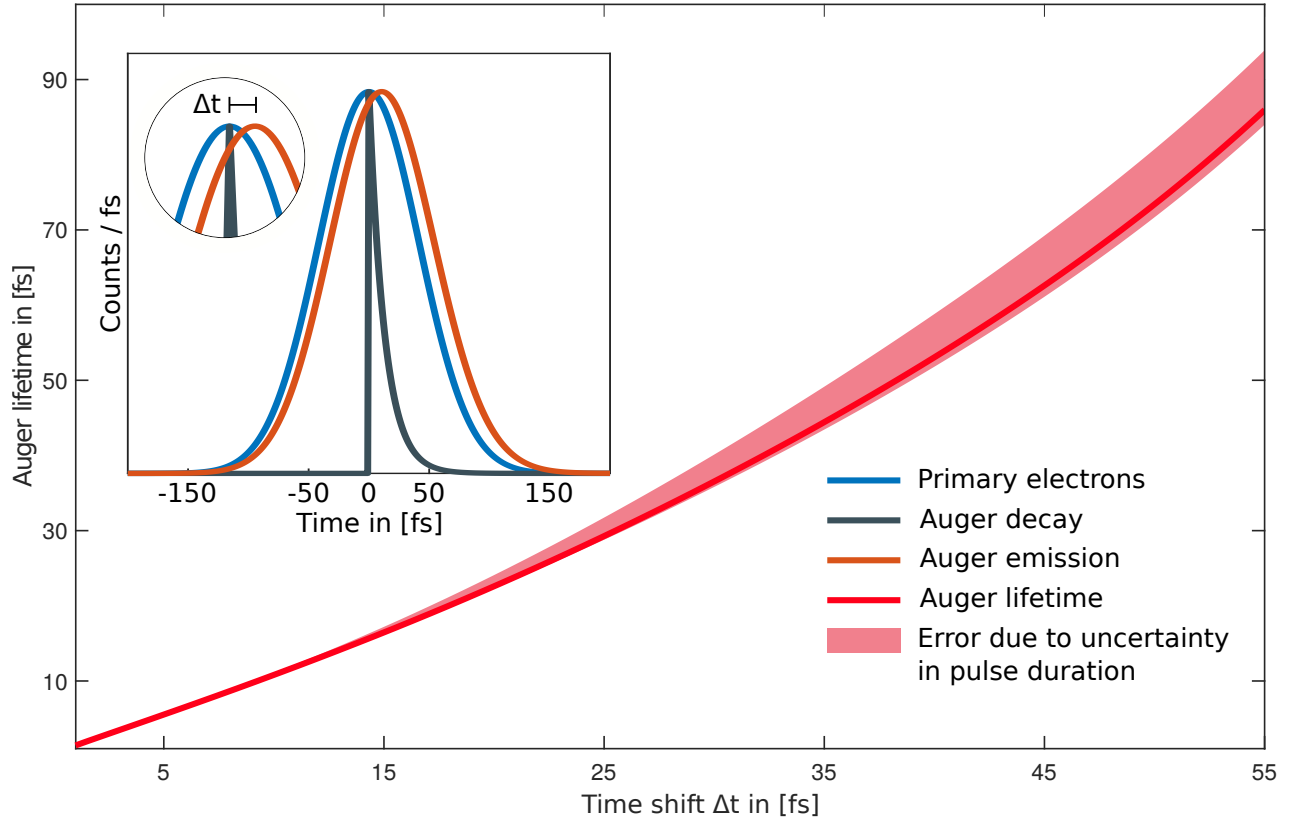
It has to be noted that the results from the analysis have to be multiplied by the factor of $1/\sin 40^\circ$ to account for the tilted sample holder. Taking this factor into account, we find a maximal vector potential of $A = (217.8 \pm 0.1) \text{ MVfs/m}$ and a maximum of the electric field of $E = (18.15 \pm 0.01) \text{ MV/m}$. Both quantities can be found in Figure 3.7.

3.2.3 Lifetime of the Auger Decay

In a classical streaking experiment, the lifetime of an Auger decay is determined by measuring the relative temporal shift between the streaking traces of Auger and photoelectrons.

In this experimental environment it is sufficient to assume an instantaneous emission of the photoelectrons, since their lifetime is in the attosecond regime, while the Auger decay takes place in the femtosecond regime [68].

In the presented experiment, electron pulses are used to generate the Auger electrons. We assume that the leading edge of the primary electrons in the spectrum have only experienced elastic scattering and therefore are not subject to any process that has an internal temporal structure. Hence the shift between Auger and primary electrons can be used to determine the lifetime of the Auger decay. Furthermore, we assume a Gaussian temporal profile of the electron pulse initiating the



Auger decay in the carbon target with a time-dependent intensity of

$$I(t)_{e^-} = I_0 \exp\left(-\frac{t^2}{2\sigma^2}\right). \quad (3.7)$$

Here the FWHM pulse duration of the electron beam is given by $\text{FWHM} = 2\sqrt{2\ln 2}\sigma$. The final emission of Auger electrons is characterised by the convolution of the ionising beam described above, and the exponential decay of the Auger process.

The time-dependent amplitude of the Auger decay is given by

$$A(t) = \begin{cases} 0 & \text{for } t < t_0 \\ A_0 \exp\left(-\frac{t-t_0}{\tau_A}\right) & \text{for } t \geq t_0 \end{cases}. \quad (3.8)$$

The amplitude and the decay lifetime of the Auger process is given by A_0 and τ_A , respectively.

Figure 3.8: Calculated **Auger lifetime** as a function of the temporal shift Δt between Auger and primary electrons. Assuming a $\text{FWHM} = 138$ fs of the **primary electron pulses** and a **Auger lifetime** of $\tau_A = 12$ fs we obtain a temporal shift of $\Delta t = 11$ fs between the primary electrons and the **measured Auger electrons** due to the non-vanishing Auger lifetime.

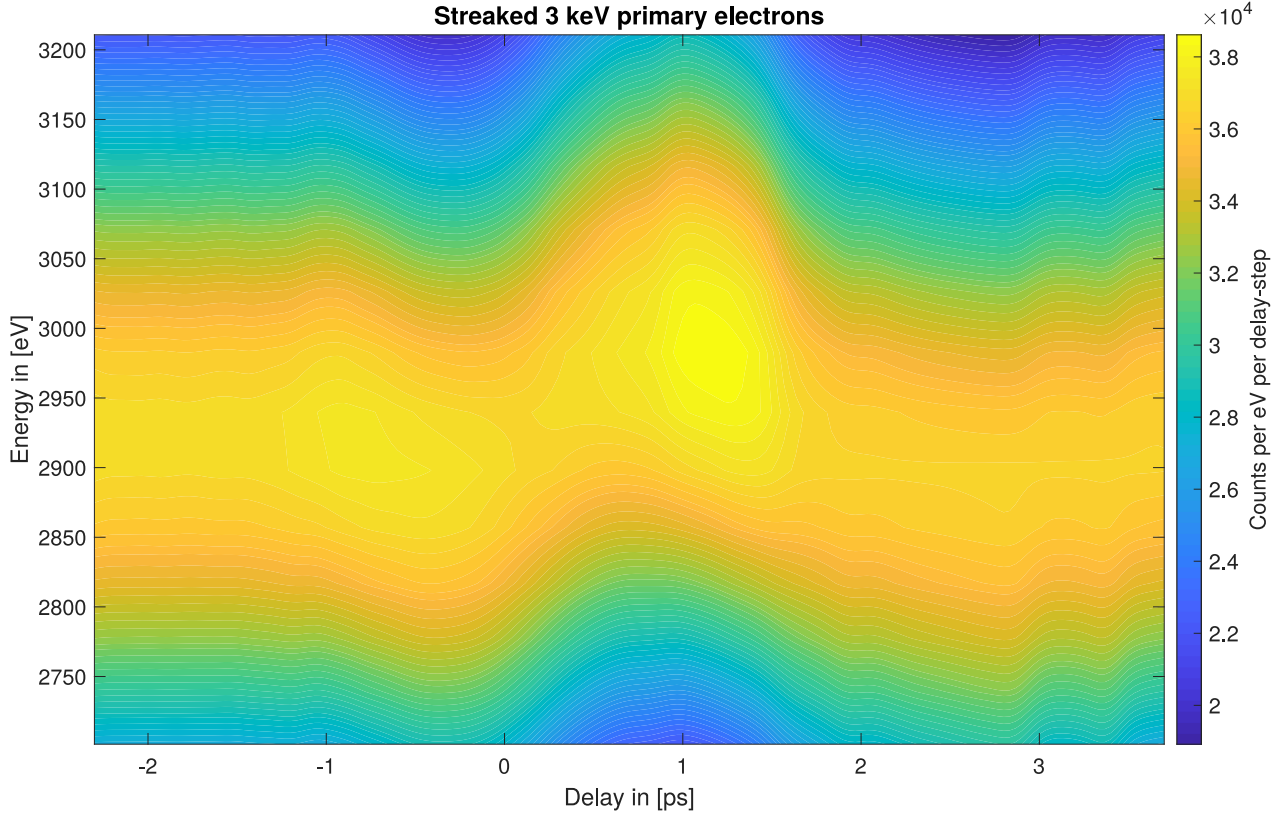


Figure 3.9: Energy shift introduced to the primary electrons by the THz pulse as a function of temporal delay. The varying signal strength can be correlated to factors like the current field-configuration of the THz field or tunneling effects [69].

The convolution of the Auger decay and the exciting electron pulse is given by [70, 71]

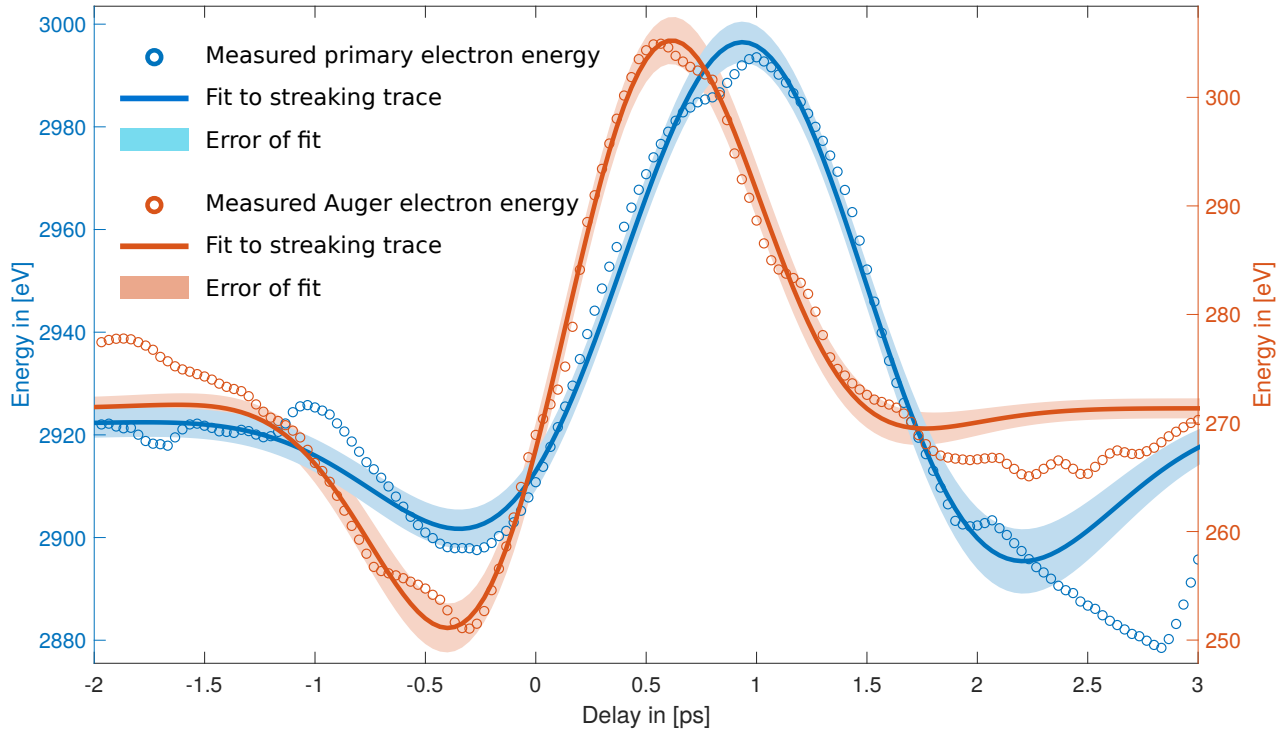
$$\begin{aligned}
 I(t)_A &= I(t)_{e^-} \otimes A(t) \\
 &= I_0 A_0 \frac{\sigma\sqrt{2\pi}}{2} \exp\left(\frac{1}{\tau_A} \left(t_0 - t + \frac{\sigma^2}{2\tau_A}\right)\right) \times \dots \quad (3.9) \\
 &\quad \left(1 - \operatorname{erf}\left(\frac{1}{\sqrt{2}\sigma} \left(t_0 - t + \frac{\sigma^2}{\tau_A}\right)\right)\right).
 \end{aligned}$$

If we now compute the resulting shift Δt (see Figure 3.8) between the exciting pulse and the convolution of the Auger decay and the primary pulse as a function of the lifetime of the decay, we can use the inverse function to determine the lifetime of the Auger process as a function of the temporal shift between the primary and Auger signal.

With an Auger lifetime of $\tau_A = 12$ fs, we obtain a theoretical shift of $\Delta t = 11$ fs between the primary electrons and the Auger emission, if a FWHM of 138 fs of the electron pulse is assumed.⁶

To validate those theoretical assumptions, we now investigate the measured shift between the streaked primary electrons (see Figure 3.9) and the Auger electrons they produce. Since the primary electrons are used to generate the Auger electrons, which exhibit a non-vanishing

⁶ The natural linewidth of carbon of $\Gamma = 56$ meV translates to a lifetime of $\tau_A = 12$ fs [72, 73].



lifetime, the primary electrons should be influenced by the THz field before the Auger electrons. As depicted in Figure 3.10, the exact opposite of the predicted behaviour is measured. The interaction of the Auger electrons with the THz field seem to take place before the interaction of the 3 keV electrons with the THz field take place.

A possible explanation for this result may lie in the one order of magnitude energy difference between the primary electrons and the Auger electrons. In a classical streaking experiment the kinetic energy of Auger electrons and photoelectrons are of a similar order of magnitude. In the setup at hand, the primary electrons exhibit velocities of 10.8% of the speed of light and therefore, relativistic effects should be taken into account.

Due to their high velocity and the geometry of the presented setup, the 3 keV primary electrons experience a considerable relativistic redshift of the THz wave, which results from the relativistic Doppler effect that is given by

$$v = v_0 \frac{\sqrt{1 - \beta^2}}{1 - \beta \cos(\Theta)}, \quad \text{with } \beta = \frac{v}{c_0} = \sqrt{1 - \left(\frac{1}{E/mc_0^2 + 1} \right)^2}, \quad (3.10)$$

where the frequency at rest is given by ν_0 , the kinetic energy by E and the angle of the trajectory between observer and light-source is given by Θ (see Figure 3.11).

Figure 3.10: Phase shift between the **primary electrons** and the **Auger electrons**. The energies of the primary and Auger electrons are defined by the maximum of the derivative of the respective spectra.

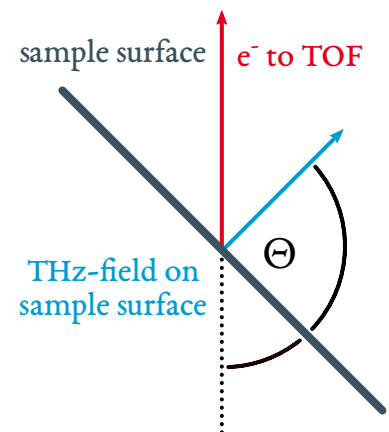


Figure 3.11: Relativistic Doppler effect for arbitrary angles. Note that the relative motion of the electrons with respect to the THz field is opposite to the absolute motion.

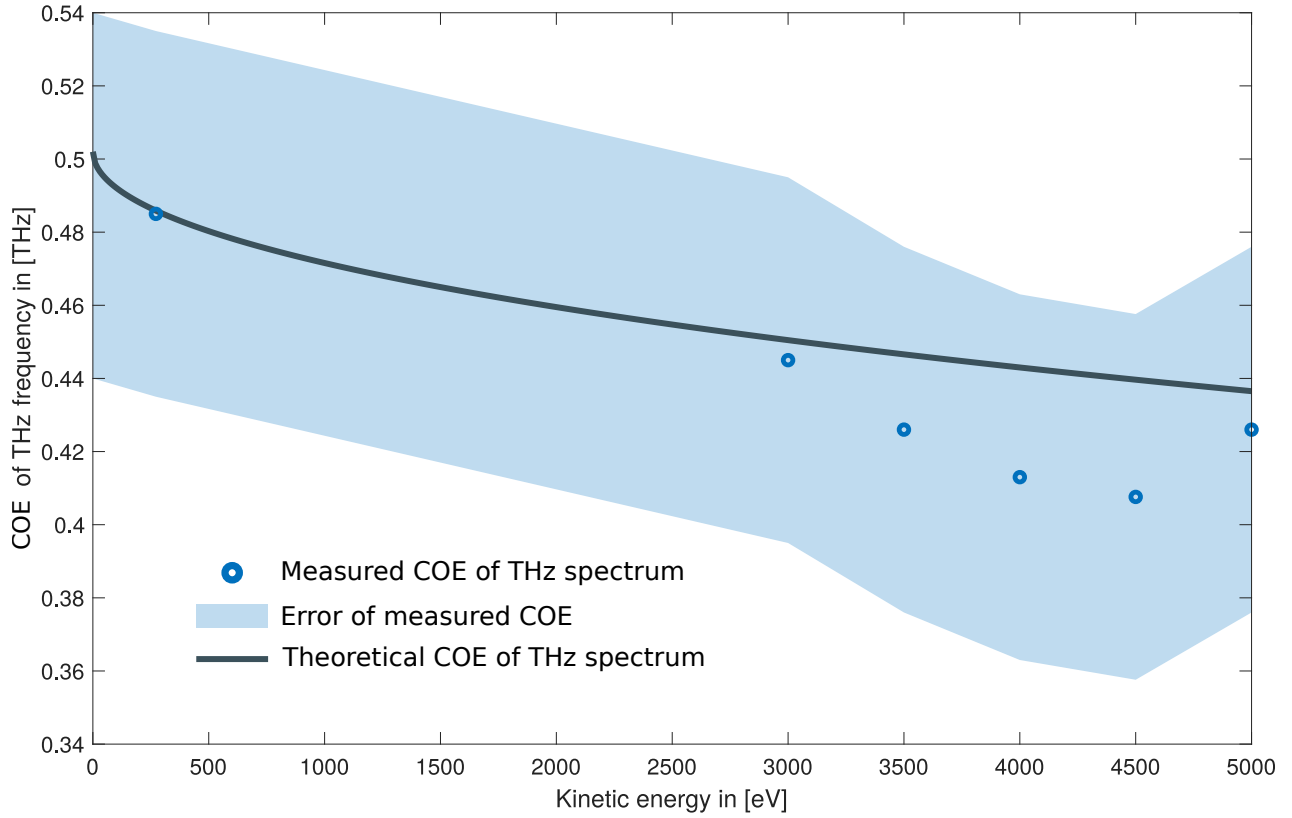


Figure 3.12: Different kinetic energies of the primary electrons or the Auger electrons lead to different centres of energy in the reconstructed THz spectra (see Equations 3.11 and 3.10). A possible explanation might be a relativistic Doppler effect. Due to the limited amount of delay steps, the reconstruction of the THz COE can be challenging, which is reflected in its large uncertainty.

To test this hypothesis, the center of energy (COE) of the frequency of the THz pulse is determined for multiple primary energies as well as for the Auger electrons and the EOS signal. The resulting frequencies are depicted in Figure 3.12. Taking the COE of the THz spectrum obtained in the EOS-measurement (see Section 2.3.1) of $\nu_0 = (0.502 \pm 0.02)$ THz as the frequency at rest, we obtain the solid line shown in Figure 3.12. The measured redshift of the 3 keV primary electrons is $\nu/\nu_0 = 0.88 \pm 0.1$, whereas the theoretical redshift (see Equation 3.10) is given by $\nu/\nu_0 = 0.897$.

The redshift of the Auger electrons is significantly weaker. The measured redshift is determined to be $\nu/\nu_0 = 0.96 \pm 0.1$ while the theoretical redshift is given by $\nu/\nu_0 = 0.968$.

To determine the phase shift between the Auger electrons and the primary electrons, we now have to adjust the streaking traces of Auger and primary electrons. Therefore, sine waves with a Gaussian envelope are fitted to the streaking traces

$$f(t) = I_0 \exp\left(-\left(\frac{t-t_0}{\sigma}\right)^2\right) \sin(\omega(t-t_0) - \phi). \quad (3.11)$$

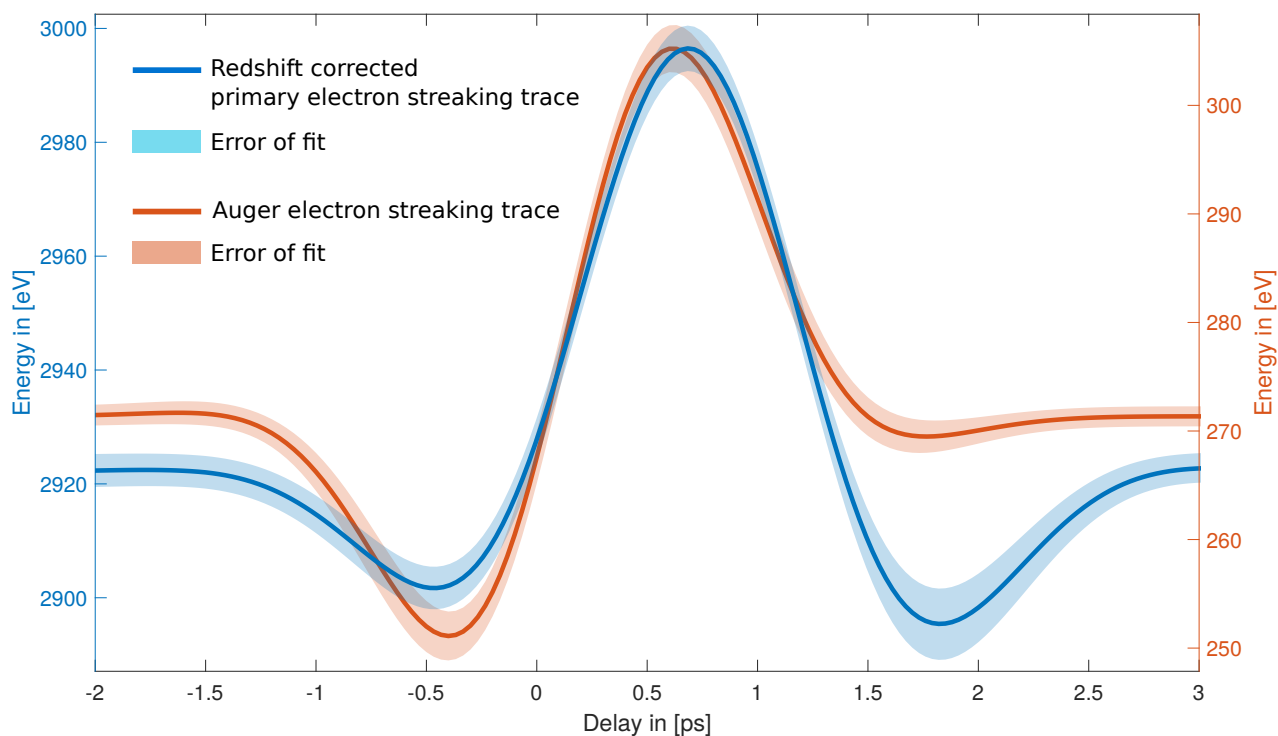


Figure 3.13: The fitted streaking traces of the **primary electrons** and **Auger electrons** show the correct ordering after the redshift correction, which results in a $\Delta t = 11_{-11}^{+52}$ fs temporal shift between primary and Auger electrons.

To determine the point in time from which the redshift must be taken into account, we assume that the interaction of the electrons and THz field start at -3σ of the Gaussian envelope determined through fitting, which is equivalent to -1.7 ps temporal delay. It is worth noticing, that by assuming a different range in which an interaction of electrons and THz field takes place, the temporal shift and therefore the calculated Auger lifetime will change.

If we now compress the temporal delay of the 3 keV electrons by a factor of $v_{3\text{keV}}/v_0 = 0.88$ to accommodate for the redshift, the temporal shift between Auger electrons and primary electrons is in the right ordering and amounts to $\Delta t = 11_{-11}^{+52}$ fs. This temporal shift translates to an estimated Auger lifetime of $\tau_{\text{Auger}} = 13_{-13}^{+100}$ fs (see Equation 3.9 and Figure 3.8).

It is worth noticing, that in practice the approach to extract the Auger lifetime from the temporal shift is only viable, if the duration of the exciting pulse and the Auger lifetime are of the same order of magnitude and the primary electron pulse profile is exactly Gaussian. In the presented experiment, this is not the case, as the electron pulses exhibit a duration of at least one order of magnitude higher than the expected Auger lifetime. Therefore, an interpretation of the data should only be made with great caution and a claim to realistic physical statements should be omitted.

Furthermore, the findings on the redshift of the THz field offer new research opportunities, although it is possible, that the measured dependency of the THz frequency on the kinetic energy of the streaked electrons has a different origin than the assumed relativistic Doppler effect.

Another reason may be the asymmetric geometry of the setup, which might lead to complicated field configurations in the interaction zone. But in order to confirm or reject this hypothesis, far-reaching investigations should be carried out.

Therefore, we discuss the summarised results and further strategies for the experiment in the concluding chapter.

Chapter 4

Summary and Outlook

In this final Chapter we will summarise the experimental results we obtained in Chapter 3 and will investigate possible future applications as well as the steps necessary to improve the setup to explore those applications.

4.1 Summarised Results

Within the scope of this thesis, a setup was designed and implemented allowing to streak Auger electrons originating from thin films. To make the inner-shell excitations accessible that stimulate the Auger decays, short electron pulses provided by a photon-driven electron gun are used. The Auger electrons are streaked by strong near single-cycle THz pulses, which are generated by optical rectification in LiNbO₃ using a tilted pulse front configuration.

The electron gun implemented in this setup demonstrates pulse durations of $\tau = 138^{+12}_{-38}$ fs at a beam energy of 3 keV. This duration, however, is not directly available during the streaking process due to the tilted geometry of the sample. The 250 μm width of the Si₃N₄-window leads to an effective pulse duration of 536 fs.

Nevertheless, it is possible to imprint a momentum-modulation to the Auger electrons of carbon by spatio-temporal overlapping the electron pulses with THz pulses and thus, creating streaking traces for the primary 3 keV electrons and the 272 eV Auger electrons. The redshift-corrected phase shift between the two traces reveals a duration of the Auger decay in carbon of $\tau_{\text{Auger}} = 13^{+100}_{-13}$ fs.

If the large error is left out of consideration, the experimental results are compatible with the decay time retrieved by the natural linewidth of carbon K-shell electrons of 56 meV suggesting a lifetime of 12 fs [72, 73].

As shown above, the presented technique is far from mature, but shows promising first results. In the next section we will show possibilities to decrease the actual as well the effective pulse duration, the error on the lifetime of the Auger decay and concerns not mentioned so far.

4.2 Outlook

To develop the streaking on thin films to a more mature procedure, at least two major weak points of the current setup need to be addressed. The first being the long effective pulse duration of the electron beam. The second being the long acquisition time. To reach an acceptable signal-to-background ratio, at least 500 000 pulses have to be accumulated for a given temporal delay between electron and THz pulse. To sample the complete THz pulse, a total of ~ 30 hours of measurement time are needed at the current status. This imposes great requirements to the overall stability of the complete setup and is far from practical everyday use.

To get the pulse duration under control, the electron gun has to be adjusted, while a modification of the measurement process increases the usability of the setup.

4.2.1 Optimising the Setup

The most straightforward way to reduce the effective pulse duration is to scale down the width of the Si_3N_4 -window. A width below $30 \mu\text{m}^1$ would reduce the impact of the window width to such an extent that it would be below the current pulse duration inside the gun. But in return, the signal strength would decrease by more than a factor of eight, reducing the usability even further.

Another way to decrease the pulse duration is to reduce the gap between anode and cathode inside the gun. If an upper limit for the kinetic energy of 3 keV is set, the gap could be scaled down to 0.3 mm before vacuum-breakdown is reached.

This reduction would lead to a theoretical pulse duration inside the gun of $\tau_e = 68.5 \text{ fs}$ (see Equation 2.4).² A more effective way to reduce the pulse duration as well as the data acquisition time is to completely redesign the setup.

Two different approaches shall be given in the following, that aim to improve the overall performance of the experiment

Optimised Electron Gun and Data Collection

In the first proposal, the concept of the photon-driven gun is kept, but the anode sample holder is implemented in a THz wave-guide, based on the design given in [74]. By this, the THz polarisation is orientated orthogonal to the sample-surface and the THz field is not reduced by the tilted setup (see for example Figure 2.8). Furthermore, the wave guide increases the field strength of the THz pulses by a factor of three, compared to the free space focus. This allows to operate the

¹ $c_0 \times 30 \mu\text{m} \approx 9 \text{ fs}$

² If the current window-width is kept, the 40% improvement in pulse duration due to the smaller gap size would only translate to a 2% improvement in the effective pulse duration.

Mazzler at its full capacity, resulting in an estimated UV pulse duration of ~ 40 fs. With an additional reduction of the cathode-anode gap inside the gun, ~ 60 fs electron pulses could be possible.

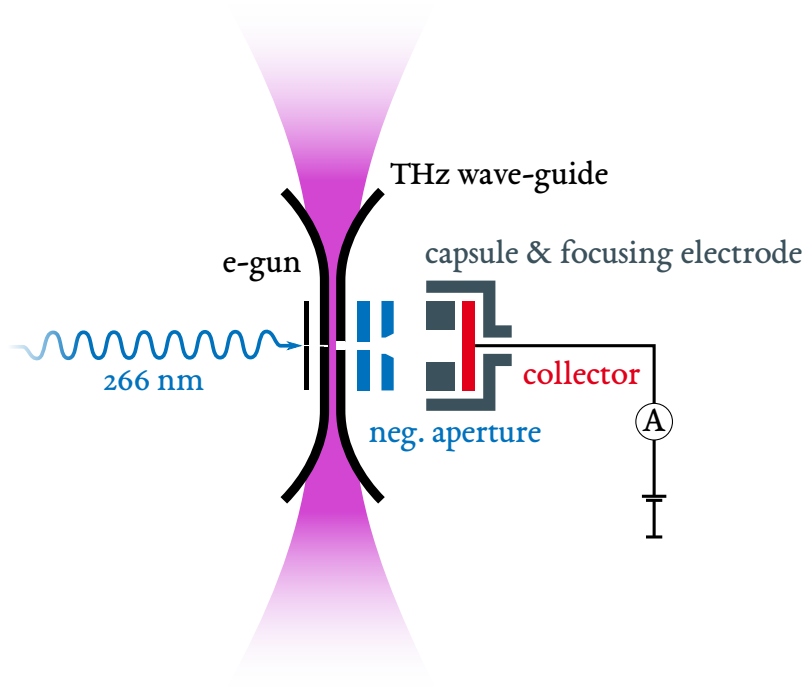


Figure 4.1: A possible new design of the experiment, including a wave-guide [74] for the THz pulses and the exchange of the TOF spectrometer with a retarding field analyser [75].

To profit from the decreased pulse duration, the window-width has to be reduced below $30\ \mu\text{m}$. The signal loss resulting from the reduced window size is compensated by a larger detectable solid angle, which is the result of replacing the TOF spectrometer with a RFA.³ The entrance aperture of the RFA as well as the anode of the gun are designed to be part of the wave-guide (see Figure 4.1). With a gap size of the wave-guide of only $0.75\ \text{mm}$, the detectable solid angle will be $\Omega = 0.11$.⁴

The advantage of the RFA presented in [75] is its capability to operate at currents in the μA -regime, while still be able to resolve electrons with $\Delta E/E_0 = 0.3\ \%$ at $2.5\ \text{keV}$. Therefore, it is not necessary to attenuate the beam to avoid saturation in the readout electronics.

Even with a conservative estimate of $50\ \%$ transmission in the RFA, an overall increase in signal strength by a factor of ~ 80 might be within the bounds of possibility. At the same time a decrease in the effective electron pulse duration by a factor of 4 might be possible.

Active Pulse Compression

The second proposal pursues a more elaborate approach to decrease the temporal profile of the electron pulses.

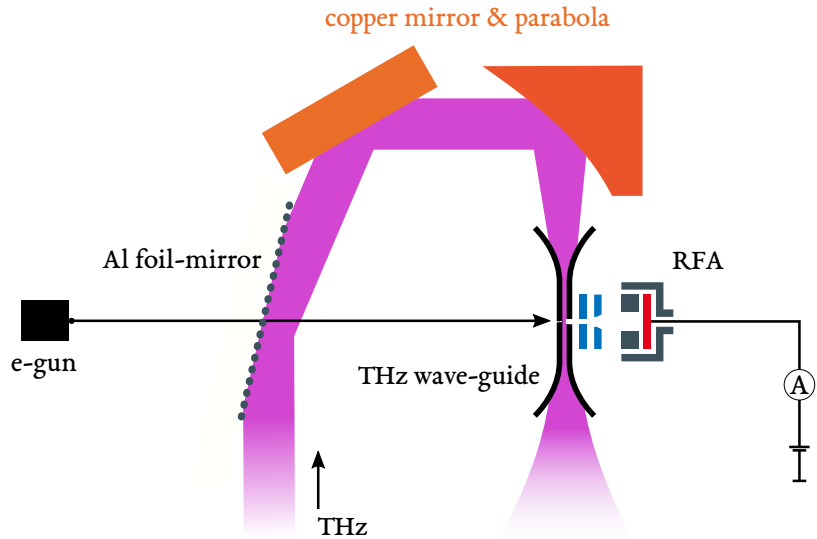
³ RFA: Retarding Field Analyser

⁴ The current solid angle is $\Omega = 0.04$

⁵ RF: Radio Frequency

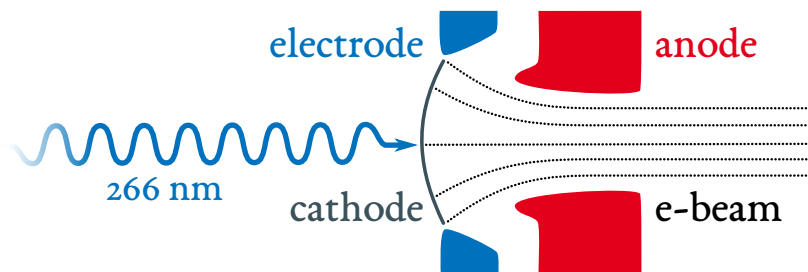
If even shorter durations of the electron pulses are desired, active pulse compression cannot be avoided. In classical gun designs, this is resolved in most cases by the use of RF⁵ pulse compression, which would make it nearly impossible to maintain a tabletop form factor.

Figure 4.2: Another possible design of the experiment, including an active pulse compression as well as a wave-guide and a RFA.



Nevertheless, it is possible to implement active compression by utilising THz pulses as shown in [3]. Here the electron pulses are generated in a conventional electron gun. The pulses then pass through a 40 nm thin Al mirror. On this surface THz pulses are reflected, resulting in a compression of the electron pulses. The THz pulses could then be reused to streak the Auger electrons, which will be generated through electron impact in the sample holder, that will be integrated into the wave-guide (see Figure 4.2).

Figure 4.3: Pierce-type electron gun, adapted from [76]



Crucial for an efficient compression and a successful streaking process is the correct placement of the Al mirror with respect to the gun and the sample, as well as the correct path length for the THz beam compared to the electron beam path. If the path length for the THz and

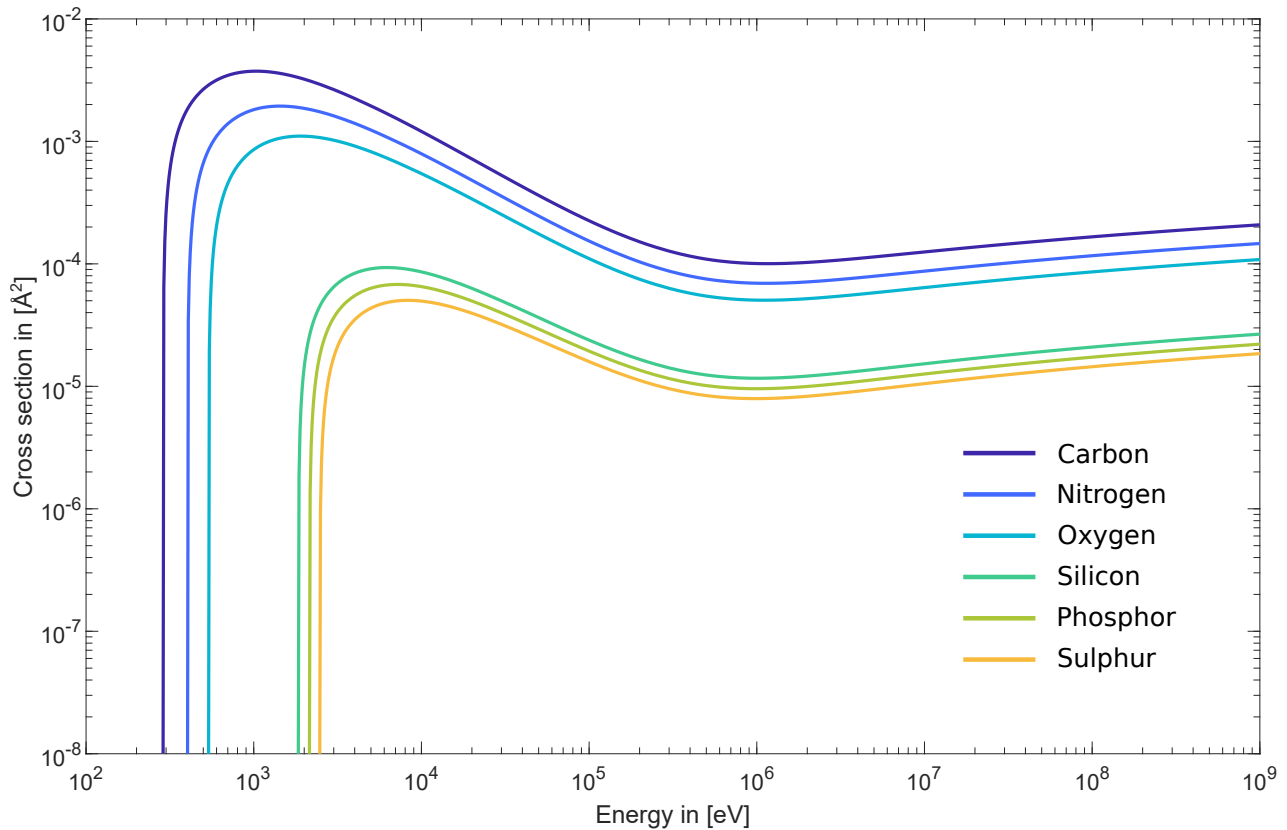


Figure 4.4: The total KLL Auger electron cross section by electron impact for elements of potential interest [66].

electron pulses does not compensate for the different velocities, a temporal overlap is not possible.

With the implementation of an active compression, the necessity arises to separate the sample from the gun. Therefore, a new gun design is mandatory. A possible candidate would be a photon-driven Pierce type gun (see Figure 4.3) The design of this type of gun counteracts space charges inside the gun to a certain degree [77] and is able to achieve a focus outside the gun, depending on the anode design. Nevertheless, the compression setup introduced in [3] was designed for extremely low bunch charges, meaning a thorough investigation is needed before this proposal should be considered for implementation.

Independent of further development of the experimental setup, it might be worthwhile to take different sample materials into consideration.

4.2.2 Possible Targets

There are multiple reasons to select carbon as the first target element of choice. First, there is its significant role in organic chemistry and biology.

Second, there is its high cross section for the Auger process induced through electron impact and closing its relatively high reflectivity in the THz regime [78].

To establish the streaking on thin films as a viable technique, new materials have to be added to the pool of possible targets.

There is a large manifold of elements that are of scientific interest due to various reasons. Being close to carbon in the periodic table, nitrogen and oxygen might be of interest due to their prominence in biology, while silicon and phosphor might be of interest due to their outstanding role in the semiconductor sector. The cross section for the KLL Auger decay of a fraction of those elements can be found in Figure 4.4. Here it also becomes apparent why the overall efficiency of the presented setup has to be improved. With increasing atomic number the cross section decreases dramatically. For example, the cross section decreases by more than one order of magnitude from carbon to sulphur.

For higher atomic numbers new decay channels with higher cross sections are available, but the principle of a decreasing cross section with higher atomic number remains the same.

To open this newly developed tool to a broad range of possible new targets, it is necessary to conduct further optimisation and research.

Bibliography

- [1] Thomas Gaumnitz, Arohi Jain, Yoann Pertot, Martin Huppert, Inga Jordan, Fernando Ardana-Lamas, and Hans Jakob Wörner. Streaking of 43-attosecond soft-x-ray pulses generated by a passively cep-stable mid-infrared driver. *Opt. Express*, 25(22):27506–27518, Oct 2017.
- [2] Li Zheng, Xianfeng Chen, Songsong Tang, and Ruxin Li. Multiple quasi-phase-matching for enhanced generation of selected high harmonics in aperiodic modulated fibers. *Opt. Express*, 15(26):17985–17990, Dec 2007.
- [3] Dominik Ehberger, Kathrin J Mohler, Thomas Vasileiadis, Ralph Ernstorfer, Lutz Waldecker, and Peter Baum. Terahertz compression of electron pulses at a planar mirror membrane. *Physical Review Applied*, 11(2):024034, 2019.
- [4] DC Haynes, M Wurzer, A Schletter, A Al-Haddad, C Blaga, C Bostedt, J Bozek, H Bromberger, M Bucher, A Camper, et al. Clocking auger electrons. *Nature Physics*, pages 1–7, 2021.
- [5] Jean-Claude Diels and Wolfgang Rudolph. *Ultrashort laser pulse phenomena*. Elsevier, 2006.
- [6] Claude Rulliere et al. *Femtosecond laser pulses*. Springer, 2005.
- [7] Geoffrey New. *Introduction to nonlinear optics*. Cambridge University Press, 2011.
- [8] Andrew Weiner. *Ultrafast optics*, volume 72. John Wiley & Sons, 2011.
- [9] Bahaa EA Saleh and Malvin Carl Teich. *Fundamentals of photonics*. John Wiley & Sons, 2019.
- [10] Robert W. Boyd. *Nonlinear Optics*. Academic Press, 2008.
- [11] DN Nikogosyan. Beta barium borate (bbo). *Applied Physics A*, 52(6):359–368, 1991.

- [12] JE Midwinter and J Warner. The effects of phase matching method and of uniaxial crystal symmetry on the polar distribution of second-order non-linear optical polarization. *British Journal of Applied Physics*, 16(8):1135, 1965.
- [13] geb. Grenda Neele Henrike Giverny Friesen. *Evaluation molekularer Targets für eine zeitauflösende Elektronenspektroskopie*. PhD thesis, Universität Hamburg, May 2019.
- [14] Paul R Bolton and CL Deprey. IR Bandwidth and Crystal Thickness Effects on THG Efficiency and Temporal Shaping of Quasi-rectangular UV pulses. Technical report, LCLS-TN-07-4, June 01, 2007.
- [15] A Tomasino, A Parisi, S Stivala, P Livreri, AC Cino, AC Busacca, M Peccianti, and R Morandotti. Wideband thz time domain spectroscopy based on optical rectification and electro-optic sampling. *Scientific reports*, 3:3116, 2013.
- [16] Ingrid Wilke and Suranjana Sengupta. Nonlinear optical techniques for terahertz pulse generation and detection - optical rectification and electrooptic sampling. In *Terahertz Spectroscopy*. CRC press, 2017.
- [17] Q Wu and X-C Zhang. Free-space electro-optics sampling of mid-infrared pulses. *Applied physics letters*, 71(10):1285–1286, 1997.
- [18] Ajay Nahata, Aniruddha S Weling, and Tony F Heinz. A wideband coherent terahertz spectroscopy system using optical rectification and electro-optic sampling. *Applied physics letters*, 69(16):2321–2323, 1996.
- [19] L Xu, X-C Zhang, and DH Auston. Terahertz beam generation by femtosecond optical pulses in electro-optic materials. *Applied Physics Letters*, 61(15):1784–1786, 1992.
- [20] X-C Zhang, Y Jin, and XF Ma. Coherent measurement of thz optical rectification from electro-optic crystals. *Applied Physics Letters*, 61(23):2764–2766, 1992.
- [21] BB Hu, X-C Zhang, DH Auston, and PR Smith. Free-space radiation from electro-optic crystals. *Applied physics letters*, 56(6):506–508, 1990.
- [22] József András Fülöp, Stelios Tzortzakis, and Tobias Kampfrath. Laser-driven strong-field terahertz sources. *Advanced Optical Materials*, page 1900681, 2019.

- [23] Janos Hebling, Gabor Almási, Ida Z Kozma, and Jürgen Kuhl. Velocity matching by pulse front tilting for large-area thz-pulse generation. *Optics Express*, 10(21):1161–1166, 2002.
- [24] Richard Lee Sutherland, Daniel Garth McLean, and Sean Kirkpatrick. Handbook of nonlinear optics, 2003.
- [25] Thomas P Dougherty, Gary P Wiederrecht, and Keith A Nelson. Impulsive stimulated raman scattering experiments in the polaron regime. *JOSA B*, 9(12):2179–2189, 1992.
- [26] Ka-Lo Yeh. *The generation of high field terahertz radiation and its application in terahertz nonlinear spectroscopy*. PhD thesis, Massachusetts Institute of Technology, 2009.
- [27] L Pálfalvi, J Hebling, G Almási, Á Péter, K Polgár, KI Lengyel, and R Szipöcs. Nonlinear refraction and absorption of mg doped stoichiometric and congruent linbo 3. *Journal of applied physics*, 95(3):902–908, 2004.
- [28] L Pálfalvi, J Hebling, J Kuhl, A Peter, and K Polgár. Temperature dependence of the absorption and refraction of mg-doped congruent and stoichiometric linbo 3 in the thz range. *Journal of applied physics*, 97(12):123505, 2005.
- [29] J Hebling, AG Stepanov, G Almási, B Bartal, and J Kuhl. Tunable thz pulse generation by optical rectification of ultrashort laser pulses with tilted pulse fronts. *Applied Physics B*, 78(5):593–599, 2004.
- [30] B Bartal, Ida Z Kozma, AG Stepanov, G Almási, Jürgen Kuhl, Eberhard Riedle, and J Hebling. Toward generation of μj range sub-ps thz pulses by optical rectification. *Applied Physics B*, 86(3):419–423, 2007.
- [31] Yun-Shik Lee. *Principles of terahertz science and technology*, volume 170. Springer Science & Business Media, 2009.
- [32] David R Lide. Crc handbook of chemistry and physics (; boca raton. Fla.: Taylor and Francis, 2005.
- [33] Heinrich Hertz. über einen Einfluss des ultravioletten Lichtes auf die elektrische Entladung. *Annalen der Physik*, 267(8):983–1000, 1887.
- [34] Albert Einstein. Über einen die Erzeugung und Verwandlung des Lichtes betreffenden heuristischen Gesichtspunkt [adp 17, 132 (1905)]. *Annalen der Physik*, 14(S1 1):164–181, 2005.

- [35] LV Keldysh et al. Ionization in the field of a strong electromagnetic wave. *Sov. Phys. JETP*, 20(5):1307–1314, 1965.
- [36] Niels Bohr. II. On the theory of the decrease of velocity of moving electrified particles on passing through matter. *The London, Edinburgh, and Dublin Philosophical Magazine and Journal of Science*, 25(145):10–31, 1913.
- [37] Niels Bohr. LX. On the decrease of velocity of swiftly moving electrified particles in passing through matter. *The London, Edinburgh, and Dublin Philosophical Magazine and Journal of Science*, 30(178):581–612, 1915.
- [38] Hans Bethe. Zur Theorie des Durchgangs schneller Korpuskularstrahlen durch Materie. *Annalen der Physik*, 397(3):325–400, 1930.
- [39] Felix Bloch. Zur Bremsung rasch bewegter Teilchen beim Durchgang durch Materie. *Annalen der Physik*, 408(3):285–320, 1933.
- [40] Stephen M Seltzer and Martin J Berger. Improved procedure for calculating the collision stopping power of elements and compounds for electrons and positrons. *The International Journal of Applied Radiation and Isotopes*, 35(7):665–676, 1984.
- [41] Cedric J Powell, Aleksander Jablonski, and Francesc Salvat. Nist databases with electron elastic-scattering cross sections, inelastic mean free paths, and effective attenuation lengths. *Surface and Interface Analysis: An International Journal devoted to the development and application of techniques for the analysis of surfaces, interfaces and thin films*, 37(11):1068–1071, 2005.
- [42] Lise Meitner. Über die Entstehung der β -Strahl-Spektren radioaktiver Substanzen. *Zeitschrift für Physik*, 9(1):131–144, 1922.
- [43] Pierre Auger. Sur les rayons β secondaires produits dans un gaz par des rayons x. *CR Acad. Sci.(F)*, 177:169, 1923.
- [44] Uwe Becker and David A Shirley. *VUV and Soft X-ray Photoionization*. Springer Science & Business Media, 2012.
- [45] Marion A Brisk and AD Baker. Shake-up satellites in x-ray photoelectron spectroscopy. *Journal of Electron Spectroscopy and Related Phenomena*, 7(3):197–213, 1975.
- [46] T Åberg. Unified theory of auger electron emission. *Physica Scripta*, 1992(T41):71, 1992.

- [47] J Itatani, F Quéré, Gennady L Yudin, M Yu Ivanov, Ferenc Krausz, and Paul B Corkum. Attosecond streak camera. *Physical review letters*, 88(17):173903, 2002.
- [48] John Jasper Bekx. *Towards modeling of electron-impact ionization in warm dense matter*. PhD thesis, Staats-und Universitätsbibliothek Hamburg Carl von Ossietzky, 2020.
- [49] F Quéré, Y Mairesse, and J Itatani. Temporal characterization of attosecond xuv fields. *Journal of Modern Optics*, 52(2-3):339–360, 2005.
- [50] Daniil M Wolkow. Über eine Klasse von Lösungen der Diracschen Gleichung. *Zeitschrift für Physik*, 94(3-4):250–260, 1935.
- [51] Femtolasers Produktions GmbH. User’s Manual for Mirror-dispersion-controlled Ti:Sapphire oscillator FEMTOSOURCE rainbow. 2007.
- [52] G Cheriaux, P Rousseau, F Salin, JP Chambaret, Barry Walker, and LF Dimauro. Aberration-free stretcher design for ultrashort-pulse amplification. *Optics letters*, 21(6):414–416, 1996.
- [53] Jürgen Eichler, Lothar Dünkel, and Bernd Eppich. Die Strahlqualität von Lasern – Wie bestimmt man Beugungsmasszahl und Strahldurchmesser in der Praxis? *Laser Technik Journal*, 1(2):63–66, 2004.
- [54] Axel Griesbeck, Michael Oelgemöller, and Francesco Ghetti. *CRC Handbook of Organic Photochemistry and Photobiology, -Two Volume Set*. CRC press, 2019.
- [55] THORLABS. Total Transmission of 5mm Thick, Uncoated Sapphire Window, 2021.
- [56] M. Hornig. Pulsdauerbestimmung ultrakurzer Lichtpulse mit nichtlinearer Autokorrelation dritter Ordnung bei 266 nm Wellenlänge. M.S. Thesis, Universität Hamburg, 2015.
- [57] Roman Brannath. *Zeitliche Verteilung von Auger-Elektronen-Wellenpaketen aus der Photoionisation von Atomen*. PhD thesis, Staats-und Universitätsbibliothek Hamburg Carl von Ossietzky, 2016.
- [58] Monika Aidelsburger, Friedrich O Kirchner, Ferenc Krausz, and Peter Baum. Single-electron pulses for ultrafast diffraction. *Proceedings of the National Academy of Sciences*, 107(46):19714–19719, 2010.

- [59] Bao-Liang Qian and Hani E Elsayed-Ali. Electron pulse broadening due to space charge effects in a photoelectron gun for electron diffraction and streak camera systems. *Journal of applied physics*, 91(1):462–468, 2002.
- [60] DAVID H NARUMAND and KENTON D CHILDS. Auger spectrometers: A tutorial review. *Applied Spectroscopy Reviews*, 34(3):139–158, 1999.
- [61] Ulrike Frühling. *Lichtfeld getriebene Streak-Kamera zur Einzelschuss Zeitstrukturmessung der XUV-Pulse eines Freie-Elektronen Lasers*. PhD thesis, DESY, 2009.
- [62] Oliver Schepp. *Untersuchungen zur Reaktionsdynamik kleiner Moleküle mittels interferometrischer VUV-VUV Anrege-Abfrage Spektroskopie*. PhD thesis, Staats-und Universitätsbibliothek Hamburg Carl von Ossietzky, 2018.
- [63] David D Eskeldson, Reginald Kellum, and Donald A Whiteman. A Digitizing Oscilloscope Time Base and Trigger System Optimized for Throughput and Low Jitter. *Hewlett-Packard Journal*, pages 24–30, October 1993.
- [64] FAST ComTec GmbH. *Model MCS6A, 64 Bit 5/(6) input 100 ps Multistop TDC, Multiscaler, Time-Of-Flight*, 11 2011.
- [65] Lawrence E Davis. Handbook of auger electron spectroscopy. *Physical Electronics Division*, 1978.
- [66] Xavier Llovet, Francesc Salvat, David Bote, Francesc Salvat-Pujol, Aleksander Jablonski, and Cedric J Powell. *NIST Database of Cross Sections for Inner-shell Ionization by Electron Or Positron Impact*. US Department of Commerce, National Institute of Standards and Technology, 2014.
- [67] David Bote and Francesc Salvat. Calculations of inner-shell ionization by electron impact with the distorted-wave and plane-wave born approximations. *Physical Review A*, 77(4):042701, 2008.
- [68] Martin Schultze, Markus Fieß, Nicholas Karpowicz, Justin Gagnon, Michael Korbman, Michael Hofstetter, S Neppl, Adrian L Cavalieri, Yannis Komninos, Th Mercouris, et al. Delay in photoemission. *science*, 328(5986):1658–1662, 2010.
- [69] Lara Wimmer, Georg Herink, Daniel R Solli, Sergey V Yalunin, KE Echternkamp, and Claus Ropers. Terahertz control of nanotip photoemission. *Nature Physics*, 10(6):432–436, 2014.

- [70] K Wenig, Marek Wieland, A Baumann, S Walther, A Dimitriou, MJ Prandolini, O Schepp, I Bermúdez Macias, M Sumfleth, N Stojanovic, et al. Electronic decay of core-excited HCl molecules probed by THz streaking. *Structural Dynamics*, 6(3):034301, 2019.
- [71] Katharina Chirvi. *Zeitaufgelöste Untersuchung des Auger-Zerfalls in dissoziierenden HCl-Molekülen*. PhD thesis, Staats-und Universitätsbibliothek Hamburg Carl von Ossietzky, 2021.
- [72] F Sette, GK Wertheim, Y Ma, G Meigs, Silvio Modesti, and CT Chen. Lifetime and screening of the c 1s photoemission in graphite. *Physical review B*, 41(14):9766, 1990.
- [73] DL Walters and Ch P Bhalla. Nonrelativistic Auger Rates, X-Ray Rates, and Fluorescence Yields for the 2 p Shell. *Physical Review A*, 4(6):2164, 1971.
- [74] W Ronny Huang, Arya Fallahi, Xiaojun Wu, Emilio A Nanni, Huseyin Cankaya, Anne-Laure Calendron, Dongfang Zhang, Koustuban Ravi, Kyung-Han Hong, and Franz X Kärtner. Terahertz-driven, sub-keV electron gun. In *2016 Conference on Lasers and Electro-Optics (CLEO)*, pages 1–2. IEEE, 2016.
- [75] Peter Köhler. *Design, Konstruktion und Test eines hochauflösenden Gegenfeldanalysators mit fokussierender Elektrode und hochgelegtem Kollektor*. PhD thesis, Justus-Liebig-Universität Giessen, 2018.
- [76] AS Gilmour. *Klystrons, traveling wave tubes, magnetrons, crossed-field amplifiers, and gyrotrons*. Artech House, 2011.
- [77] JR Pierce. Rectilinear electron flow in beams. *Journal of applied physics*, 11(8):548–554, 1940.
- [78] Yuya Morimoto and Peter Baum. Attosecond control of electron beams at dielectric and absorbing membranes. *Physical Review A*, 97(3):033815, 2018.

